

Unitary Transformations for Nuclear Structure Calculations

Vom Fachbereich Physik
der Technischen Universität Darmstadt

zur Erlangung des Grades
eines Doktors der Naturwissenschaften
(Dr. rer. nat.)

genehmigte Dissertation
von Dipl. Phys. Sabine Reinhardt
aus Groß-Gerau

Darmstadt 2013
D17

Referent:	Prof. Dr. Robert Roth
Korreferent:	Prof. Dr. Jochen Wambach
Tag der Einreichung:	11.02.2013
Tag der Prüfung:	29.04.2013

Summary

The explicit treatment of short-range correlations generated by realistic and chiral potentials is the main goal of the Unitary Correlation Operator Method (UCOM) and the Similarity Renormalization Group (SRG) approach. Both methods use unitary transformations to derive phase-shift equivalent nucleon-nucleon interactions. Even if both methods are conceptually completely different, the underlying unitary transformation can be traced back to generators with the same structure.

The first part of the thesis discusses the basic concepts of the UCOM and the SRG. Exploiting the connection of the generators of these two methods, correlation functions that define the unitary transformation in the UCOM are extracted from SRG calculations, leading to improved convergence in No-Core Shell Model (NCSM) calculations and improved Hartree-Fock results. Alternatively, UCOM correlation functions are obtained by parameterizations whose parameters are determined by energy minimisation. Correlation functions with structures adapted to the SRG-generated UCOM correlation functions produce good results in many-body calculations for realistic and chiral interactions.

Alternative choices of the SRG generator are explored in the second part, with the aim to optimize the balance between induced many-body forces and good convergence behaviour. One choice adds an explicit scale parameter to the square of the momentum, while other choices change the power of momentum. The first choice increase the effect of three- and higher-body contributions and the convergence behaviour becomes worse. In case of the different powers of momentum in the generator, the results are very similar for all flow parameters. Therefore, the choice of the generator used so far provides a good balance between convergence behaviour and induced many-body forces.

The unitary SRG and UCOM transformation of other observables is the topic of the third part. It is performed in a consistent way for radii and multipole operators, which are long-ranged operators. Hartree-Fock calculations for SRG-transformed charge radii deviate only little from the calculations using the bare operators, leading to changes less than 1%. The same holds for UCOM transformed radii. Consistent transition strengths obtained from Random Phase Approximation calculations show more significant deviations from the untransformed strengths for the monopole case with SRG transformation. The UCOM transformation leads to much smaller effects here. In the case of quadrupole transitions smaller effects due to the unitary transformation

are observed for both, the UCOM and the SRG transformation. These results are confirmed in case of the SRG-transformed quadrupole transition in NCSM calculations.

Zusammenfassung

Die explizite Behandlung lang- und kurzreichweitiger Korrelationen, die von realistischen und phänomenologischen Potentialen erzeugt werden, ist das Hauptziel der Methode der unitären Korrelatoren (UCOM) und der Similarity Renormalization Group (SRG). Beide Verfahren basieren auf unitären Transformationen um streuphasenäquivalente Nukleon-Nukleon Wechselwirkungen zu erhalten. Obwohl beide Verfahren sich konzeptionell unterscheiden ist es möglich die unitäre Transformation auf Generatoren ähnlicher Struktur zurückzuführen.

Im ersten Teil der Arbeit werden die grundlegenden Konzepte der UCOM und des SRG Verfahrens diskutiert. Unter Ausnutzung der Ähnlichkeit der Generatoren der beiden Verfahren werden Korrelationsfunktionen, die die unitäre Transformation mit der UCOM beschreiben, aus SRG Berechnungen extrahiert. Dies führt auf verbessertes Konvergenzverhalten in No-Core Schalenmodell (NCSM) Rechnungen sowie verbesserte Ergebnisse in Hartree-Fock Rechnungen. Alternativ werden die Korrelationsfunktionen auch mit Hilfe von Parametrisierungen angegeben deren Parameter durch Energieminimierung bestimmt werden. Korrelationsfunktionen deren Struktur an die Form der SRG-generierten UCOM Korrelationsfunktionen angepasst wurden liefern gute Ergebnisse in Vielteilchenrechnungen für realistische und phänomenologische Potentiale.

Im zweiten Teil der Arbeit werden andere mögliche SRG Generatoren betrachtet um einen Mittelweg zwischen induzierten Vielteilchenbeiträgen und gutem Konvergenzverhalten zu finden. Eine Wahl addiert einen Skalenparameter auf den quadratischen Impuls im Generator, bei anderen Generatoren wird die Potenz des Impulses verändert. Der erste Generator führt zu stärkeren induzierten Drei- und Mehrteilchenbeiträgen sowie schlechterem Konvergenzverhalten. Die Generatoren mit den verschiedenen Potenzen des Impulses zeigen in allen Fällen sehr ähnliches Verhalten. Daher bietet die bisherige Wahl des Generators einen guten Mittelweg zwischen induzierten Vielteilchenkräften und guten Konvergenzverhalten liefert.

Im dritten Teil werden unitäre Transformation von anderen Observablen mit den SRG und UCOM Verfahren diskutiert. Die Transformation wird konsistent für Radien und Multipoloperatoren durchgeführt. Hartree-Fock Rechnungen mit SRG transformierten Ladungsradien liefern nur geringe Abweichungen von den nicht transformierten Ergebnissen. Die Änderungen liegen im Bereich von etwa einem Prozent. Das selbe Verhalten wird auch bei der Transformation der Ladungsradien mit der UCOM beob-

achtet. Konsistent berechnete Übergangsstärken die aus Rechnungen mit der Random Phase Approximation zeigen, im Fall des SRG transformierten Monopols, signifikante Abweichungen von den nicht transformierten Ergebnissen. Die UCOM führt in diesem Fall auf wesentlich geringere Abweichungen. Für Quadrupolübergänge werden bei beiden Verfahren wesentlich geringere Abweichungen vom nicht transformierten Fall erzielt. Diese Ergebnisse werden, unter Verwendung der SRG, für den Quadrupolübergang in NCSM Rechnungen bestätigt.

Für Annika

Contents

Introduction	xiii
1 Nucleon-Nucleon Potentials	1
1.1 Argonne V18 Potential	1
1.2 Chiral Potentials	2
1.3 The Deuteron Wave-Function	4
2 Effective Interactions	7
2.1 Unitary Correlation Operator Method	7
2.1.1 Basic Concept	7
2.1.2 Central Correlations	8
2.1.3 Tensor Correlations	9
2.1.4 Correlated Wave Functions	10
2.1.5 Cluster Expansion	12
2.1.6 Correlated Operators	12
2.1.7 Correlated Matrix-Elements	16
2.2 Similarity Renormalization Group	16
2.2.1 Formal Derivation	17
2.2.2 Evolution of Two-Body Matrix-Elements in Momentum-Space	18
2.2.3 SRG and the Deuteron	20
2.3 SRG and UCOM	20
2.3.1 Comparison of the Methods	23
3 Determination of UCOM Correlation Functions	25
3.1 SRG-Generated UCOM	25
3.1.1 Extracting UCOM Correlation Functions from SRG	25
3.1.2 SRG-Generated UCOM Correlation Functions	27

3.2	Optimization of UCOM Correlation Functions	31
3.2.1	Correlation Functions by Energy Minimization	33
3.2.2	Other Parameterizations for UCOM Correlation Functions	35
3.2.3	Few Body Systems with the Different Correlation Functions	41
3.2.4	Many-Body Systems with the Different Correlation Functions	45
4	SRG with Alternative Generators	49
4.1	Λ -SRG	49
4.1.1	Basic Idea	50
4.1.2	Λ -SRG and the Deuteron	53
4.1.3	Few- and Many-Body Calculations	54
4.2	Generators Containing Different Powers of the Momentum	59
4.2.1	Formulation of the Generators	59
4.2.2	The Transformed Deuteron Wave-Function	61
4.2.3	Few-Nucleon System	63
5	Transformed Observables	65
5.1	Unitary Transformation of Operators	65
5.2	Radii	67
5.2.1	Hartree-Fock Calculations with Unitary Transformed Radii	69
5.2.2	NCSM Calculations with SRG-Transformed Radii	73
5.3	Multipole Transition Operators	75
5.3.1	Transition Operators in the RPA Framework	77
5.3.2	Giant Multipole Resonances	78
5.3.3	NCSM Calculations with SRG-Transformed Quadrupole Transition Strengths	92
6	Conclusions	95
A	The Hartree-Fock Method	99
A.1	The Variational Principle	99
A.2	The Hartree-Fock Equations	100
A.3	Hartree-Fock for Interactions in Matrixelement Representation	104
B	The Random Phase Approximation	107
B.1	Equations of Motion	107

B.2	Random Phase Approximation	108
B.3	Derivation of the Two-Body Contribution to the Transition Strength	111
C	Unitary Transformed Densities	117
C.1	Motivation	117
C.1.1	Two-Body Density in Harmonic Oscillator Basis	117

Introduction

The Standard Model of particle physics was introduced as a theoretical model for the description of elementary particles and their interactions. It consists of quarks, leptons and the gauge bosons which carry the weak, strong and electromagnetic interaction as well as the Higgs boson, where the Higgs mechanism explains the masses of the gauge bosons of the weak interaction and the fermionic elementary particles [1]. The included particles and their respective interactions are displayed in Figure 1.

Recently, the ATLAS and CMS experiments at the Large Hadron Collider have discovered a Higgs-like particle [3], which at the present time is the only missing ingredient from the Standard Model. It remains to be seen whether the discovered particle matches Standard Model predictions for its properties, or whether extensions of the Standard Model need to be considered. Even in the latter case, the Standard Model will remain a powerful effective model, because it has been extremely successful in describing many experimental results.

On the theoretical side, the Standard Model is an example of a quantum field theory (QFT). Quantum Chromo Dynamics (QCD) is the quantum field theory responsible for the description of the strong interaction between quarks and gluons in the Standard Model. An interesting property of QCD is asymptotic freedom, i.e., at high momentum transfers, the coupling between quarks and gluons decreases, and a perturbative treatment is possible [4]. At low momentum transfers, however, the theory is non-perturbative because in this regime confinement occurs, i.e., quarks and gluons appear only in bound states. This non-perturbative character makes direct solutions for nuclei very difficult (cf. [5]).

Nuclear physics, and nuclear structure in particular, is dominated by the strong interaction at comparatively low momentum transfers and energies, deep in the non-perturbative regime. A description of nuclear structure phenomena in a quark picture is beyond our capabilities. One can ask, however, whether such a description would be desirable in the first place, i.e., whether nuclear phenomena really depend on details of the strong interaction at the quark level, given the different scales of the problem. Typical energy scales for nuclear phenomena are in the MeV or tens of MeV ranges, whereas quarks can only be resolved by investigating the structure of hadrons at much higher momenta and energies. For this reason, it is sensible to introduce an effective theory, which can be connected to QCD more or less rigorously, and attempt a description in terms of effective degrees of freedom, e.g. nucleons and pions as the

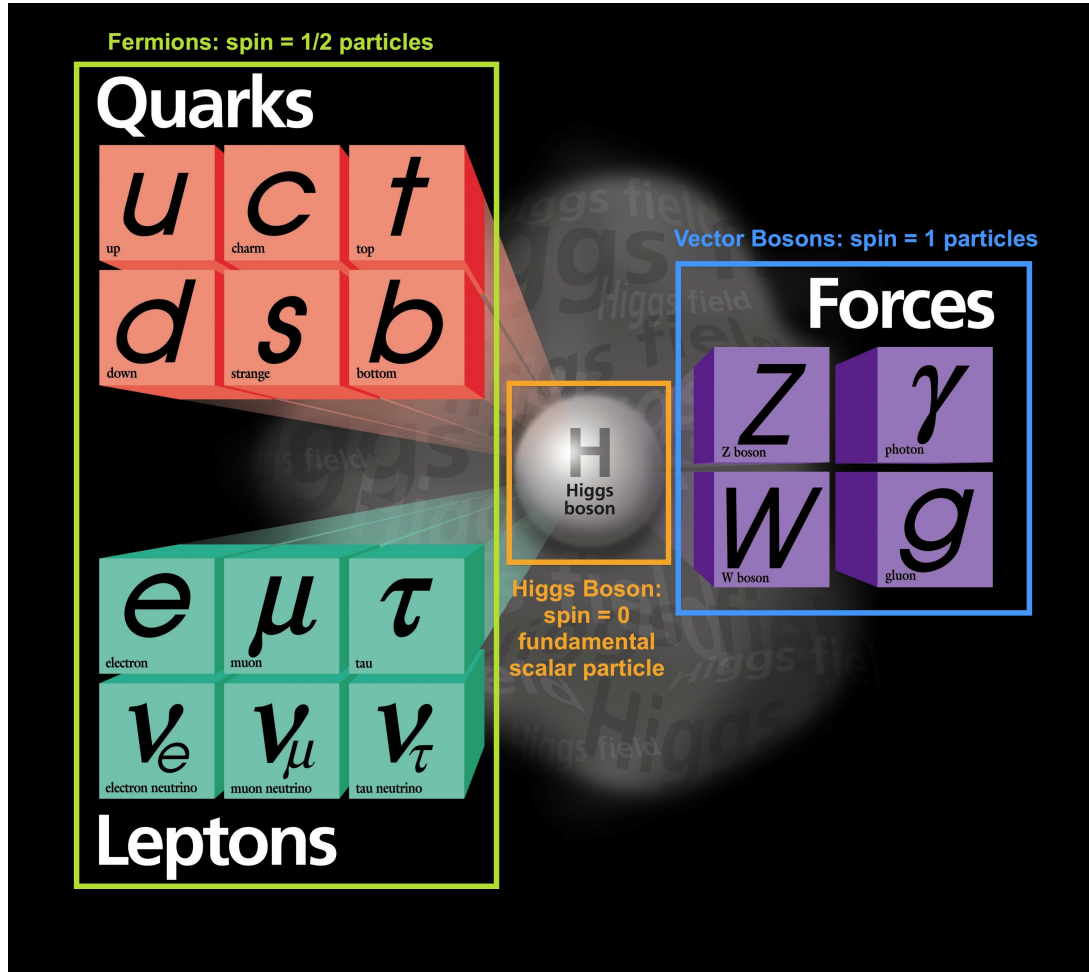


Figure 1: Elementary particles and interactions of the standard model, taken from [2].

lightest confined baryons and mesons, respectively. This effective theory is not valid for high energies, because it is restricted to the region of confinement and does not resolve the substructures included in the underlying fundamental theory, which are important for calculations in the high-energy regime. The appropriate effective theory for the construction of a nucleon-nucleon (NN) interaction is Chiral Effective Field Theory (χ EFT), where nucleons and pions are the degrees of freedom and the chiral symmetry of QCD is taken into account. Within this framework nucleons interact via pion exchanges and contact terms that parametrize unresolved short-range physics. The strength parameters of these contact terms, the so-called low-energy constants, are determined by fits to experimental data, but in principle they can be calculated from QCD. Using chiral EFT, one can construct chiral potentials for use in established nuclear many-body techniques [6, 7]. A very appealing feature of this approach is that the potential can be improved order by order in the expansion of the chiral Lagrangian underlying the theory, and that three-body and higher many-body interactions appear in a natural, hierarchical way and that consistent electromagnetic and weak current

operators can be deduced [8].

Before the advent of interactions from chiral EFT, semi-phenomenological “realistic” potentials like Argonne V18 [9] and CD-Bonn [10] have been employed widely. These interactions are designed to reproduce two-nucleon observables, like phase-shifts obtained from scattering experiments very accurately, with varying degrees of theoretical input. In the case of the Argonne V18, one-pion exchange accounts for the long-range behaviour of the interaction, and it is supplemented with phenomenological short-range terms, while the CD-Bonn is based on meson-exchange theory.

The chiral as well as the realistic potentials induce strong short-range correlations caused by the short-range repulsion of the interaction and tensor forces. In momentum-space representation the interaction exhibits large off-diagonal matrix-elements, which are caused by the induced correlations. Consequently, large model-spaces are necessary to obtain converged results with these interactions in a many-body calculation, which are computationally tractable only for very light nuclei.

One possibility to handle these short-range correlations is the construction of phase-shift equivalent effective interactions. The Unitary Correlation Operator Method (UCOM) [11, 12] was constructed as a method to describe these strong short-range correlations by means of a unitary transformation. For that purpose correlation functions are introduced, which describe the short-range central and tensor correlations explicitly. They are given in a parameterized form obtained from energy minimization. In momentum-space representation the unitary transformation causes a band-diagonalization and, therefore, a decoupling of low-lying from high-lying momenta resulting in an improved convergence behaviour in smaller model-spaces in many-body calculations.

The Similarity Renormalization Group (SRG) [13, 14] is another method to construct an effective interaction by means of a unitary transformation. The generator of the unitary transformation is obtained by solving a renormalization group flow-equation in order to pre-diagonalize the Hamiltonian matrix in a given basis. The choice of the generator is arbitrary and can be adapted to the respective problem [15, 16]. The comparison of the UCOM and the SRG shows that both diagonalize the interaction matrix-elements in momentum-space. A closer investigation shows that the generators of UCOM and SRG have a similar structure, at least at the beginning of the SRG evolution, i.e., they address the same physics. This motivates attempts to use the SRG to extract correlation functions for the UCOM, and to investigate the impact of the restricted parameterizations of the correlation functions [17, 18].

With these effective interactions many-body calculations can now be performed with an adequate computational effort. For light nuclei the No-Core Shell Model (NCSM) [19] is applicable, where an exact diagonalization of the Hamiltonian matrix is performed. For heavier nuclei, mean-field approaches like the Hartree-Fock scheme [20] are a suitable starting point, but it is necessary to go beyond the Hartree-Fock approximation to include long-range correlations that are not described by the UCOM or SRG transformations. Nevertheless, it is a good tool to investigate the effect of SRG and UCOM transformations on the interaction and on ground-state observables. For in-

vestigations of excited states, the Random Phase Approximation (RPA) [21, 22, 23, 24] based on the Hartree-Fock ground-states can be used.

In order to investigate the effect of short-range correlations on observables other than the energy, SRG and UCOM transformations must be applied to transform them consistently [20, 21, 25]. For that purpose the unitary operators of both methods have to be extracted. The unitary transformation can be applied either on the states or on the operators. During the unitary transformation of an operator induced many-body forces are generated which have to be considered in further calculations. Since they are hard to handle, calculations are performed at two- or three-body level. Nuclear densities are of special interest in the investigations of short-range correlations since they can be used to visualize these correlations directly. Other observables which can be compared with experiment are of interest as well.

This thesis is organized as follows. In Chapter 1, the chiral potentials N3LO and N3LOS, along with the Argonne V18 potential as a representative of the realistic interactions are introduced, and their respective deuteron wave-functions are investigated.

In Chapter 2 UCOM and SRG are introduced as methods to derive effective interactions and treat short-range correlations explicitly. A formal comparison of both schemes is given at the end of this chapter.

The formal derivation of UCOM correlations functions obtained from a SRG evolution is presented in Chapter 3. The resulting correlation functions are discussed in detail. In addition, the determination of correlations functions obtained from energy minimization is discussed, and the resulting correlation functions are compared with the UCOM correlation functions throughout SRG calculations. Finally, the effects of the different correlations functions are discussed in NCSM as well as Hartree-Fock calculations.

Alternative SRG generators are the subject of Chapter 4. First, SRG transformations with an additional parameter, which restricts the momentum range the transformation acts on, are investigated. In this way, we aim to adapt the generator to modify the low-momentum, long-range components of the interaction as little as possible. Another straightforward modification is the replacement of the quadratic momentum operator in the generator by other functions of the momentum. The impact of these modifications on the momentum-space matrix-elements and deuteron wave-functions are investigated, and their effect on the convergence behaviour of NCSM calculations is studied.

In Chapter 5, the general approach of the unitary transformation of observables via UCOM and SRG is discussed. The transformation of radius and multipole operators is performed using both transformation methods. The results of many-body calculations with these transformed operators are compared to results with untransformed operators in quasi-exact (NCSM) and approximate methods (Hartree-Fock and RPA).

Concluding remarks and an outlook on further fields of study are given in Chapter 6.

In Appendix A the basic concepts of the Hartree-Fock approximation are summarized, and Appendix B introduces the RPA method. In Appendix C the transformation of the

two-body density matrix in harmonic oscillator representation is given as a starting point for unitary transformations.

Chapter 1

Nucleon-Nucleon Potentials

1.1 Argonne V18 Potential

Realistic nucleon-nucleon (NN) potentials are fitted to the experimental scattering data of protons and neutrons. One of these potentials is the Argonne V18 (AV18) potential [9]. It is designed to reproduce pp and np phase-shifts and deuteron properties very accurately. AV18 is composed of a one-pion exchange part, describing the long-range properties, a phenomenological medium- and short-range part, and an electromagnetic part:

$$V = V^\pi + V^R + V^{\text{EM}}. \quad (1.1)$$

The potential can be given in a general operator form

$$V_{ST} = \sum_p V_{ST}^p(r) O_p \quad (1.2)$$

with the 14 charge independent operators

$$O_p^{\text{CI}} = \{ \mathbb{1}, \boldsymbol{\tau}_1 \cdot \boldsymbol{\tau}_2, \boldsymbol{\sigma}_1 \cdot \boldsymbol{\sigma}_2, (\boldsymbol{\sigma}_1 \cdot \boldsymbol{\sigma}_2)(\boldsymbol{\tau}_1 \cdot \boldsymbol{\tau}_2), S_{12}, S_{12}(\boldsymbol{\tau}_1 \cdot \boldsymbol{\tau}_2), \mathbf{L} \cdot \mathbf{S}, \mathbf{L} \cdot \mathbf{S}(\boldsymbol{\tau}_1 \cdot \boldsymbol{\tau}_2), \mathbf{L}^2, \mathbf{L}^2(\boldsymbol{\tau}_1 \cdot \boldsymbol{\tau}_2), \mathbf{L}^2(\boldsymbol{\sigma}_1 \cdot \boldsymbol{\sigma}_2)(\boldsymbol{\tau}_1 \cdot \boldsymbol{\tau}_2), (\mathbf{L} \cdot \mathbf{S})^2, (\mathbf{L} \cdot \mathbf{S})^2(\boldsymbol{\tau}_1 \cdot \boldsymbol{\tau}_2) \}, \quad (1.3)$$

with the spin $\boldsymbol{\sigma}_i$ of the i th particle, the isospin $\boldsymbol{\tau}_i$ of the i th particle, the tensor operator S_{12} and the total spin \mathbf{S} and total angular momentum \mathbf{L} . They act in the same manner for pp , np and nn interactions. Additional four charge dependent and charge asymmetric terms

$$O_p^{\text{CD}} = \{ T_{12}, (\boldsymbol{\sigma}_1 \cdot \boldsymbol{\sigma}_2)T_{12}, S_{12}T_{12}, (\tau_{z1} + \tau_{z2}) \} \quad (1.4)$$

improving the agreement with pp and np scattering data are included as operators O_p

in equation (1.2). Here $T_{12} = 3\tau_{z1}\tau_{z2} - \boldsymbol{\tau}_1 \cdot \boldsymbol{\tau}_2$ is the isotensor operator.

Working with the (S, T) -projected part of the potential the phenomenological part is given by

$$V_{ST}^R = V_{ST}^c(r) + V_{ST}^t(r) S_{12} + V_{ST}^{ls}(r) \mathbf{L} \cdot \mathbf{S} + V_{ST}^{ls2}(r) (\mathbf{L} \cdot \mathbf{S})^2 + V_{ST}^{l2}(r) \mathbf{L}^2 \quad (1.5)$$

a central $V_{ST}^c(r)$, a tensor $V_{ST}^t(r)$, a spin-orbit $V_{ST}^{ls}(r)$, a quadratic spin-orbit $V_{ST}^{ls2}(r)$ and a quadratic angular momentum $V_{ST}^{l2}(r)$ component are contained. In this equation

$$S_{12} = \frac{3}{r^2} (\boldsymbol{\sigma}_1 \cdot \mathbf{r}) (\boldsymbol{\sigma}_2 \cdot \mathbf{r}) - \boldsymbol{\sigma}_1 \cdot \boldsymbol{\sigma}_2 \quad (1.6)$$

is the tensor operator and $\boldsymbol{\sigma}_n$ is the spin of the n th particle.

The radial dependencies in equation (1.5) can be expressed in a general form

$$V_{ST}^i(r) = I_{ST}^i T_\mu^2(r) + \left[P_{ST}^i + \mu r Q_{ST}^i + (\mu r)^2 R_{ST}^i \right] W(r), \quad (1.7)$$

with the Woods-Saxon function

$$W(r) = \left[1 + e^{(r-r_0)/a} \right]^{-1} \quad (1.8)$$

for the short-range core, the average pion mass $\mu = \frac{1}{3} (m_{\pi^0} + 2 m_{\pi^\pm})$, and the tensor function

$$T_\mu(r) = \left(1 + \frac{3}{\mu r} + \frac{3}{(\mu r)^2} \right) \frac{e^{-\mu r}}{\mu r} (1 - e^{-cr^2})^2. \quad (1.9)$$

I_{ST}^i , P_{ST}^i , Q_{ST}^i and R_{ST}^i are unknown parameters describing radial dependencies of each $V_{ST}^i(r)$. They have to be determined by fits to experimental data.

1.2 Chiral Potentials

In the past decade, Chiral Effective Field Theory (χ EFT) has emerged as a more systematic approach to derive nuclear interactions from Quantum Chromo Dynamics (QCD). This method is particularly appealing because it provides a consistent set of NN , $3N$, \dots interactions. In general EFTs are systematic low-energy approximations of more fundamental quantum field theories, which are suitable for the description of physical effects that do not depend on the substructure of the system. At higher energies these substructures become relevant and the description of the system with an EFT is no longer possible.

For the description of a nuclear force the relevant degrees of freedom have to be identified and the symmetries of QCD have to be fulfilled. Weinberg showed [26, 27] that the most general Lagrangian consistent with the symmetry principles, especially

the chiral symmetry, has to be considered to construct an EFT. The result will be the most general S-matrix consistent with the symmetries, analyticity, unitarity and the cluster decomposition principle.

In the case of QCD the spontaneous breaking of the chiral symmetry causes the transition to an effective level. Spontaneous symmetry breaking occurs when the ground-state has less symmetries than the Hamiltonian or Lagrangian describing the system. In QCD for massless systems, the quark fields can be decomposed in left- and right-handed components which transform independently under unitary rotations, e.g. under $SU_L(2) \times SU_R(2)$ transformations in the case of up and down quarks. The symmetry group can be re-expressed as a product of vectorial and axial transformations, $SU_V(2) \times SU_A(2)$, by taking linear combinations of left- and right-handed fields. At low energies the axial $SU_A(2)$ symmetry is spontaneously broken in the ground-state and only $SU_V(2)$ remains as the isospin symmetry [6]. The spontaneous symmetry breaking leads to the emergence of Goldstone bosons with the quantum numbers of the broken generators. These Goldstone bosons are identified as the lightest mesons π^0 and π^\pm [28]. The explicit breaking of chiral symmetry by the non-zero quark masses in the QCD Lagrangian is responsible for the experimentally measured non-zero pion masses.

Pions and nucleons are the relevant degrees of freedom for the description of a nuclear force. The interactions of Goldstone bosons vanish for zero momentum transfer and in the chiral limit for vanishing quark masses. This leads to a Lagrangian containing an infinite number of terms with an increasing number of derivatives, which can be organized by powers of $(Q/\Lambda_\chi)^\nu$. Here Q is the nucleon three-momentum or the pion four-momentum and Λ_χ the chiral symmetry breaking scale (breakdown scale) up to which the effective theory is valid [27]. The description of the chiral dynamics of hadrons at low energies is valid up to a scale Λ_χ , which is considered to be the mass of the ρ -meson, $m_\rho \approx 770\text{MeV}/c^2$, which is the lightest meson that cannot be identified as a Goldstone boson from chiral symmetry breaking.

To treat a two-nucleon system in χEFT , the Lagrangian is expanded in terms of powers of $1/m_N$, to account for the problem that the nucleon mass is not small compared to Λ_χ . This is the heavy baryon formulation of χEFT . With this formalism a Lagrangian for the description of a nuclear force can be derived. This Lagrangian contains terms describing the pion-pion interaction and other terms dealing with the pion-nucleon interaction. The expansion up to next-to-next-to-next-to leading order (N3LO) generates one pion exchange, two pion exchange and three pion exchange. $3N$ and $4N$ forces appear at N2LO and N3LO, respectively, where the contribution of the $2N$ force is much larger than of the $3N$ force which in turn is much larger than the $4N$ force, and so on. This ordering is due to the expansion in powers of Q/Λ_χ in the χEFT [7]. In [29] the $4N$ forces have been applied, using several approximations, to the ^4He binding energy, confirming the prediction that the effect of it is small in comparison to the full binding energy of this nucleus. A detailed calculation of the $4N$ force in the N3LO can be found in [30]. Nevertheless, one cannot extrapolate from the small effects of the $4N$ force in finite nuclei to nuclear matter [31]. The $3N$ force have a more significant effect which is for example shown in [32] for ab initio calculations using the $2N$ part

of the N3LO potential as well as the $2N$ part of the N2LO potential. In this thesis we will restrict our calculations to two-body potentials.

To obtain the NN potential the interaction terms of the Lagrangian are iterated up to a certain chiral order by means of a scattering equation. The full potential then consists of pion exchange terms V_π and contact terms V_{ct}

$$V = V_\pi + V_{\text{ct}}. \quad (1.10)$$

The potential terms are multiplied with a regulator function [33]

$$\exp \left[- \left(\frac{p}{\Lambda} \right)^{2n} - \left(\frac{p'}{\Lambda} \right)^{2n} \right]. \quad (1.11)$$

Here Λ is a cutoff parameter, p and p' , the initial and final nucleon momenta in the center-of-mass system. The exponent $2n$ is chosen large enough so that the regulator generates higher orders than the order at which the calculation is carried out.

The charge dependence due to the different pion masses, which is important for the description of low-energy pp and np data, and the Coulomb potential are included in the potential as well [27].

1.3 The Deuteron Wave-Function

The deuteron wave-functions are shown in Figure 1.1 for the N3LO potential from the Idaho group with a cutoff momentum of 500 MeV, the Argonne V18 interaction and additionally for the N3LO potential with a smoother, gaussian, cutoff (kindly provided to us by R. Machleidt). The latter will be referred to as N3LOS in the following.

The S-wave of the Argonne V18 and the N3LOS potential have a very similar shape and height. The N3LO S-wave in contrast is shifted to larger r . In the long-range region all three potentials have a similar behaviour. In the D-wave the Argonne V18 potential is higher than the two chiral potentials, which are also shifted towards larger distances. For the N3LO potential vague oscillations of the D-wave for large r can be observed. They probably result from the Fourier transform of the sharp form of the momentum cutoff in momentum space. This is eliminated in the N3LOS potential by construction, because these oscillations cause some problems in further calculations, as outlined in the following chapters. The D-wave of the N3LOS potential, however, has a negative contribution for small r . This observation shows, that the smoother cutoff causes the oscillations in the D-wave to vanish, but generates other effects. This might result from the construction of the potential, where the cutoff effects are not shifted towards higher orders of Q/Λ_χ .

The N3LOS potential will be used for calculations in Chapter 3.2 to investigate how its structure, caused by cutoff effects, will affect the calculations.

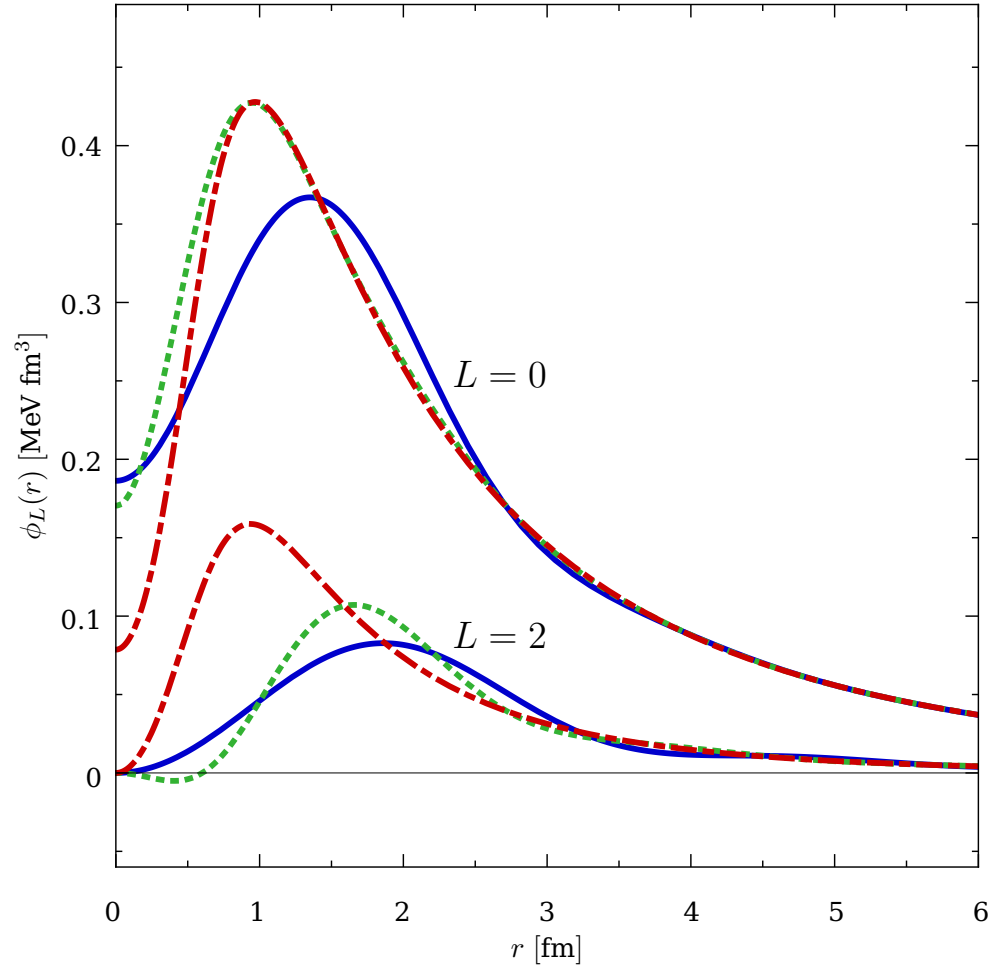


Figure 1.1: The deuteron S- (upper curves) and the D-wave-function (lower curves) for the N3LO (—), the N3LOS (·····) and the Argonne V18 potential (-.-.-).

Chapter 2

Effective Interactions

2.1 Unitary Correlation Operator Method

The main task in nuclear structure theory is to solve the nuclear many-body problem. In the ideal case it is solved *ab initio*, i.e., without any approximations. The computational effort restricts such methods to light nuclei. For the treatment of heavier nuclei the many-body Hilbert space has to be truncated to a much smaller subspaces, the heavier the nuclei become. This is problematic, because modern realistic interactions induce strong correlations, which already manifest in the deuteron solution. In the spin-projected two-body density distribution of the deuteron, shown in Figure 2.1, the effect of these correlations is illustrated. For small inter-particle distances the short-range repulsion of the interaction pushes the nucleons apart. Additionally a strong dependence on the relative distance and the spin alignments of the nucleons can be observed, which leads to the doughnut and dumbbell shapes for anti-parallel and parallel spins, respectively. This effect is caused by the action of the tensor force leading to a mixing of different orbital angular momenta.

In the Unitary Correlation Operator Method (UCOM) [34, 11, 35, 12] these correlations are imprinted onto a many-body state by means of a unitary transformation. The construction of the generators which handle the correlations and of the correlated interaction will be discussed in the following sections.

2.1.1 Basic Concept

The basic concept of the UCOM is to imprint the strong short-range and tensor correlations onto a many-body state by means of a unitary transformation. For that purpose a unitary operator C is introduced, transforming the initial many-body state $|\Psi\rangle$ or a bare operator O via

$$\langle \tilde{\Psi} | O | \tilde{\Psi}' \rangle = \langle \Psi | C^\dagger O C | \Psi \rangle = \langle \Psi | \tilde{O} | \Psi \rangle . \quad (2.1)$$

Depending on the requirements it can be chosen whether the state or the operator

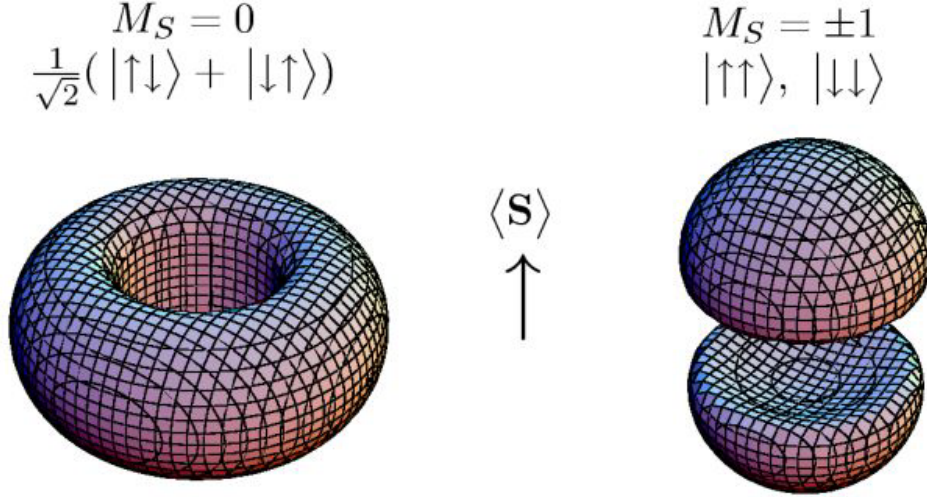


Figure 2.1: Two-body density of the deuteron calculated with the Argonne V18 potential projected onto antiparallel (left) and parallel (right) spins. Shown are the isodensity surfaces for $\rho_{1M_S}^{(2)} = 0.005\text{fm}^{-3}$, taken from [34].

should be transformed. The initial many-body state can be a Slater determinant in the simplest case. The resulting correlated state $|\tilde{\Psi}\rangle = C|\Psi\rangle$ is then no longer a single Slater determinant, but a superposition of Slater determinants.

In the UCOM framework the short-range central and the tensor correlations are treated separately, meaning that the correlation operator is a product of two operators

$$C = C_{\Omega} C_r. \quad (2.2)$$

Here C_{Ω} describes the short-range part of the tensor correlations, while C_r is responsible for the short-range central repulsion.

The correlation operators can be expressed as exponential functions with hermitian two-body generators

$$C = \exp \left[-i \sum_{i < j} g_{ij} \right]. \quad (2.3)$$

The detailed structure of the generator g is motivated by the physics of the central and tensor correlations, as discussed in the following sections.

2.1.2 Central Correlations

The repulsive core of the NN-interaction, which keeps the nucleons apart from each other, induces the short-range correlations which appear in the two-body density of the

correlated state as a correlation hole at small interparticle distances. To include these correlations in the many-body state a distance-dependent shift is introduced pushing nucleons apart whose distance is smaller than the radius of the repulsive core.

Radial shifts are generated by the projection of the relative momentum $\mathbf{q} = \frac{1}{2} [\mathbf{p}_1 - \mathbf{p}_2]$ onto the distance vector $\mathbf{r} = \mathbf{x}_1 - \mathbf{x}_2$ of the nucleons

$$q_r = \frac{1}{2} \left[\mathbf{q} \cdot \frac{\mathbf{r}}{r} + \frac{\mathbf{r}}{r} \cdot \mathbf{q} \right]. \quad (2.4)$$

The shift should be large for small distances to push the nucleons apart if their distance is smaller than the range of the repulsive core. For increasing distances, the generated shift should be small or zero to concentrate the nucleons in the attractive region of the potential. To achieve this behaviour, the shift-function $s(r)$ is introduced. Allowing separate shift-functions in the four (S, T) -channels, the generator for the central correlations now reads [11, 36]

$$g_r = \sum_{S,T} \frac{1}{2} [q_r s_{ST}(r) + s_{ST}(r) q_r] \Pi_{ST}, \quad (2.5)$$

where the operator Π_{ST} projects onto two-body spin S and isospin T .

2.1.3 Tensor Correlations

The tensor force induces correlations between the spins of two nucleons and their relative spatial orientation. For the description of the tensor correlations a spatial shift perpendicular to the radial direction has to be generated. The orbital part of the relative momentum operator is a suitable choice for that

$$\mathbf{q}_\Omega = \mathbf{q} - \frac{\mathbf{r}}{r} \cdot q_r = \frac{1}{2r^2} (\mathbf{L} \times \mathbf{r} - \mathbf{r} \times \mathbf{L}), \quad (2.6)$$

with the relative orbital angular momentum operator \mathbf{L} . The ansatz for the tensor generator including the dependence of the shift on the spin orientation is [35, 37, 11]

$$g_\Omega = \sum_T \frac{3}{2} \vartheta_T(r) [(\boldsymbol{\sigma}_1 \cdot \mathbf{q}_\Omega)(\boldsymbol{\sigma}_2 \cdot \mathbf{q}_r) + (\boldsymbol{\sigma}_1 \cdot \mathbf{q}_r)(\boldsymbol{\sigma}_2 \cdot \mathbf{q}_\Omega)] \Pi_{1T} = \vartheta(r) S_{12}(\mathbf{r}, \mathbf{q}_\Omega) \Pi_{1T}, \quad (2.7)$$

where $S_{12}(\mathbf{a}, \mathbf{b}) = \frac{3}{2} [(\boldsymbol{\sigma}_1 \cdot \mathbf{a})(\boldsymbol{\sigma}_2 \cdot \mathbf{b}) + (\boldsymbol{\sigma}_1 \cdot \mathbf{b})(\boldsymbol{\sigma}_2 \cdot \mathbf{a})] - \frac{1}{2}(\boldsymbol{\sigma}_1 \cdot \boldsymbol{\sigma}_2)(\mathbf{a} \cdot \mathbf{b} + \mathbf{b} \cdot \mathbf{a})$. The strength and radial dependence of the transverse shift of the nucleons is described by the tensor correlation function $\vartheta(r)$. It is constructed in analogy to the radial shift-function of the central correlations.

2.1.4 Correlated Wave Functions

The effect of the correlation operators can be illustrated by applying them to a two-body wave-function in coordinate-space representation. By construction only the relative wave-functions are affected by the correlation operators. For the uncorrelated states, LS -coupled angular momentum eigenstates are considered. Since the correlation operators do not depend on the magnetic quantum numbers M and M_T , they are omitted in the following.

The action of the central correlation operator $C_r = \exp(-ig_r)$ onto a two-body state in coordinate representation resembles a norm-conserving transformation of the radial wave-function [11]:

$$\langle r (L'S) JT | C_r | \phi (LS) JT \rangle = \frac{R_-(r)}{r} \sqrt{R'_-(r)} \phi(R_-(r)) \delta_{L'L} \quad (2.8)$$

$$\langle r (L'S) JT | C_r^\dagger | \phi (LS) JT \rangle = \frac{R_+(r)}{r} \sqrt{R'_+(r)} \phi(R_+(r)) \delta_{L'L}, \quad (2.9)$$

where the $\phi(r)$ are the uncorrelated radial wave-functions in coordinate space.

The correlation function $R_-(r)$ and its inverse $R_+(r)$ (where $R_\pm(R_\mp(r)) = r$) are connected to the shift-function $s(r)$ through

$$\int_r^{R_\pm(r)} \frac{d\xi}{s(\xi)} = \pm 1. \quad (2.10)$$

For slowly varying shift-functions the correlation function can be approximated by $R_\pm(r) \simeq r \pm s(r)$, i.e., two nucleons at a distance r to each other are shifted apart by the distance $s(r)$.

Application of the tensor correlation operator C_Ω to a LS -coupled two-body state has no effect for states with $L = J$. States with $L = J \pm 1$ are connected to states with $L = J \mp 1$. The tensor correlation function $\vartheta(r)$ controls the strength of the mixing [35]:

$$\langle r (L'S) JT | C_\Omega | \phi (LS) JT \rangle = \begin{cases} \phi(r) & L' = L = J \\ \cos[\theta_J(r)] \phi(r) & L' = L = J \pm 1 \\ \pm \sin[\theta_J(r)] \phi(r) & L' = J \pm 1, L = J \mp 1, \end{cases} \quad (2.11)$$

with the abbreviation $\theta_J(r) = 3\sqrt{J(J+1)} \vartheta(r)$.

The central and tensor correlated two-body wave-function in coordinate space is then given by

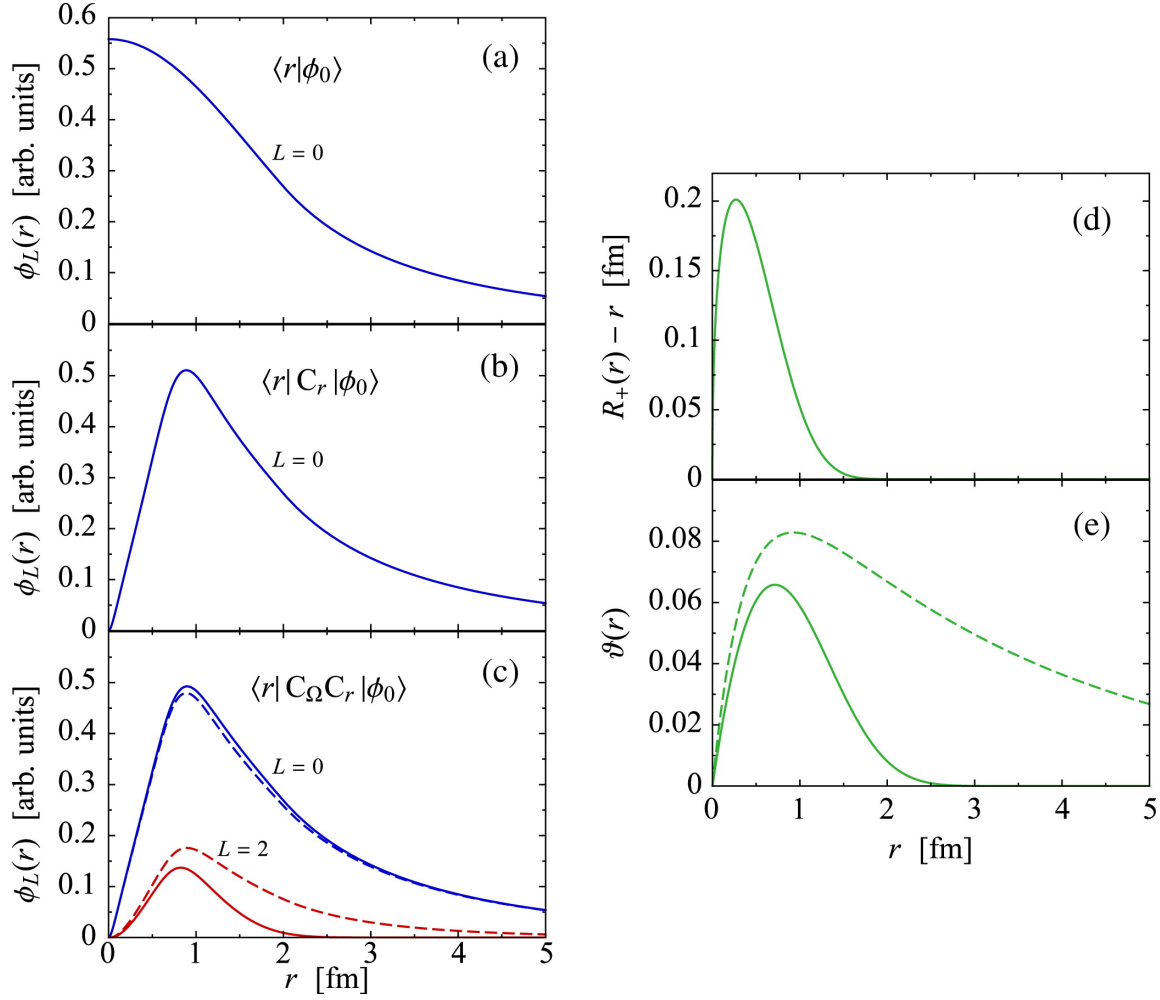


Figure 2.2: Starting with a uncorrelated trial wave-function (a). Application of the central correlator (d) leads to the wave-function (b). Supplementary application of the tensor correlator (e) yields the fully correlated wave-function (c), from [11].

$$\begin{aligned}
 & \langle r (L' S) JT | C_\Omega C_r | \phi (LS) JT \rangle \\
 &= \begin{cases} \frac{R_-(r)}{r} \sqrt{R'_-(r)} \phi(R_-(r)) & L' = L = J \\ \cos[\theta_J(r)] \frac{R_-(r)}{r} \sqrt{R'_-(r)} \phi(R_-(r)) & L' = L = J \pm 1 \\ \pm \sin[\theta_J(r)] \frac{R_-(r)}{r} \sqrt{R'_-(r)} \phi(R_-(r)) & L' = J \pm 1, L = J \mp 1. \end{cases} \quad (2.12)
 \end{aligned}$$

An uncorrelated state $|\phi_0(LS)JT\rangle = |\phi_0(01)10\rangle$, a s -wave state with the spin and isospin quantum numbers of the deuteron, is chosen as a starting point. In Figure 2.2(a) the uncorrelated $L = 0$ radial wave-function in this channel is shown. Applying the central correlator Fig. 2.2(d) leads to a wave-function with a correlation hole for short interparticle distances, Fig. 2.2(b). The additional application of the tensor correlator Fig. 2.2(e) generates the D-wave admixture in the wave-function, depending

on the tensor correlation function $\vartheta(r)$. The fully correlated wave-function is shown in Fig. 2.2(c). In order to generate a realistic deuteron wave-function the tensor correlation would have to be long-ranged as depicted with the dashed lines in the figure. The UCOM however, is designed to describe only the state-independent short-range correlations, while long-range correlations have to be described by the many-body model-space. This restriction leads to the tensor correlation function and the wave-function shown with the solid lines in Figure 2.2(e) and (c). The range constraint is discussed in Section 3.2.1 in detail.

2.1.5 Cluster Expansion

In the previous section correlated two-body states were discussed. The general equation for the correlation operators in the many-nucleon system contains the generator of the correlations in all possible nucleon pairs:

$$C_r = \exp \left[-i \sum_{i < j} g_{r,ij} \right], \quad C_\Omega = \exp \left[-i \sum_{i < j} g_{\Omega,ij} \right], \quad (2.13)$$

where $i, j = 1, \dots, A$. With this definition, the application of these operators to a state with a arbitrary particle number will generate up to A -body correlations. Such wave-functions become very complicated with increasing particle number. Therefore the unitarity of the correlation operators can be used to correlate operators instead of wave-functions. Transforming an arbitrary operator O gives a correlated operator containing up to A -body contributions.

Via a cluster expansion [34, 35]

$$\tilde{O} = C^\dagger O C = \sum_{k=1}^A \tilde{O}^{[k]} \quad (2.14)$$

the correlated operator can be decomposed into the irreducible part $\tilde{O}^{[k]}$ for particle number k , where for a n -body operator all irreducible contribution with $k < n$ vanish.

In practical calculations, the cluster expansion is truncated at two-body level, which will be referred to as the two-body approximation in the remainder of this work. The two-body approximation is meaningful for small densities and short correlation ranges, so that the range of the correlations is smaller than the mean particle distance.

2.1.6 Correlated Operators

For further investigations the correlation operators are applied to the many-body Hamiltonian containing a NN -interaction. The uncorrelated Hamiltonian for the A -body system is given by the sum of the kinetic energy operator T and a two-body potential V :

$$H = T + V = \sum_{i=1}^A \frac{1}{2\mu} \mathbf{q}_i^2 + \sum_{i>j=1}^A v_{ij}, \quad (2.15)$$

with the reduced nucleon mass μ .

For the rest of this chapter we will work in two-body space where for the NN -interaction the form [38]

$$V = \sum_p \frac{1}{2} (v_p(r) O_p + O_p v_p(r)) \quad (2.16)$$

is assumed for the purpose of this discussion, with

$$O_p \in \left\{ \mathbb{1}, \boldsymbol{\sigma}_1 \cdot \boldsymbol{\sigma}_2, q_r^2, q_r^2 \boldsymbol{\sigma}_1 \cdot \boldsymbol{\sigma}_2, \mathbf{L}^2, \mathbf{L}^2 \boldsymbol{\sigma}_1 \cdot \boldsymbol{\sigma}_2, \mathbf{L} \cdot \mathbf{S}, S_{12}\left(\frac{\mathbf{r}}{r}, \frac{\mathbf{r}}{r}\right), S_{12}(\mathbf{L}, \mathbf{L}) \right\} \otimes \{ \mathbb{1}, \tau_1 \cdot \tau_2 \} \quad (2.17)$$

(cf. (1.3)). This is sufficient to describe different realistic potentials, as the AV18 for example. The charge dependence is not considered here for the sake of simplicity. With this, the Hamiltonian can be written as

$$H = T_{\text{cm}} + T_{\text{rel}} + V, \quad (2.18)$$

with the kinetic energy split into a relative part

$$T_{\text{rel}} = T_r + T_\Omega = \frac{1}{2\mu} \left(q_r^2 + \frac{\mathbf{L}^2}{r^2} \right), \quad (2.19)$$

and a center-of-mass part

$$T_{\text{cm}} = \frac{1}{8\mu} (\mathbf{q}_1^2 + \mathbf{q}_2^2), \quad (2.20)$$

where the latter is not affected by the correlation operators.

Tensor Correlated Hamiltonian

To construct the correlated Hamiltonian in two-body space the application of the tensor correlator has to be accomplished. For that purpose the Baker-Campbell-Hausdorff expansion [38, 34] in two-body space

$$C_\Omega^\dagger O C_\Omega = \exp(\text{i}g_\Omega) O \exp(-\text{i}g_\Omega) = O + \text{i} [g_\Omega, O] + \frac{\text{i}^2}{2!} [g_\Omega, [g_\Omega, O]] + \dots \quad (2.21)$$

can be used. For some basic operators the series produces a finite number of terms,

but in general the expansion does not terminate.

The distance operator r for example commutes with the generator of the tensor correlations g_Ω and, therefore, stays unchanged in the transformation

$$C_\Omega^\dagger r C_\Omega = r. \quad (2.22)$$

For the quadratic radial momentum operator q_r^2 the first two terms of the Baker-Campbell-Hausdorff expansion remain. This leads to the correlated operator

$$C_\Omega^\dagger q_r^2 C_\Omega = q_r^2 - [\vartheta'(r)q_r + q_r\vartheta'(r)] S_{12}(\mathbf{r}, \mathbf{q}_\Omega) + [\vartheta'(r)S_{12}(\mathbf{r}, \mathbf{q}_\Omega)]^2, \quad (2.23)$$

with $S_{12}(\mathbf{r}, \mathbf{q}_\Omega) = 9 [\mathbf{S}^2 + 3(\mathbf{L} \cdot \mathbf{S}) + (\mathbf{L} \cdot \mathbf{S})^2]$.

For the other operators the full expansion is required. In first order the commutators

$$[g_\Omega, S_{12}(\frac{\mathbf{r}}{r}, \frac{\mathbf{r}}{r})] = i\vartheta(r) [-24\Pi_1 - 18(\mathbf{L} \cdot \mathbf{S}) + 3S_{12}(\frac{\mathbf{r}}{r}, \frac{\mathbf{r}}{r})] \quad (2.24)$$

$$[g_\Omega, (\mathbf{L} \cdot \mathbf{S})] = i\vartheta(r) [-\tilde{S}_{12}(\mathbf{q}_\Omega, \mathbf{q}_\Omega)] \quad (2.25)$$

$$[g_\Omega, \mathbf{L}^2] = i\vartheta(r) [2\tilde{S}_{12}(\mathbf{q}_\Omega, \mathbf{q}_\Omega)] \quad (2.26)$$

$$[g_\Omega, S_{12}(\mathbf{L}, \mathbf{L})] = i\vartheta(r) [7\tilde{S}_{12}(\mathbf{q}_\Omega, \mathbf{q}_\Omega)], \quad (2.27)$$

are obtained with the abbreviation

$$\tilde{S}_{12}(\mathbf{q}_\Omega, \mathbf{q}_\Omega) = 2r^2 S_{12}(\mathbf{q}_\Omega, \mathbf{q}_\Omega) + S_{12}(\mathbf{L}, \mathbf{L}) - \frac{1}{2} S_{12}(\frac{\mathbf{r}}{r}, \frac{\mathbf{r}}{r}). \quad (2.28)$$

This new tensor operator in turn generates further operators in the next order of the Baker-Campbell-Hausdorff expansion. To obtain a closed representation for the tensor correlated operators the number of new operators has to be truncated, e.g., by considering only operators of up to fourth order in momentum of the Baker-Campbell-Hausdorff expansion [11].

Fully Correlated Hamiltonian and the Correlated Interaction V_{UCOM}

The application of the central correlator to the tensor correlated Hamiltonian is simpler, because it can be evaluated analytically for all relevant operators. With the transformation properties in coordinate space, as introduced in Section 2.1.4, the two-body approximation of the central correlated operators can be obtained.

Applying the central correlator C_r to the distance operator r gives

$$C_r^\dagger r C_r = R_+(r), \quad (2.29)$$

which resembles a coordinate transformation. Here $R_+(r)$ is the correlation function as introduced in Section 2.1.4. Due to the unitarity of the central correlation operator the transformation of an arbitrary distance-dependent function reads

$$C_r^\dagger f(r) C_r = f\left(C_r^\dagger r C_r\right) = f\left(R_+(r)\right). \quad (2.30)$$

This affects the radial dependencies of the different contributions in the NN -interaction. Additionally, the components of the radial momentum q and the quadratic radial momentum q_r^2 are modified, where the transformation of the latter generates a local potential in addition to the state-dependent part

$$C_r^\dagger q_r^2 C_r = \frac{1}{2} \left\{ \frac{1}{R_+(r)^2} q_r^2 + q_r^2 \frac{1}{R'_+(r)^2} \right\} + \frac{7}{4} \frac{R''_+(r)^2}{R'_+(r)^4} - \frac{1}{2} \frac{R'''_+(r)}{R'_+(r)^3} \quad (2.31)$$

All other operators appearing in the Baker-Campbell-Hausdorff expansion are invariant under the transformation with the central correlation operator.

By combining and applying the central and tensor correlated operators discussed before, a correlated many-body Hamiltonian is obtained. In two-body approximation, see Section 2.1.5, the Hamiltonian reads:

$$\tilde{H} = T^{[1]} + T^{[2]} + V^{[2]} = T + V_{\text{UCOM}}. \quad (2.32)$$

The one-body contribution is the uncorrelated kinetic energy $T = T^{[1]}$. Its two-body contributions are the correlated kinetic energy $T^{[2]}$ and the correlated potential $V^{[2]}$. Their sum defines the correlated interaction V_{UCOM} , which can be written in operator form as [11]

$$V_{\text{UCOM}} = \sum_p \frac{1}{2} \left[\tilde{v}_p(r) \tilde{O}_p + \tilde{O}_p \tilde{v}_p(r) \right], \quad (2.33)$$

like the underlying bare NN -interaction. Here the operators \tilde{O}_p are

$$\begin{aligned} \tilde{O}_p = \left\{ \mathbb{1}, \boldsymbol{\sigma}_1 \cdot \boldsymbol{\sigma}_2, q_r^2, q_r^2 \boldsymbol{\sigma}_1 \cdot \boldsymbol{\sigma}_2, \mathbf{L}^2, \mathbf{L}^2 \boldsymbol{\sigma}_1 \cdot \boldsymbol{\sigma}_2, \mathbf{L} \cdot \mathbf{S}, S_{12}\left(\frac{\mathbf{r}}{r}, \frac{\mathbf{r}}{r}\right), S_{12}(\mathbf{L}, \mathbf{L}), \right. \\ \left. \tilde{S}_{12}(\mathbf{q}_\Omega, \mathbf{q}_\Omega), q_r S_{12}(\mathbf{r}, \mathbf{q}_\Omega), L^2(\mathbf{L} \cdot \mathbf{S}), L^2 \tilde{S}_{12}(\mathbf{q}_\Omega, \mathbf{q}_\Omega), \dots \right\} \otimes \{\mathbb{1}, \tau_1 \cdot \tau_2\}. \end{aligned} \quad (2.34)$$

This list includes operators appearing in the Baker-Campbell-Hausdorff expansion up to the third order. Contributions in higher orders are indicated by the dots. In general it is sufficient to work with the contributions up to the third order [35, 37].

In general, the UCOM is not restricted to the transformation of the Hamiltonian, it can be applied to other observables as well. The transformation of these observables has

to be performed in consistent way. In the Chapter 5 this is discussed for charge radii and multipole momenta.

2.1.7 Correlated Matrix-Elements

For many-body calculations the two-body matrix-elements of the correlated interaction are required. These matrix-elements are obtained by calculating the matrix-elements directly by using the operator representation of the interaction V_{UCOM} . The radial integrals can be evaluated analytically by expanding the radial dependencies of the operator channels in sums of gaussians. The tensor correlations are applied to the states, because then the truncation due to the Baker-Campbell-Hausdorff expansion, introduced in the previous section, can be avoided. The central correlator in contrast will be applied to the Hamiltonian.

For the application of the tensor correlator to the states the order of central and tensor operator in the definition of the correlated matrix-elements have to be interchanged:

$$C_r^\dagger C_\Omega^\dagger H C_r C_\Omega = (C_r^\dagger C_\Omega^\dagger C_r) C_r^\dagger H C_r (C_r^\dagger C_r C_\Omega) = \tilde{C}_\Omega^\dagger C_r^\dagger H C_r \tilde{C}_\Omega, \quad (2.35)$$

with the correlated tensor correlation operator

$$\tilde{C}_\Omega = C_r^\dagger C_r C_\Omega = \exp(-i\vartheta(R_+(r))S_{12}(\mathbf{r}, \mathbf{q}_\Omega)). \quad (2.36)$$

For LS - coupled states with $L = J$ the correlated tensor operator acts like the identity operator and the coupling of states with $L = J \pm 1$ with states with $L = J \mp 1$ is given by [11]

$$\langle r (L'S) JT | C_\Omega | \phi (LS) JT \rangle = \begin{cases} \phi(r) & L' = L = J \\ \cos[\tilde{\theta}_J(r)]\phi(r) & L' = L = J \pm 1 \\ \pm \sin[\tilde{\theta}_J(r)]\phi(r) & L' = J \pm 1, L = J \mp 1, \end{cases} \quad (2.37)$$

where

$$\tilde{\theta}_J(r) = 3\sqrt{J(J+1)}\vartheta(R_+(r)). \quad (2.38)$$

These relations allow for an exact calculations of the two-body matrix-elements.

2.2 Similarity Renormalization Group

The basic concept of the Similarity Renormalization Group (SRG) [39, 13, 14, 40] was developed by Glazek and Wilson who applied it to light-front field theory [15]. At the same time Wegner found a method to diagonalize or at least band-diagonalize

Hamiltonians [39]. As shown by Szpigel and Perry [41], both concepts are equivalent. In the SRG formalism the short-range properties of an interaction are handled by a pre-diagonalization of a matrix representation of the Hamiltonian in a given basis, leading to a band-diagonal interaction. This is achieved by solving a renormalization group flow-equation.

2.2.1 Formal Derivation

Starting with Wegners flow-equation formulation of the SRG [39], the many-body Hamiltonian of a system is transformed towards a diagonal form with respect to a given basis. This transformation has to be performed consistently for other observables as well. An application of the SRG to the momentum occupation number operator can be found in [25]. A detailed discussion of the SRG evolution of charge radii and multipole transition strengths and momenta is worked out in Chapter 5.

For the flow parameter α the evolution of the initial Hamiltonian H_0 is governed by the flow-equation

$$\frac{dH_\alpha}{d\alpha} = [\eta_\alpha, H_\alpha], \quad (2.39)$$

where $H_\alpha = T_{\text{int}} + V_\alpha$ is the SRG-evolved Hamiltonian with the many-body interaction V_α and the α -independent intrinsic kinetic energy $T_{\text{int}} = T - T_{\text{cm}}$. The evolution of the initial Hamiltonian H_0 with a flow parameter α can be written as a unitary transformation

$$H_\alpha = U_\alpha^\dagger H_0 U_\alpha. \quad (2.40)$$

From equations (2.39) and (2.40) an equation defining the generator η_α can be extracted:

$$\eta_\alpha = \frac{dU_\alpha}{d\alpha} U_\alpha^\dagger = -\eta_\alpha^\dagger. \quad (2.41)$$

The generator has to be chosen appropriately for the application of interest. The original choice of Wegner [39] for the anti-hermitian generator η_α was

$$\eta_\alpha = [\text{diag}(H_\alpha), H_\alpha]. \quad (2.42)$$

If the Hamiltonian commutes with its diagonal part in a given basis, the generator η_α vanishes and the evolution has reached a fixed point. This is only possible if H_α is diagonal in that basis.

Another, widely applied, ansatz for the generator was suggested by Szpigel and Perry [41] and later adopted by Bogner et al. [14]. For the evolution a generator containing the relative kinetic energy T_{rel} instead of the diagonal part of H_α is used:

$$\eta_\alpha = (2\mu)^2 [T_{\text{rel}}, H_\alpha] . \quad (2.43)$$

This generator will be used in the following discussion. There are, of course, many other possibilities for the choice of η_α . Some other generators are investigated in Chapter 4.

During the flow, the off-diagonal matrix-elements of the Hamiltonian are suppressed continuously [39, 18]. The side-effect of this diagonalization is, that during the flow complicated many-body interactions are generated, even for an initial two-body interaction. This can be seen by decomposing the Hamiltonian in second-quantized form. In a very schematic way the SRG flow-equation (2.39) with the generator (2.42) can be written as

$$\frac{dH_\alpha}{d\alpha} = \left[\left[\sum a^\dagger a^\dagger aa, \sum a^\dagger a^\dagger aa \right], \sum a^\dagger a^\dagger aa \right] \quad (2.44)$$

$$= \sum a^\dagger a^\dagger aa + \sum a^\dagger a^\dagger a^\dagger aaa + \dots , \quad (2.45)$$

where the initially used two-body Hamiltonian obtains higher-body contributions during the evolution. For a more detailed discussion of the SRG flow-equation in second quantization see for example [42].

Wegner showed [39], by solving the flow-equation for each particle number separately, that the one-body equation does not depend on the flow parameter, while an A -body equations depends on particle numbers equal to or less than A .

In this thesis all calculations are performed in a two-body approximation, therefore the flow-equation (2.44) has to be truncated at this level. This is analogous to the two-body approximation of the cluster expansion in the UCOM framework (c.f. Section 2.1.5). Calculations with induced three-body contributions are presented in recent works [43, 44, 45].

2.2.2 Evolution of Two-Body Matrix-Elements in Momentum-Space

Confining the evolution to two-body space, where the higher order contributions are discarded in the evolved interaction, the generator (2.43) reads

$$\eta_\alpha = (2\mu)^2 [T_{\text{rel}}, H_\alpha] = 2\mu [\mathbf{q}^2, H_\alpha] = 2\mu [\mathbf{q}^2, T_{\text{rel}} + V_\alpha] , \quad (2.46)$$

with the relative kinetic energy $T_{\text{rel}} = \frac{1}{2\mu} \mathbf{q}^2$. The prefactor $(2\mu)^2$ of the commutator, with the reduced nucleon mass μ , is chosen such that the dimension of the flow parameter α is fm^4 . The flow-equation now reads

$$\frac{dH_\alpha}{d\alpha} = 2\mu [[\mathbf{q}^2, H_\alpha], H_\alpha] . \quad (2.47)$$

Decomposing the square of the two-body relative momentum operator into a radial and an angular part leads to

$$\mathbf{q}^2 = q_r^2 + \frac{\mathbf{L}^2}{r^2}, \quad \text{with} \quad q_r = \frac{1}{2} \left(\mathbf{q} \cdot \frac{\mathbf{r}}{r} + \frac{\mathbf{r}}{r} \cdot \mathbf{q} \right). \quad (2.48)$$

This shows that one fixed point of the flow given by equation (2.47) is a two-body Hamiltonian that commutes with q_r^2 and with $\frac{\mathbf{L}^2}{r^2}$. In a partial-wave momentum-space basis $|q(LS)JT\rangle$ the Hamiltonian is band-diagonalized with respect to the relative momentum (q, q') and the orbital angular momentum (L, L') .

The flow-equation for the uncoupled partial-waves with $L = L' = J$ reads

$$\begin{aligned} \frac{dV_\alpha(q, q')}{d\alpha} &= -(q^2 - q'^2)^2 V_\alpha(q, q') \\ &+ 2\mu \int dQ Q^2 (q^2 + q'^2 - 2Q^2) V_\alpha(q, Q) V_\alpha(Q, q'), \end{aligned} \quad (2.49)$$

where

$$V_\alpha(q, q') = \langle q(LS)JT | V_\alpha | q'(LS)JT \rangle. \quad (2.50)$$

In this case charge-independence and rotational symmetry are assumed for the interaction, i.e. the matrix-elements do not depend on M and M_T . These quantum numbers are omitted in the following, but we use M_T -dependent matrix-elements for all applications.

For channels with $S = 1$ and $L, L' = J \pm 2$ the mixing of the angular momenta couples matrix-elements for the different combinations of $L = J \pm 1$ and $L' = J \mp 1$. The flow-equation of the coupled-channel can be obtained by replacing $V_\alpha(q, q')$ of equation (2.49) with a matrix $\mathcal{V}_\alpha(q, q')$, i.e.

$$\begin{aligned} \frac{d\mathcal{V}_\alpha(q, q')}{d\alpha} &= -(q^2 - q'^2)^2 \mathcal{V}_\alpha(q, q') \\ &+ 2\mu \int dQ Q^2 (q^2 + q'^2 - 2Q^2) \mathcal{V}_\alpha(q, Q) \mathcal{V}_\alpha(Q, q'), \end{aligned} \quad (2.51)$$

with

$$\mathcal{V}_\alpha(q, q') = \begin{pmatrix} V_\alpha^{LL}(q, q') & V_\alpha^{LL'}(q, q') \\ V_\alpha^{L'L}(q, q') & V_\alpha^{L'L'}(q, q') \end{pmatrix}, \quad (2.52)$$

where $V_\alpha^{LL'}(q, q') = \langle q(LS)JT | V_\alpha | q'(L'S)JT \rangle$. The SRG-evolution is performed for each non-coupled partial-wave and each set of coupled partial-waves separately.

2.2.3 SRG and the Deuteron

The SRG evolution has a strong impact on the deuteron wave-function. This effect can be seen in Figure 2.3 in case of the AV18 interaction and in Figure 2.4 for the N3LO interaction, where the wave-functions and for comparison also the momentum-space matrix-elements are shown for the unevolved and the SRG-evolved effective interaction for $\alpha = 0.08 \text{ fm}^4$.

In the matrix-elements of the initial potential the strong off-diagonal contributions couple low- and high-momentum components in the wave-functions. During the flow the large off-diagonal matrix-elements are suppressed and pushed towards the diagonal with increasing flow parameter. In the $^3\text{S}_1$ partial-wave the attraction in the low-momentum region has increased significantly. One effect, which can be observed more strongly for the AV18 interaction than for the N3LO interaction, is the accumulation of repulsive strength on the diagonal in the high-momentum area, see for example [46, 17].

The band-diagonalization of the matrix, reducing the contributions of the short-range correlations has a significant effect on the wave-functions. During the flow the correlation hole in the $L = 0$ radial wave-function is completely removed by the evolution. The $L = 2$ admixture is reduced, i.e., the effect of the short-range correlations is diminished.

Comparing the SRG-evolved wave-functions with the UCOM correlated wave-functions for the AV18 potential in Figure 2.2 shows, that both methods describe short-range correlations by means of a unitary transformation. In the UCOM the correlations are imprinted onto the many-body state, while in the SRG the correlations are obtained by the transformation of the Hamiltonian.

The suppression of the tensor part and the elimination of the correlation hole are general effects in both methods which occur for both SRG-evolved interactions. A UCOM transformation of the N3LO potential is not possible with the usual parameterizations for the correlation functions used so far. This procedure and some proposals for new parameterizations, which allow the construction of correlation functions for the N3LO potential, are discussed in Chapter 3.2. The suppression of the D-wave also leads to smaller quadrupole moments. A consistent unitary transformation of this observable is necessary to correct for the effects caused by the transformation of the interaction. The discussion and results are summarized in Chapter 5.

2.3 SRG and UCOM

Both, the UCOM and the SRG make use of unitary transformations of the Hamiltonian to decouple low-lying and high-lying momenta and to handle the short-range correlations which are induced by the underlying potential. In the UCOM generators for the central and the tensor correlations are constructed explicitly. The SRG on the other hand aims for a pre-diagonalization of the momentum-space matrix-elements in

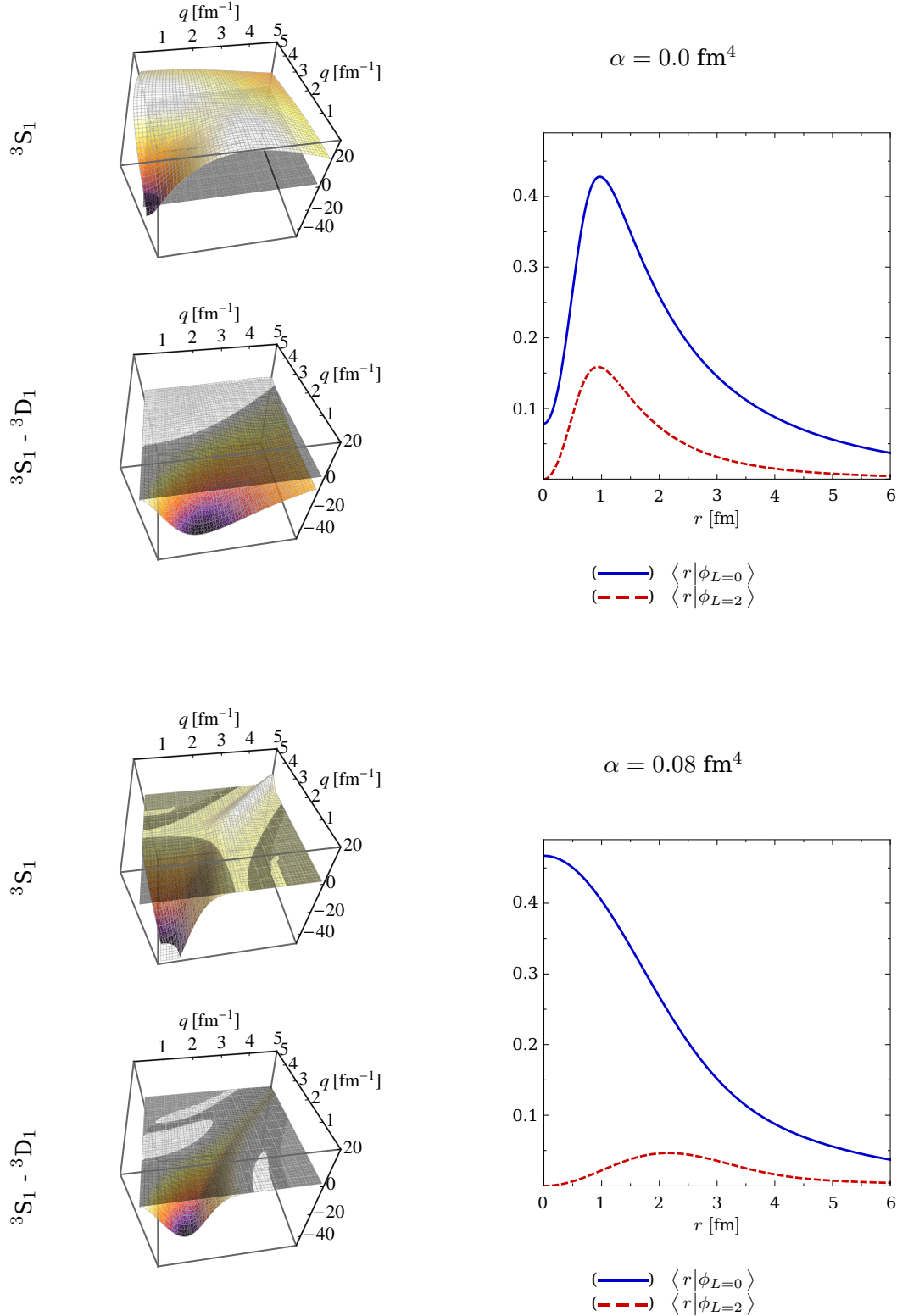


Figure 2.3: Momentum-space matrix-elements (in units of MeV fm^3) and deuteron wave-functions of the SRG-evolved AV18 potential for $\alpha = 0.0 \text{ fm}^4$ (top) and 0.08 fm^4 (bottom). Note the different scale for the matrix-elements of the unevolved 3S_1 partial-wave.

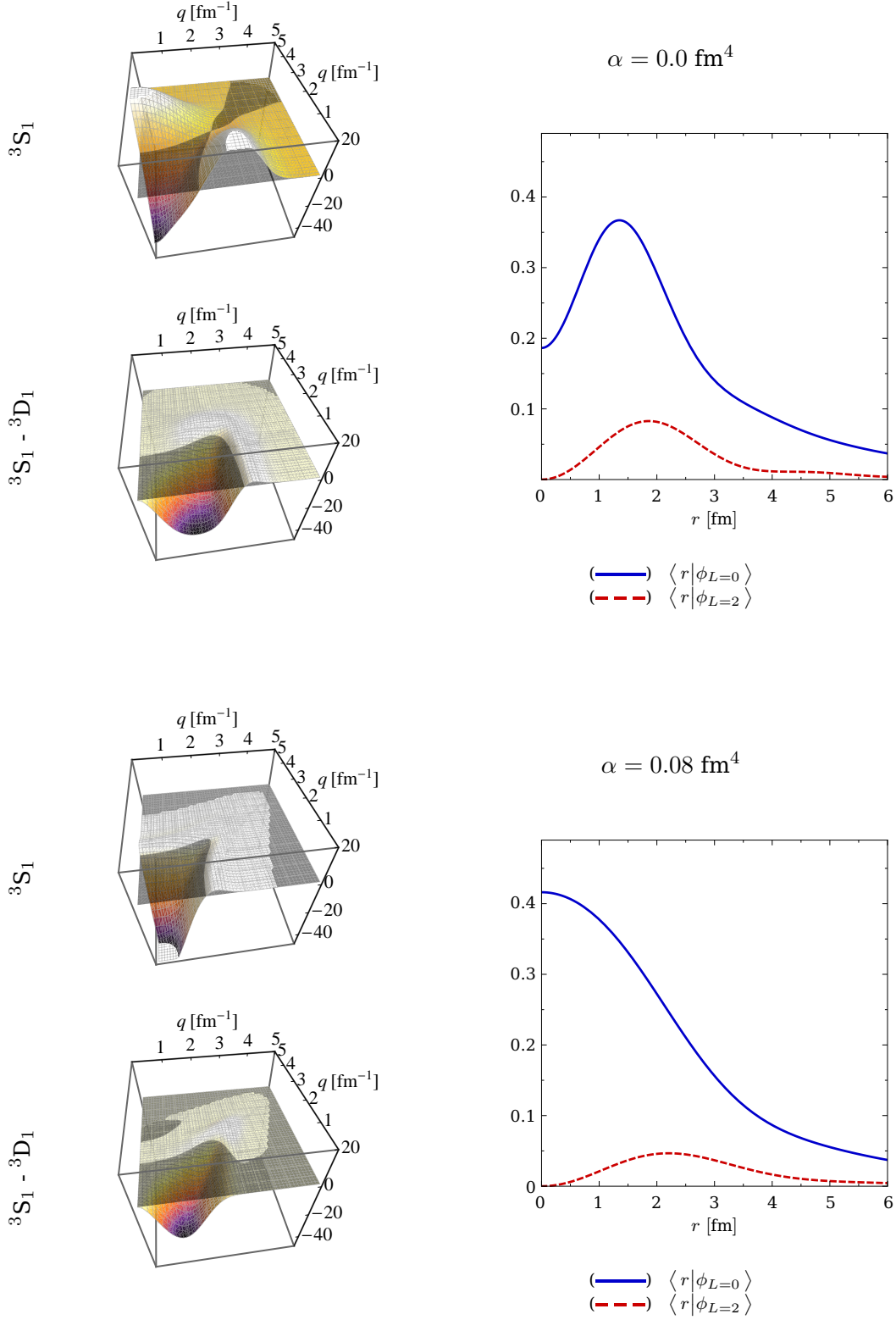


Figure 2.4: Momentum-space matrix-elements (in units of MeV fm^3) and deuteron wave-functions of the SRG-evolved N3LO potential for $\alpha = 0.0 \text{ fm}^4$ (top) and 0.08 fm^4 (bottom).

a partial-wave representation by solving a renormalization group flow-equation.

Because both methods exhibit many similarities, a comparison and a study of their connection on a formal level is in order.

2.3.1 Comparison of the Methods

The relation of the generators of the UCOM and of the SRG are examined in more detail in the following.

The operator form of the AV18 potential (see Section 1.1)

$$V = \sum_p V_p(r) O_p, \quad (2.53)$$

is chosen for the following investigations, but the charge-dependent operators are omitted for the sake of simplicity. Evaluating the SRG generator (2.46) at $\alpha = 0.0 \text{ fm}^4$ and splitting the relative kinetic energy in a radial and an angular part, the initial generator is given by

$$\eta_0 = \frac{1}{2\mu} \left[q_r^2 + \frac{\mathbf{L}^2}{r^2}, V \right]. \quad (2.54)$$

This commutator can be split into one commutator for the operator q_r^2 and one for $\frac{\mathbf{L}^2}{r^2}$. The first is given by

$$[q_r^2, V] = \sum_p [q_r^2, V_p(r) O_p] = -i \sum_p (q_r V_p'(r) + V_p'(r) q_r) O_p, \quad (2.55)$$

because q_r commutes with all operators O_p . In the angular part only the tensor component of the interaction does not commute with \mathbf{L}^2 , leading to

$$\left[\frac{\mathbf{L}^2}{r^2}, V \right] = \left[\frac{\mathbf{L}^2}{r^2}, V_t(r) S_{12}\left(\frac{\mathbf{r}}{r}, \frac{\mathbf{r}}{r}\right) \right] = -4i \frac{V_t(r)}{r^2} S_{12}(\mathbf{r}, \mathbf{q}_\Omega). \quad (2.56)$$

With these results the initial SRG-generator

$$\eta_0 = \frac{i}{2} (q_r S(r) + S(r) q_r) + i \Theta(r) S_{12}(\mathbf{r}, \mathbf{q}_\Omega) \quad (2.57)$$

is obtained, with

$$S(r) \equiv -\frac{1}{\mu} \left(\sum_p V_p'(r) O_p \right) \quad (2.58)$$

and

$$\Theta(r) \equiv -\frac{2}{\mu} \frac{V_t(r)}{r^2}. \quad (2.59)$$

The generator η_0 has the same structure as the sum of the UCOM generators g_r (2.5) and g_Ω (2.7). The symmetrized radial momentum q_r and the momentum-dependent tensor operator $S_{12}(\mathbf{r}, \mathbf{q}_\Omega)$, which are constructed in the UCOM framework to mimic the structure of the short-range correlations, result from the commutation relation that defines the generator of the flow. This connects the intuitive picture of central and tensor correlation of the UCOM framework with the one of the SRG flow.

A difference of the methods is, that in the SRG transformation the operator valued function $S(r)$ depends on the spin-isospin channel as well as the partial-wave, while in the UCOM the function $s(r)$ does not depend on the partial-wave. A UCOM transformation for each partial-wave with a corresponding correlation function would be necessary to emulate the behaviour of the SRG. Another difference is that the UCOM transformation of the Hamiltonian is static, performed in a single step. In contrast, the SRG transformation is dynamical and adapts the generator at each step of the flow, which obliterates the structural similarity of the generators which acquires a more and more complicated structure throughout the evolution. Moreover, the UCOM introduces separate generators for central and tensor correlations, while the SRG does not distinguish between the types of the correlations. In the SRG method the two types of correlations are entangled which may cause a shift to larger scales on which the central correlations are transferred from the potential to the wave-function.

Chapter 3

Determination of UCOM Correlation Functions

3.1 SRG-Generated UCOM

The formal connection of UCOM and SRG, derived in the previous chapter shows that the SRG can reproduce the generators included in the UCOM approach. A next logical step is to derive the UCOM correlation functions from the SRG evolution [18, 47, 17, 11]. To achieve this, the SRG flow-equation is solved for a given interaction up to a flow parameter α . This leads to momentum-space matrix-elements $V_\alpha(q, q')$ for a certain partial-wave. With these matrix-elements the two-body problem is solved to determine eigenstates. The lowest two-body eigenstate of the SRG-evolved interaction is mapped onto the corresponding state of the initial interaction in the respective partial-wave by a UCOM transformation and thus, UCOM correlation functions are obtained.

3.1.1 Extracting UCOM Correlation Functions from SRG

We start with the two-body eigenstates $|\Phi^{(0)}\rangle$ of the initial potential, and $|\Phi^{(\alpha)}\rangle$ of the SRG-evolved one, both with the same energy eigenvalue. The idea is now to construct a UCOM correlation function mapping the SRG-evolved state onto the initial state:

$$|\Phi^{(0)}\rangle = C |\Phi^{(\alpha)}\rangle = C_\Omega C_r |\Phi^{(\alpha)}\rangle. \quad (3.1)$$

Considering non-coupled partial-waves with $L = J$, where only the central correlator acts, the two-body states for the initial and the SRG-evolved interaction can be written as

$$\begin{aligned} |\Phi^{(0)}\rangle &= |\phi^{(0)}(LS)JT\rangle \\ |\Phi^{(\alpha)}\rangle &= |\phi^{(\alpha)}(LS)JT\rangle, \end{aligned} \quad (3.2)$$

respectively.

From equations (2.9) and (3.1) an equation for determining the central correlation function $R_-(r)$ is obtained, with real-valued wave-functions:

$$\phi^{(0)}(r) = \frac{R_-(r)}{r} \sqrt{R'_-(r)} \phi^{(\alpha)}(R_-(r)). \quad (3.3)$$

Since the wave-functions are known, $R_-(r)$ can be evaluated by integrating equation (3.3):

$$R_-^3(r) = 3 \int_0^r dr' r'^2 \frac{[\phi^{(0)}(r')]^2}{[\phi^{(\alpha)}(R_-(r'))]^2}. \quad (3.4)$$

This integral equation for $R_-(r)$ can be solved in an iterative way for any considered partial-wave.

For coupled partial-waves with $L = J + 1$ and $L' = J - 1$ central and tensor correlations appear simultaneously. The two-body eigenstates of the initial and SRG-evolved interaction

$$\begin{aligned} |\Phi^{(0)}\rangle &= |\phi_L^{(0)}(LS)JT\rangle + |\phi_{L'}^{(0)}(L'S)JT\rangle \\ |\Phi^{(\alpha)}\rangle &= |\phi_L^{(\alpha)}(LS)JT\rangle + |\phi_{L'}^{(\alpha)}(L'S)JT\rangle \end{aligned} \quad (3.5)$$

are used as an ansatz. For the correlation functions in coordinate-space representation (2.12), a set of coupled equations is obtained

$$\begin{pmatrix} \phi_L^{(0)}(r) \\ \phi_{L'}^{(0)}(r) \end{pmatrix} = \frac{R_-(r)}{r} \sqrt{R'_-(r)} \begin{pmatrix} \cos \theta_J(r) & \sin \theta_J(r) \\ -\sin \theta_J(r) & \cos \theta_J(r) \end{pmatrix} \begin{pmatrix} \phi_L^{(\alpha)}(R_-(r)) \\ \phi_{L'}^{(\alpha)}(R_-(r)) \end{pmatrix}, \quad (3.6)$$

with the correlation functions $R_-(r)$ and $\theta_J(r) = 3\sqrt{J(J+1)}\vartheta(R_-(r))$. Formal integration of this equation, as for the uncoupled partial-waves, will not lead to a satisfying result, because the equations depend on the unknown central and tensor correlation functions. Therefore the correlation functions will be extracted separately in the following.

The $\theta_J(r)$ -part is affected by the central correlation function $R_-(r)$ in the same manner for each equation. To eliminate it, the sum of the squares of the wave-functions is considered

$$[\phi_L^{(0)}(r)]^2 + [\phi_{L'}^{(0)}(r)]^2 = \frac{R_-^2(r)}{r^2} R'_-(r) \left([\phi_L^{(\alpha)}(R_-(r))]^2 + [\phi_{L'}^{(\alpha)}(R_-(r))]^2 \right). \quad (3.7)$$

In analogy to the uncoupled case, the central correlation function can now be determined by a formal integration:

$$R_-^3(r) = 3 \int_0^r dr' r'^2 \frac{[\phi_L^{(0)}(r')]^2 + [\phi_{L'}^{(0)}(r')]^2}{[\phi_L^{(\alpha)}(R_-(r'))]^2 + [\phi_{L'}^{(\alpha)}(R_-(r'))]^2}. \quad (3.8)$$

Inserting this relation for the central correlation function into the equations (3.6), which have to be fulfilled simultaneously, the tensor correlation function can be extracted

$$\begin{aligned} \phi_L^{(0)}(r) = & \frac{R_-(r)}{r} \sqrt{R'_-(r)} \left\{ \cos(\theta_J(r)) \phi_L^{(\alpha)}(R_-(r)) \right. \\ & \left. + \left[-\frac{\phi_{L'}^{(0)}(r) r}{R_-(r) \sqrt{R'_-(r)}} + \cos(\theta_J(r)) \phi_{L'}^{(\alpha)}(R_-(r)) \right] \frac{\phi_{L'}^{(\alpha)}(R_-(r))}{\phi_L^{(\alpha)}(R_-(r))} \right\}. \end{aligned} \quad (3.9)$$

This equation has pairs of symmetric solutions due to the symmetry properties of the cosine function. The correct value for $\theta_J(r)$ is obtained by reinserting the solution of equation (3.9) into equation (3.6) to check the agreement between the UCOM transformed wave-functions and the SRG-evolved ones.

For the implementation of this mapping procedure, discretized wave-functions are used. The SRG transformation of a two-body momentum-space Hamiltonian for a given partial-wave is performed on the sufficiently large grid. With these discretized matrix-elements the two-body problem is solved on the same grid in momentum-space for the respective partial-wave. After transforming the ground-state wave-functions to coordinate space they can be inserted in equation (3.4) in case of uncoupled states and in equation (3.8) for coupled states, to calculate the discretised central correlation function $R_-(r)$. Numerical inversion leads to the correlation function $R_-(r)$. The tensor correlation functions are then obtained by evaluating equation (3.9).

For the determination of the correlation functions only the two-body ground-state for the given partial-wave has been used. This is an arbitrary choice, in practice other states in the two-body spectrum can be used here. However, it shows that using a low-lying excited state instead of the ground-state does not change the correlation functions significantly [17].

3.1.2 SRG-Generated UCOM Correlation Functions

To stay close to the UCOM framework the SRG-generated correlation functions are calculated for different channels of spin S and isospin T , rather than for each partial-wave separately. They are optimized for a given (S, T) -channel for the lowest J partial-wave, because these partial-waves are affected most by short-range correlations, while the relative wave-functions are strongly suppressed by the centrifugal barrier for higher L .

For the determination of the central correlation function $R_+(r)$ in the spin-singlet

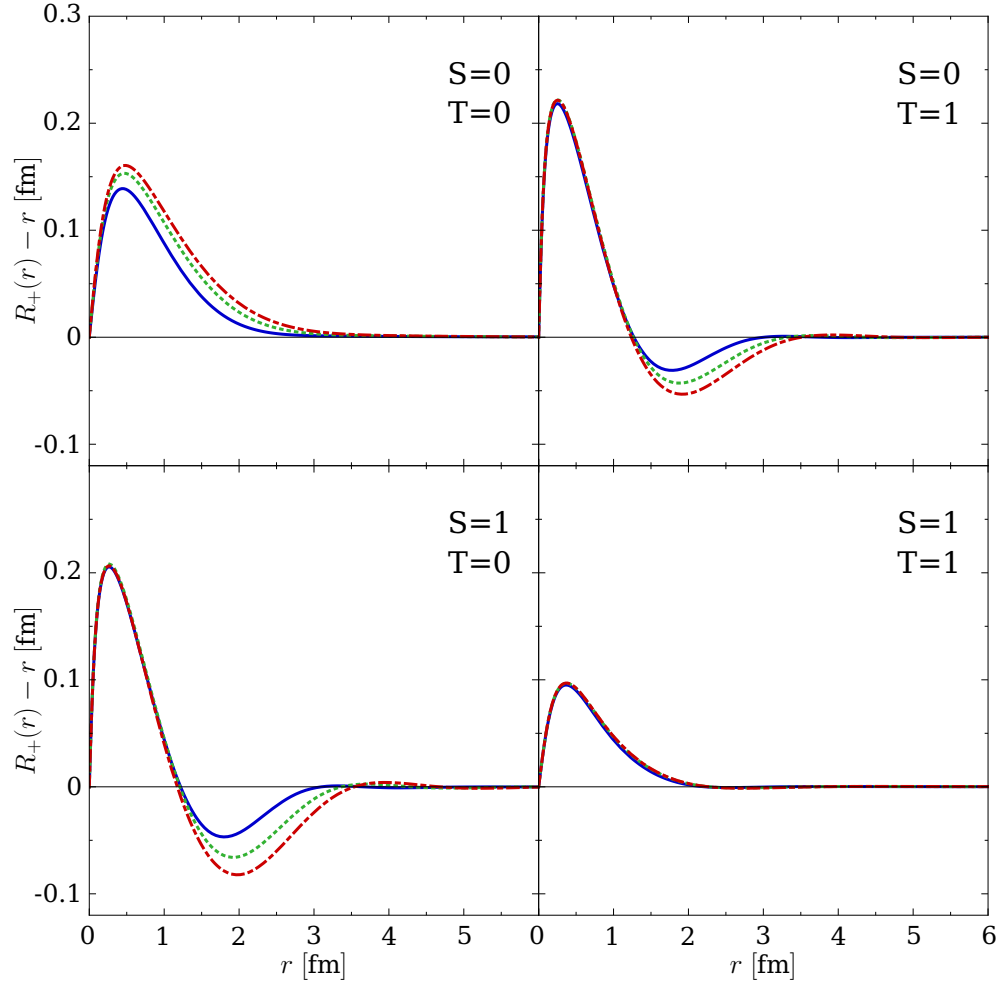


Figure 3.1: SRG-generated UCOM central correlation functions for the AV18 potential for different spin and isospin channels. The curves correspond to the flow parameters $\alpha = 0.02 \text{ fm}^4$ (—), 0.04 fm^4 (·····), and 0.06 fm^4 (- - -).

channels the 1S_0 partial-wave is used for $T = 0$ and the 1P_1 partial-wave for $T = 1$. The central and tensor correlation functions in the spin-triplet channels are extracted from the deuteron solution in the coupled 3S_1 - 3D_1 partial-wave for $T = 0$. For $T = 1$ the lowest possible orbital angular momentum is $L = 1$, so the total angular momentum can be $J = 0, 1, 2$. One possibility to handle this channel is to use only the coupled 3P_2 - 3F_2 partial-wave as done in [18, 17]. In this case the central correlation functions are not adapted to the partial-waves with small J very well. Therefore, a scheme dealing with all possible J values is required to determine the central correlation functions. In practice they are obtained by averaging the 3P_0 , 3P_1 and 3P_2 partial-waves weighted with $2J + 1$.

The SRG-generated UCOM central correlation functions for the AV18 potential for the different (S, T) -channels are shown in Figure 3.1 for different values for α . The corresponding tensor correlation functions for these flow parameters are shown in

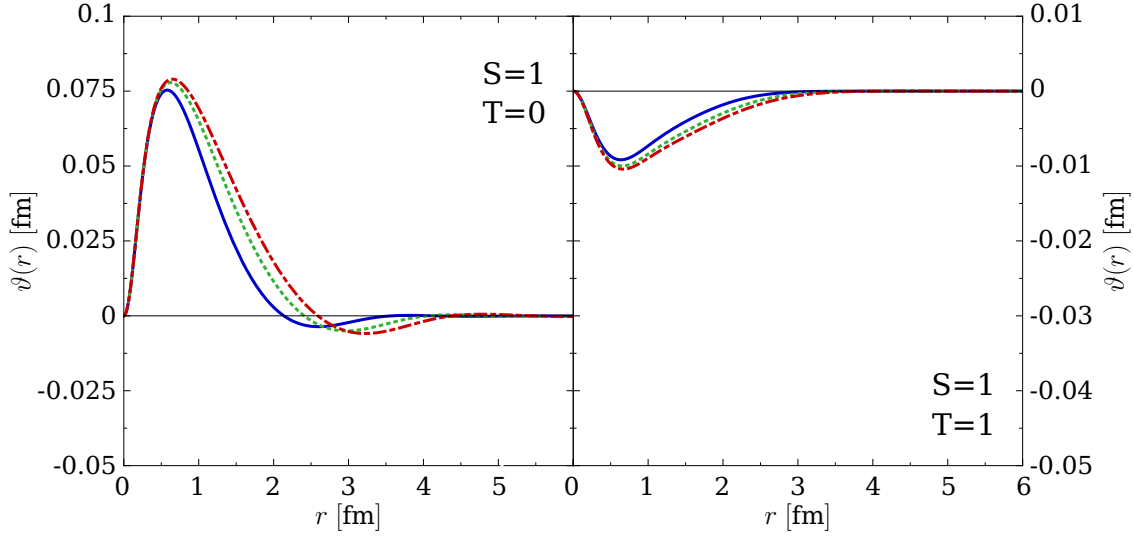


Figure 3.2: SRG-generated UCOM tensor correlation functions for the AV18 potential for different isospin channels. The curves correspond to the flow parameters $\alpha = 0.02 \text{ fm}^4$ (—), 0.04 fm^4 (⋯), and 0.06 fm^4 (-.-). Note the different scales for the two channels.

Figure 3.2. The range of the correlation functions is connected to the flow parameter α , the larger the value of α the longer is the range of the correlation functions. In the flow picture this can be understood intuitively. The SRG evolution starts with the suppression of matrix-elements for high momenta, i.e., small inter-particle distances, and as the flow progresses, matrix-elements for smaller momenta are affected as well and driven towards the diagonal. In coordinate space this means that the wave-functions are modified at intermediate and longer distances, leading to longer ranged correlation functions. For the $(S, T) = (0, 1)$ and $(S, T) = (1, 0)$ -channels the correlation functions have a negative contribution, where the effect of increasing flow parameter is more significant than in the positive part at small distances. In the $(S, T) = (1, 1)$ -channel the central correlation function is much weaker than in the other channels. The tensor correlation function in this channel is completely negative and very weak.

The SRG-generated correlation functions for the N3LO potential are shown in Figure 3.3 for the central correlation function and in Figure 3.4 for the tensor correlation function. In comparison to the AV18 potential the correlation functions are much weaker, except for the central correlation functions of the $(S, T) = (1, 0)$ -channel. A possible explanation for this effect is that the N3LO potential is softer than the AV18 to begin with. In the matrix-elements the off-diagonal parts of the N3LO potential are not as strong as for the AV18 potential, but this cannot explain why the central correlation function for $(S, T) = (1, 0)$ is not weaker than for the AV18 potential. Moreover, we observe α -dependence in all regions of the correlation function, not just in the long-range part as for the AV18 potential. Another significant difference are the strong oscillations, especially in the $(S, T) = (1, 0)$ -channel. The tensor correlation functions

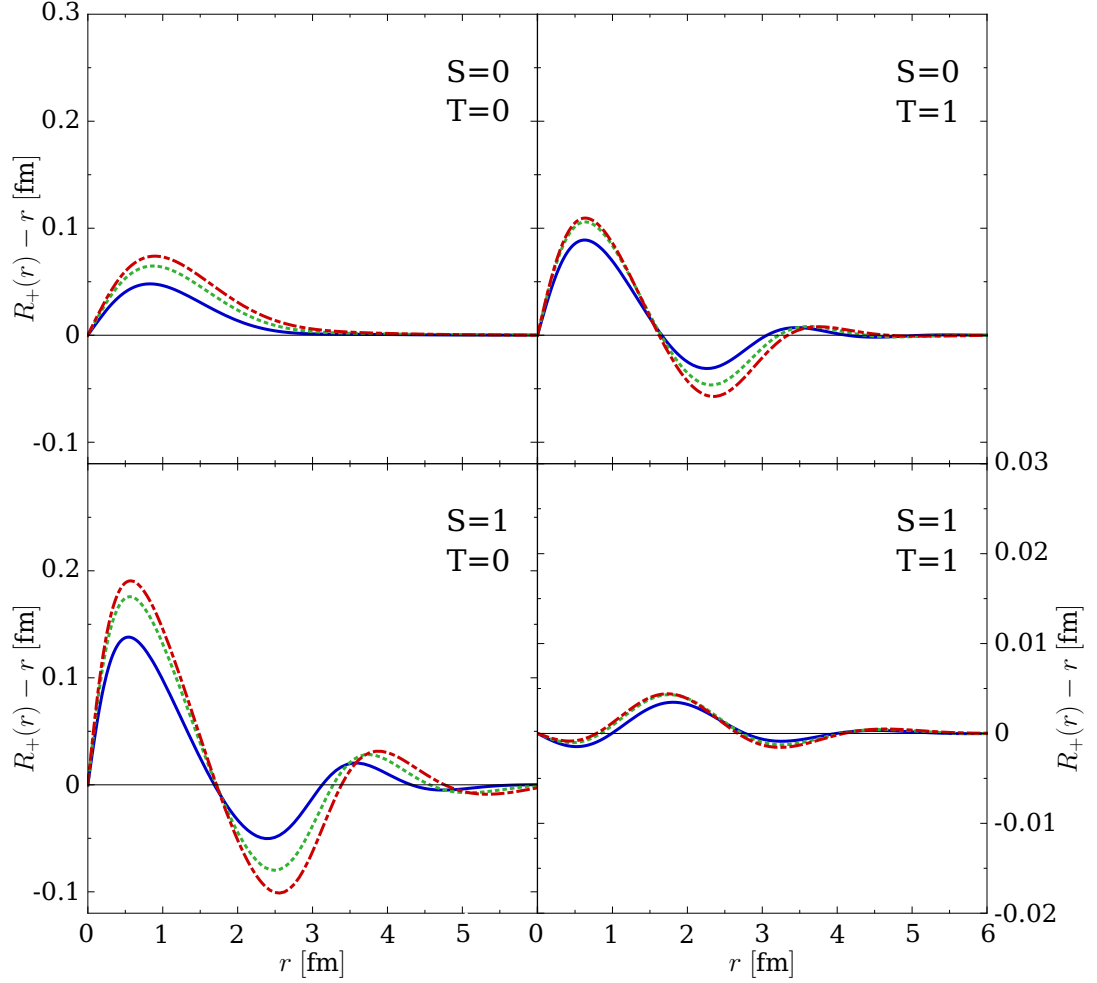


Figure 3.3: SRG-generated UCOM central correlation functions for the N3LO potential for different spin and isospin channels. The curves correspond to the flow parameters $\alpha = 0.02 \text{ fm}^4$ (—), 0.04 fm^4 (---), and 0.06 fm^4 (-.-.-). Note the different plot range for the $(S, T) = (1, 1)$ -channel.

in this channel also show a dip in the middle of the first peak besides the long-ranged oscillations. In fact, the first peak seems to consist of two fragments which merge during the flow. The long-ranged oscillations are an unwanted effect, because the aim of a UCOM effective interaction is to describe only the short-range corrections. These oscillations for large distances originate from the oscillations observed in the wave-functions of the N3LO potential which are mentioned in Section 1.2.

The correlation functions for the N3LOS potential are shown in Figure 3.5 for the central part and in Figure 3.6 for the tensor part. For $(S, T) = (0, 0)$ the correlation function has a similar structure as the correlation functions of the other potentials, but for small distances there is a kink in the function, directly after a very sharp increase. This artifact is caused by the construction of the mapping, which has problems handling the

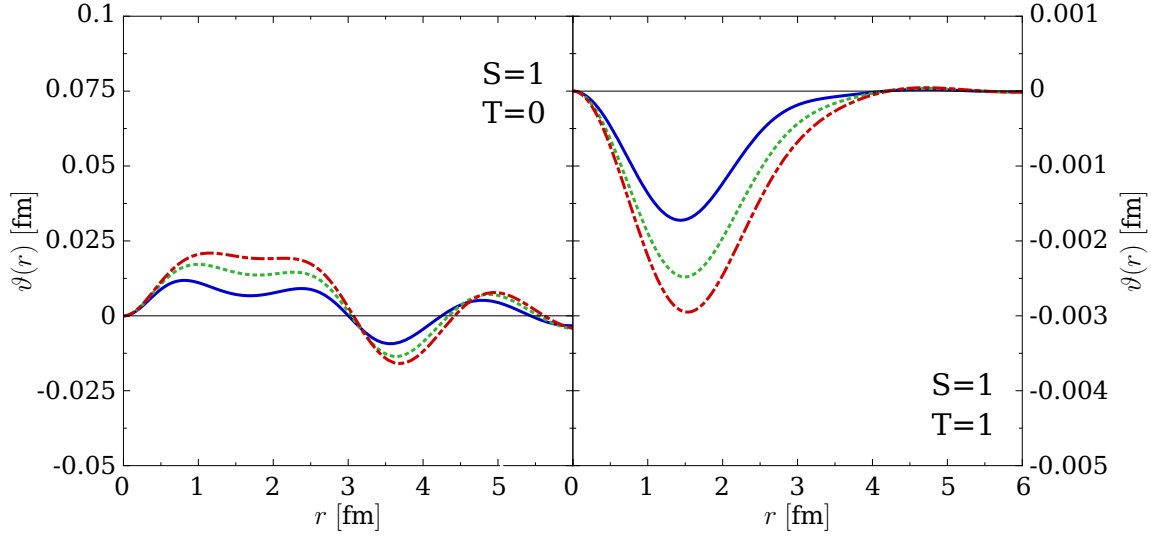


Figure 3.4: SRG-generated UCOM tensor correlation functions for the N3LO potential for different isospin channels. The curves correspond to the flow parameters $\alpha = 0.02 \text{ fm}^4$ (—), 0.04 fm^4 (---), and 0.06 fm^4 (-.-.-). Note the different plot ranges.

rapid changes of the gradients of the obtained curves in that region. The slope of the curve negative part central of the correlation function for $(S, T) = (0, 1)$ decreases at about 2 fm. This is an effect generated by the wave-function of the N3LOS potential, see Section 1.2, which is strongly oscillating in the D-wave. The central correlation functions in the other two channels show more similarities to the correlation functions for the N3LO potential. The tensor correlation function for the $(S, T) = (1, 0)$ -channel is strongly oscillating, for the $(S, T) = (1, 1)$ -channel the tensor correlation function is very weak and has a very broad peak which again may be caused by the oscillations of the wave-function.

These correlation functions show, that both, the N3LOS potential and the N3LO potential generate correlation functions which are long-ranged with an oscillatory behaviour. Looking at the discussion in Chapter 1 for the behaviour of the wave-functions, the oscillations are not surprising, because in both cases they occur already in the wave-functions. Since the N3LOS does not provide any systematic improvement to the N3LO potential it will not be used for further investigations in this thesis.

3.2 Optimization of UCOM Correlation Functions

The UCOM correlation functions introduced in Section 2.1, should be constructed in such a way that they are state-independent, i.e., that they only depend on the underlying bare potential but not on specific nuclei or many-body states [35, 48]. For that purpose the state-dependent and state-independent features have to be disen-

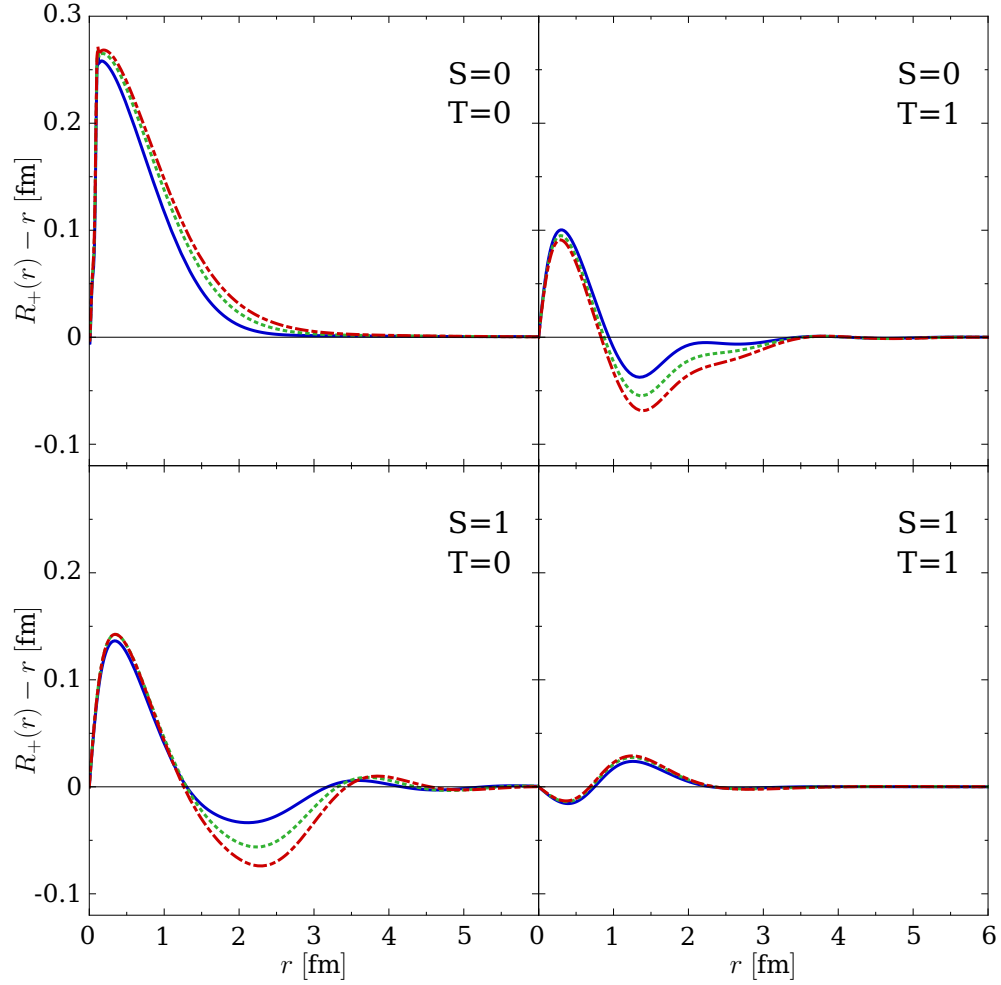


Figure 3.5: SRG-generated UCOM central correlation functions for the N3LOS potential for different spin and isospin channels. The curves correspond to the flow parameters $\alpha = 0.02 \text{ fm}^4$ (—), 0.04 fm^4 (·····), and 0.06 fm^4 (-.-.-).

tangled, i.e., the long- and short-range correlations have to be resolved. Additionally they should only describe short-range correlations, while the long-range correlations should be described by the many-body method. In Figure 2.2 the tensor correlations in the $(S, T) = (1, 0)$ -channel are long ranged which is against the idea of the UCOM. In that case a tensor correlation function has to be found which disentangles short-range and long-range correlations where the latter should be described by the many-body states.

In case of the AV18 potential, the central correlations are restricted to short ranges automatically, because of the repulsive core which provides a short-ranged scale. For the tensor correlations there is no such separation of scales and, therefore, the UCOM transformation has to disentangle the short ranges from the long ranges by construction [38]. The N3LO potential is softer than the AV18 leading to a less pronounced,

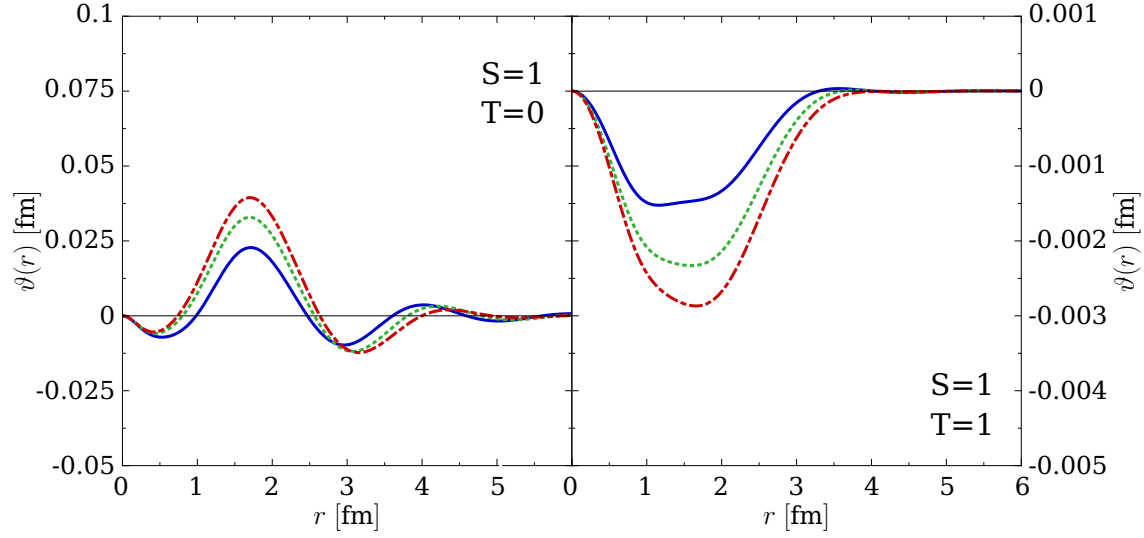


Figure 3.6: SRG-generated UCOM tensor correlation functions for the N3LOS potential for different isospin channels. The curves correspond to the flow parameters $\alpha = 0.02 \text{ fm}^4$ (—), 0.04 fm^4 (·····), and 0.06 fm^4 (-.-.-). Note the different plot ranges in the two channels.

broader core region. Therefore there is no natural decoupling scale of short- and long-range central and tensor correlations for this potential. This is similar for the SRG, where only one parameter is used for the evolution of the interaction. Here the central and tensor correlations are coupled in the generator and it is not possible to decouple them. Nevertheless, it was shown in [49] for the AV18 and the N3LO potential, that during the SRG evolution the repulsive core is eliminated first and later, with higher flow parameter, the long-range contributions become modified.

3.2.1 Correlation Functions by Energy Minimization

A method to determine the correlation functions is based on energy-minimization in the two-body system. The correlated energy expectation value for the lowest partial-wave in each spin-isospin channel is calculated with a trial state for each (S, T) -channel separately. As the uncorrelated trial state should be independent of the short-range correlations, a possible choice is the free zero-energy scattering solution $\phi_L(r) \propto r^L$ [38, 11].

For the central correlation functions two different parameterization have proven appropriate in the past [34, 11]:

3.2. OPTIMIZATION OF UCOM CORRELATION FUNCTIONS

S	T	Param.	α [fm]	β [fm]	γ [fm]	η
0	0	II	0.7971	1.2638	0.4621	-
0	1	I	1.3793	0.8853	-	0.3724
1	0	I	1.3265	0.8342	-	0.4471
1	1	II	0.5665	1.3888	0.1786	-

Table 3.1: Parameter set A0 of the central correlation functions $R_+(r)$ in the different spin-isospin channels for the AV18 potential [11].

$$R_+^I(r) = r + \alpha \left(\frac{r}{\beta} \right)^\eta \exp \left\{ -\exp \left\{ \frac{r}{\beta} \right\} \right\}, \quad (3.10)$$

$$R_+^{II}(r) = r + \alpha \left(1 - \exp \left\{ \frac{r}{\gamma} \right\} \right) \exp \left\{ -\exp \left\{ \frac{r}{\beta} \right\} \right\}. \quad (3.11)$$

For the four different (S, T) -channels the parameterization of $R_+(r)$ leading to the lower energy expectation value will be used. Since the potential is purely repulsive in the $(S, T) = (0, 0)$ -channel, leading to long-ranged correlation functions, the constraint

$$I_{R_+} = \int dr r^2 (R_+(r) - r) \quad (3.12)$$

is introduced. It is fixed to $I_{R_+} = 0.1 \text{ fm}^4$ in this channel for the AV18 potential to restrict the range of the correlation function to a similar value as in the other (S, T) -channels. Table 3.1 summarizes the parameters for the central correlation functions for the AV18 potential. These parameters will be referred to as parameter set A0 in the following.

The tensor correlation function for the $S = 1$ channels is parameterized by

$$\vartheta(r) = \alpha \left(1 - \exp \left\{ -\frac{r}{\gamma} \right\} \right) \exp \left\{ -\exp \left\{ \frac{r}{\beta} \right\} \right\}. \quad (3.13)$$

The range of the tensor correlation function is controlled by using

$$I_\vartheta = \int dr r^2 \vartheta(r) \quad (3.14)$$

to restrict the correlation to short ranges, to ensure that only the short-range correlations are covered by the UCOM transformation, while the long-range correlations are treated by the many-body state.

As already discussed for the SRG-generated UCOM correlation functions in Section 3.1, the optimization in the $(S, T) = (1, 1)$ channel is carried out by a superposition of three energy expectation values with relative weights of $2J + 1$ [11].

S	T	I_ϑ [fm ³]	α	β [fm]	γ [fm]
1	0	0.09	536.67	1.2608	1000.0
1	1	-0.09	-0.0569	2.1874	1.4761

Table 3.2: Parameter set A0 of the tensor correlation functions $\vartheta(r)$ in the different spin-isospin channels for the AV18 potential [11].

The parameters for the tensor correlation functions for the AV18 potential for parameter set A0 are given in Table 3.2.

In Figure 3.7 the correlation functions for the AV18 potential obtained with parameter set A0 are plotted. The correlation functions in the $(S, T) = (0, 0)$ and $(S, T) = (1, 1)$ channels are weaker and longer ranged than the correlation functions in the $(S, T) = (0, 1)$ and $(S, T) = (1, 0)$ channels. This effect is caused by the centrifugal barrier. In Figure 3.8 the corresponding tensor correlation functions are shown. The tensor correlation functions are weaker than the central correlation functions. In the $(S, T) = (1, 1)$ channel the correlation function is very weak and also negative.

3.2.2 Other Parameterizations for UCOM Correlation Functions

The parameterizations for the UCOM correlation functions described in Section 3.2.1 work quite well for the AV18 potential. But comparing the structure of these correlation functions with the SRG-generated UCOM correlation functions, pictured in Figures 3.1 and 3.2, shows a significant difference: the shown SRG-generated UCOM central correlation functions $R_+(r) - r$ and the tensor correlation functions have negative contributions in some channels. Such structures cannot be produced with the parameterizations (3.10) and (3.11) for the central correlations and (3.13) for the tensor part. To investigate the effect of the negative contributions, these parameterizations have to be adapted to allow such structures. One possible parameterization to mimic the behavior of the SRG-generated UCOM correlation functions is

$$R_+^{\text{cos}}(r) = r + \alpha \left(\frac{r}{\beta} \right)^\eta \exp \left\{ -\exp \left\{ \frac{r}{\beta} \right\} \right\} \cos \left(\frac{r}{\delta} \right) \quad (3.15)$$

for the central correlations. The tensor correlation function is then given by

$$\vartheta^{\text{cos}}(r) = \alpha \left(1 - \exp \left\{ -\frac{r}{\gamma} \right\} \right) \exp \left\{ -\exp \left\{ \frac{r}{\beta} \right\} \right\} \cos \left(\frac{r}{\delta} \right). \quad (3.16)$$

The correlation functions are now determined by energy minimization with these parameterizations. In the $(S, T) = (0, 0)$ channel none of the considered potentials produce SRG-generated UCOM correlation functions which show a negative contribution, therefore parameterization (3.10) is used for this channel to stay close to the SRG-generated UCOM correlation functions. The range constraints I_{R_+} and I_ϑ can be extracted from the SRG-generated UCOM correlation functions via equation (3.12) and (3.14). These values are chosen as a vague reference for the beginning. The results

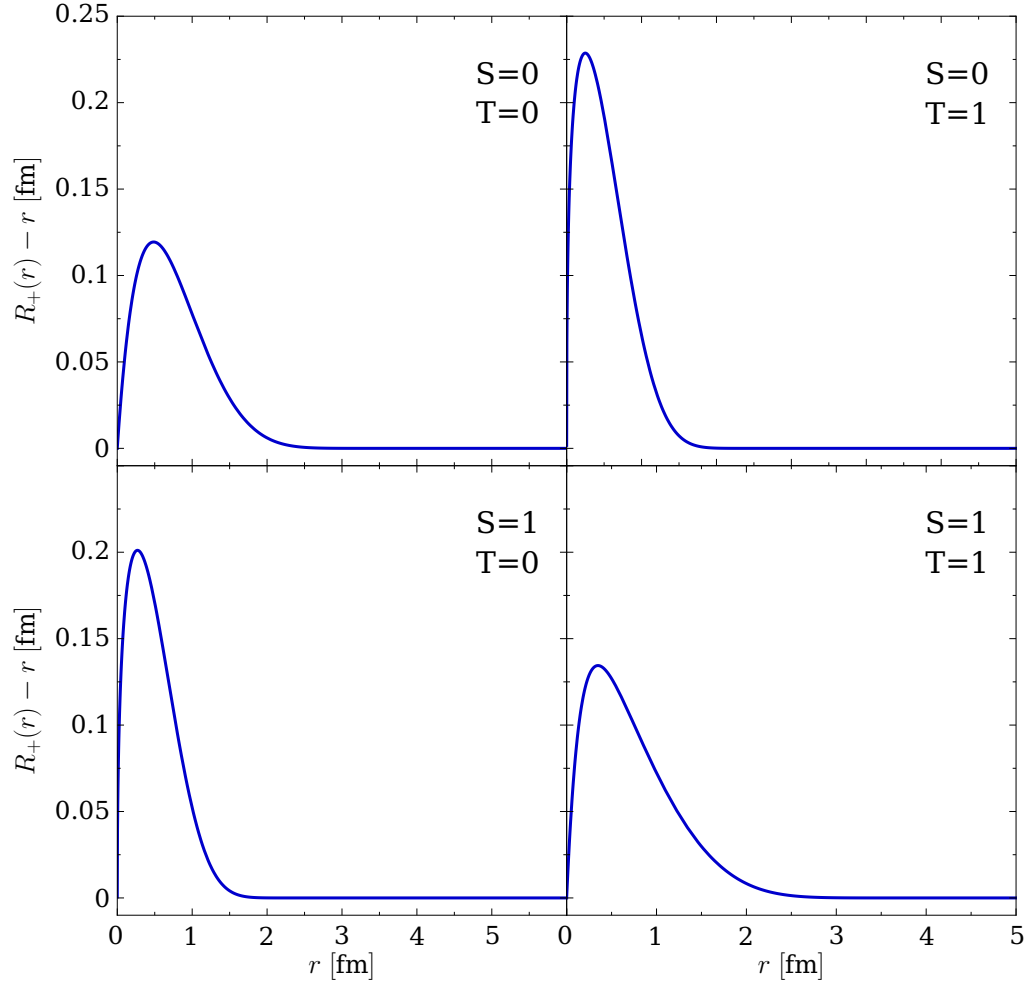


Figure 3.7: UCOM central correlation functions for the AV18 potential for different spin and isospin channels.

differ significantly from the SRG-generated UCOM approach, which might be caused by the SRG transformation which does not distinguish between central and tensor correlations in contrast to the UCOM. As already mentioned in Section 2.3, the scale on which the central correlations are shifted from the potential into the wave-function is given by the core in the UCOM scheme, where there is no scale for the tensor correlations. In the SRG there is no such constraint on the scale and, therefore, central correlations can be taken from the potential to the wave-function on longer length scales. The determination of the UCOM correlation functions via the SRG mapping procedure then leads to correlation functions with longer ranges than in the UCOM scheme using the parameterized correlation functions. This conflicts with the philosophy of the UCOM and is a subject for further studies.

In Table 3.3 three sets of parameters (A1-A3) for the AV18 potential in the different spin-isospin channels are listed. The parameters for the corresponding tensor corre-

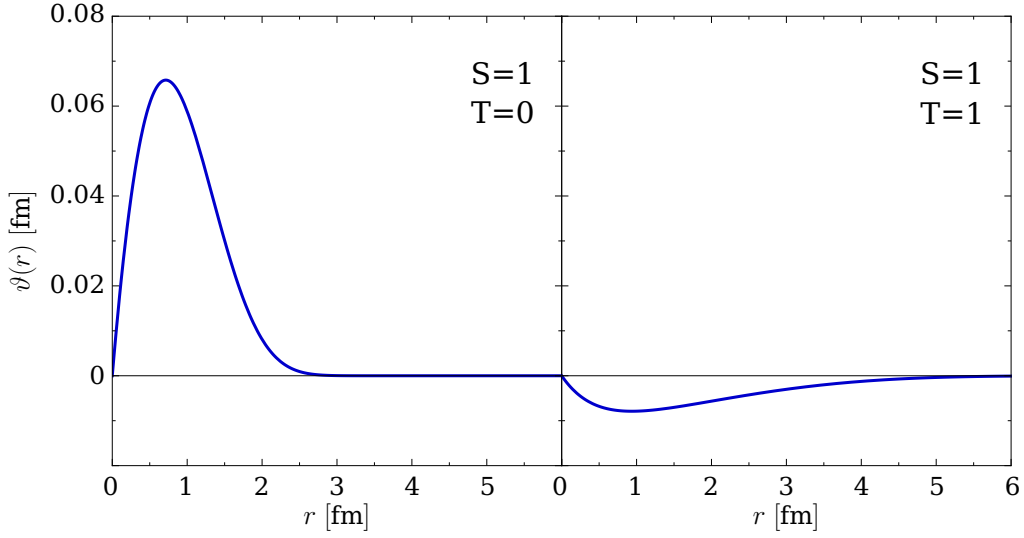


Figure 3.8: UCOM tensor correlation functions for the AV18 potential for different spin and isospin channels.

S	T	I_{R_+} [fm ⁴]	α [fm]	β [fm]	γ [fm]	δ [fm]	set
0	0	0.195	0.9619	1.4436	0.4640	-	A1
0	0	0.1	0.9384	1.1689	0.6126	-	A2
0	0	0.3	0.9660	1.6617	0.3960	-	A3
0	1	0.2	1.2029	1.6600	0.2527	0.8027	A1
0	1	0.111	1.2759	1.4267	0.2885	0.9127	A2
0	1	0.3	1.1475	1.8565	0.2271	0.8027	A3
1	0	0.3	1.1417	1.8348	0.2797	0.7261	A1
1	0	0.1	1.3118	1.0973	0.3442	2.0800	A2
1	0	0.2	1.1244	1.4417	0.2220	2.8097	A3
1	1	0.079	0.7323	1.2806	0.3325	1.8689	A1
1	1	0.2	0.5436	1.8463	0.0960	3.2098	A2
1	1	0.1	0.6891	1.3796	0.2671	2.2717	A3

Table 3.3: Parameters of the central correlation functions $R_+(r)$ in the different spin-isospin channels for the AV18 potential with the cosine parameterization.

lation functions are given in Table 3.4.

For illustration the central correlation functions $R_+(r) - r$ with these parameters are plotted in Figure 3.9. In addition the UCOM correlation functions with parameter set A0 and the SRG-generated UCOM correlation functions are shown. In the $(S, T) = (0, 0)$ channel the variation of the range constraint leads to correlation functions with different strength. Here the correlation functions are somewhat longer ranged than for the SRG-generated UCOM correlation functions. In the $(S, T) = (0, 1)$ channel the correlation functions with the cosine-parameterizations have a very similar range and form of the negative contribution as the SRG-generated UCOM correla-

3.2. OPTIMIZATION OF UCOM CORRELATION FUNCTIONS

S	T	I_ϑ [fm ³]	α	β [fm]	γ [fm]	δ [fm]	set
1	0	0.3	0.7581	2.1796	0.7408	2.4742	A1
1	0	0.2	0.8281	1.8466	0.9052	2.1545	A2
1	0	0.2	0.8081	1.8618	0.8880	2.1670	A3
1	1	-0.02	-0.0885	1.8679	1.1347	2.3001	A1
1	1	-0.2	-0.0634	4.3546	0.4890	4.7080	A2
1	1	-0.09	-0.0840	3.0483	0.7885	3.4544	A3

Table 3.4: Parameters of the tensor correlation functions $\vartheta(r)$ in the different spin-isospin channels for the AV18 potential with the cosine parameterization.

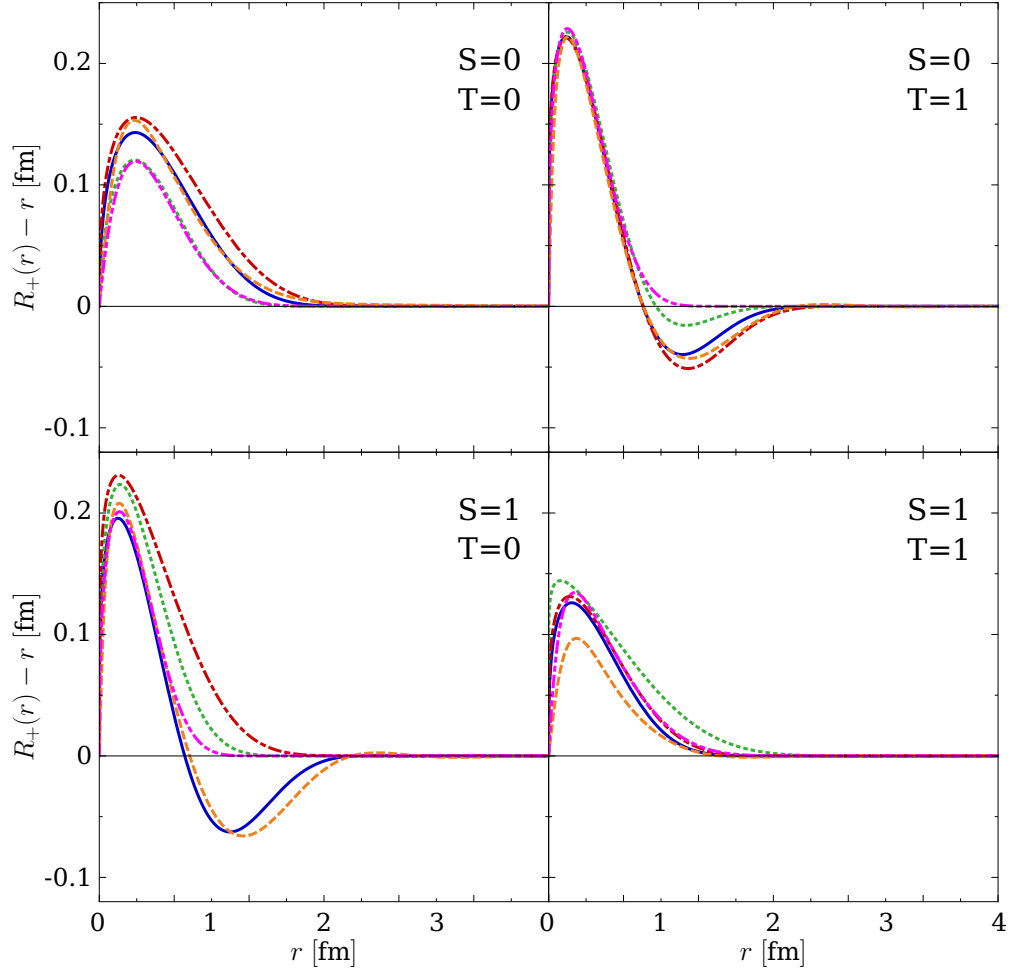


Figure 3.9: UCOM central correlation functions for parameter set A1 (—), parameter set A2 (·····), parameter set A3 (---), SRG-generated UCOM correlation functions (---) and the UCOM correlation functions obtained with parameter set A0 (-.-) for the AV18 potential for different spin and isospin channels.

tion functions. Also in the $(S, T) = (1, 0)$ channel a parameterization is obtained that stays close to the SRG-generated UCOM results. In this channel the SRG-generated

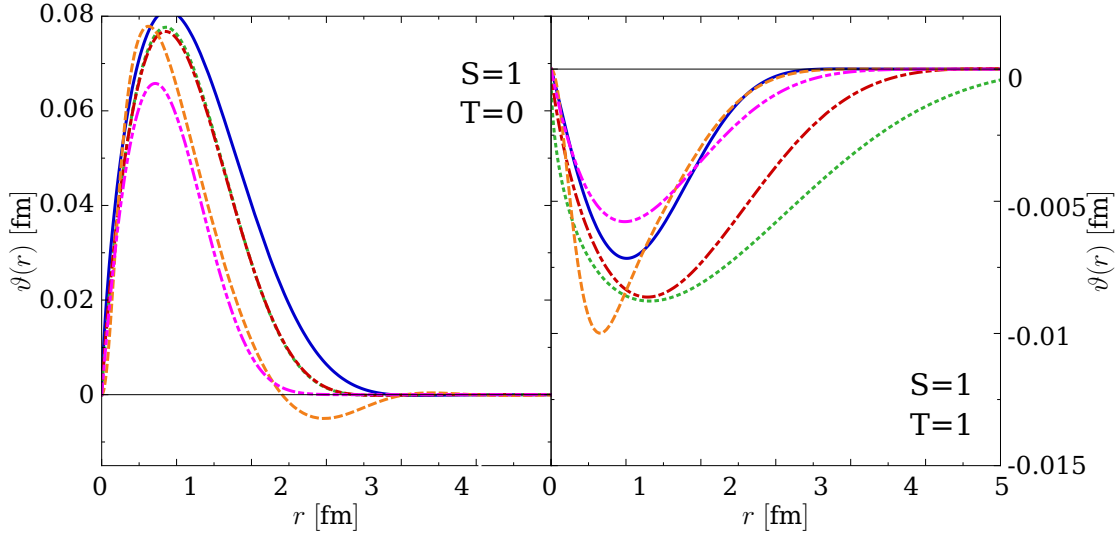


Figure 3.10: UCOM tensor correlation functions for parameter set A1 (—), parameter set A2 (·····), parameter set A3 (-.-.-), SRG-generated UCOM correlation functions (---) and the UCOM correlation functions obtained with parameter set A0 (-.-) for the AV18 potential for different spin and isospin channels. Note the different plot ranges in the two channels.

correlation function has a zero and becomes negative in the attractive intermediate range of the NN interaction, i.e., it pulls nucleons in this region. The range of the negative contribution is a bit longer than for the correlation functions obtained with parameter set A1, where no negative shifts are allowed by construction. For the $(S, T) = (1, 1)$ channel the parameter sets A0-A3 show higher peaks than the SRG-generated UCOM correlation functions. In addition, parameter set A2 has a very steep slope for small radii, which would rather be expected for a hard core potential.

The tensor correlation functions with the parameter sets A0-A3 and the SRG-generated UCOM correlation functions are shown in Figure 3.10. Surprisingly in the $(S, T) = (1, 0)$ channel no parameterization with a negative contribution is found. In both $(1, T)$ channels the obtained parameterized correlation functions differ significantly from the SRG-generated UCOM correlation functions. A parameterization which reproduces the height leads to a much broader curve while one with a similar width produces a much lower amplitude.

For further investigations the correlator set A1 is chosen.

This procedure can be carried out for the N3LO potential as well. The obtained parameter sets N1-N3 are listed in Table 3.5 for the central correlation functions and in Table 3.6 for the tensor correlation functions. For $S = 0$ only one parameter set is given, because it was not possible to find further parameterizations by energy minimization.

The central correlation functions of these parameter sets and of the SRG-generated UCOM ones are shown in Figure 3.11. The parameterizations N1-N3 show completely

3.2. OPTIMIZATION OF UCOM CORRELATION FUNCTIONS

S	T	I_{R+} [fm ⁴]	α [fm]	β [fm]	γ [fm]	δ [fm]	set
0	0	-	1.1130	1.5825	1.4453	-	N1
0	1	-	1.7660	1.8640	0.9290	1.3623	N1
1	0	0.6	2.2566	2.0356	0.8283	1.1924	N1
1	0	0.3	2.2044	1.6875	0.8143	1.4856	N2
1	0	0.2	1.9719	1.5343	0.9333	1.3745	N3
1	1	-0.1	-0.2044	1.6801	4.3185	0.820454	N1
1	1	0.3	0.4798	1.8216	5.5799	2.6907	N2
1	1	0.1	0.1876	1.9422	3.8664	0.4246	N3

Table 3.5: Parameters of the central correlation functions $R_+(r)$ in the different spin-isospin channels for the N3LO potential with the cosine parameterization

S	T	I_ϑ [fm ³]	α	β [fm]	γ [fm]	δ [fm]	set
1	0	0.2	0.4968	1.5081	3.9490	13245.1	N1
1	0	0.08	0.3989	1.4288	4.6586	1.9689	N2
1	0	0.2	0.4871	1.5074	4.0128	4470.1	N3
1	1	0.1	0.0510	3.5882	0.9753	0.8464	N1
1	1	0.08	0.0561	3.2216	1.1282	0.8425	N2
1	1	0.2	0.0365	5.0512	0.5996	0.8558	N3

Table 3.6: Parameters of the tensor correlation functions $\vartheta(r)$ in the different spin-isospin channels for the N3LO potential with the cosine parameterization.

different structures as the SRG-generated UCOM correlation functions. The positive effect of this is the lack of the unphysical long-range oscillations that plagued the latter (see Figures 3.3 and 3.4). In all channels the peak of the correlation functions with parameter sets N1-N3 is shifted a little towards larger radii in comparison to the SRG-generated UCOM correlation functions. The tensor correlation functions for parameter sets N1-N3 are displayed in Figure 3.12. They are quite different from the SRG-generated UCOM correlation functions, which are included for comparison. For $T = 0$ the correlation functions for the three parameter sets are completely positive, as for the AV18 potential. In this channel the artifacts of the cutoff in the N3LO potential show in the SRG-generated UCOM correlation functions as a dip in the positive contribution to the correlation function at short ranges, and long-ranged oscillations. Therefore, it is not astonishing that the UCOM correlation functions N1-N3 look completely different, because they cannot reproduce such structures by construction. A problem occurs for $T = 1$, where even a range constraint is not able to restrict the correlation functions N1-N3 to short ranges. This may be explained by the cutoff effects in the N3LO potential, which manifest here and are stronger than the constraint.

For this potential the correlator set N1 is chosen for further calculations, they seem to be the most reasonable set with regard to their range.

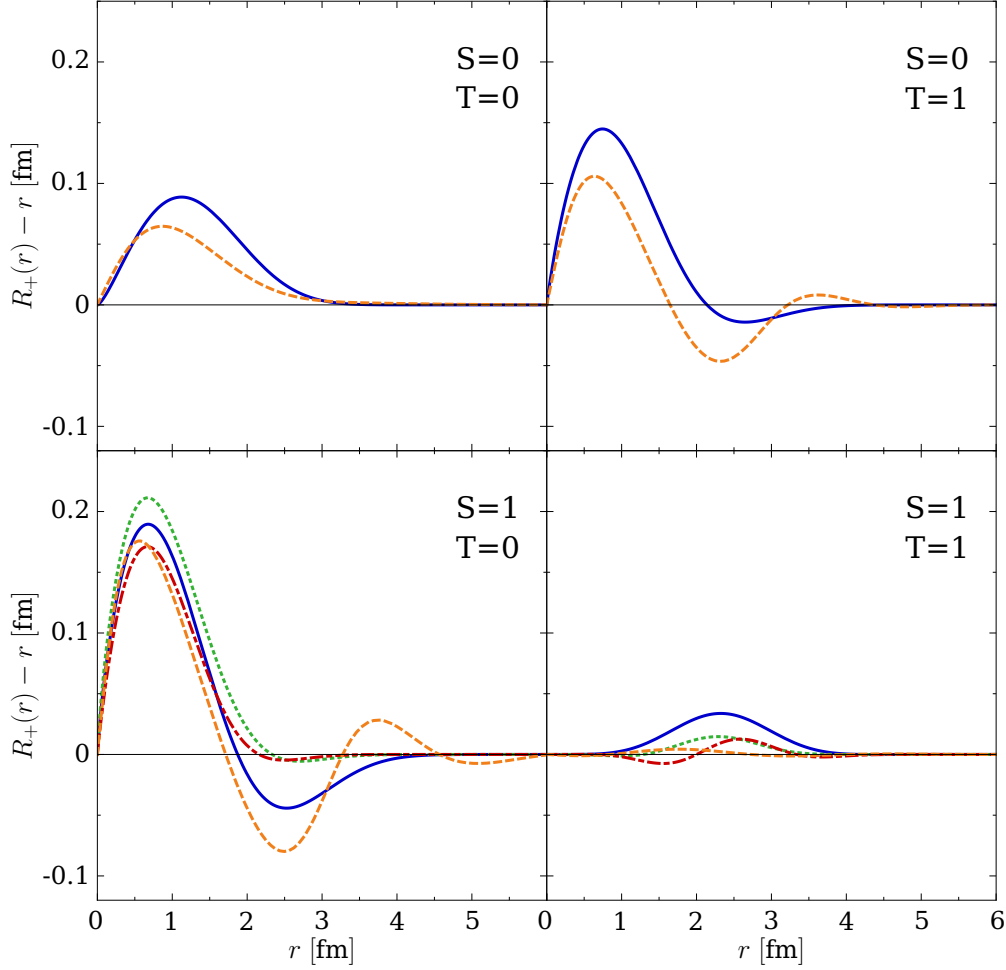


Figure 3.11: UCOM central correlation functions for parameter set N1 (—), parameter set N2 (·····), parameter set N3 (-.-.-) and the SRG-generated UCOM correlation functions (---) for the N3LO potential for different spin and isospin channels.

3.2.3 Few Body Systems with the Different Correlation Functions

The No-Core Shell Model (NCSM) [19, 50, 51] is a powerful many-body method for investigations of light nuclei. It is a quasi-exact method for the solution of the nuclear many-body problem. It is not possible to solve this problem in the complete Hilbert space, therefore a truncation to a smaller subspace is necessary. In order to obtain good convergence to the exact binding energies, large Hilbert spaces have to be used. This leads to a limitation to light nuclei due to computational resources.

Starting with a two-body Hamiltonian in an A -body system

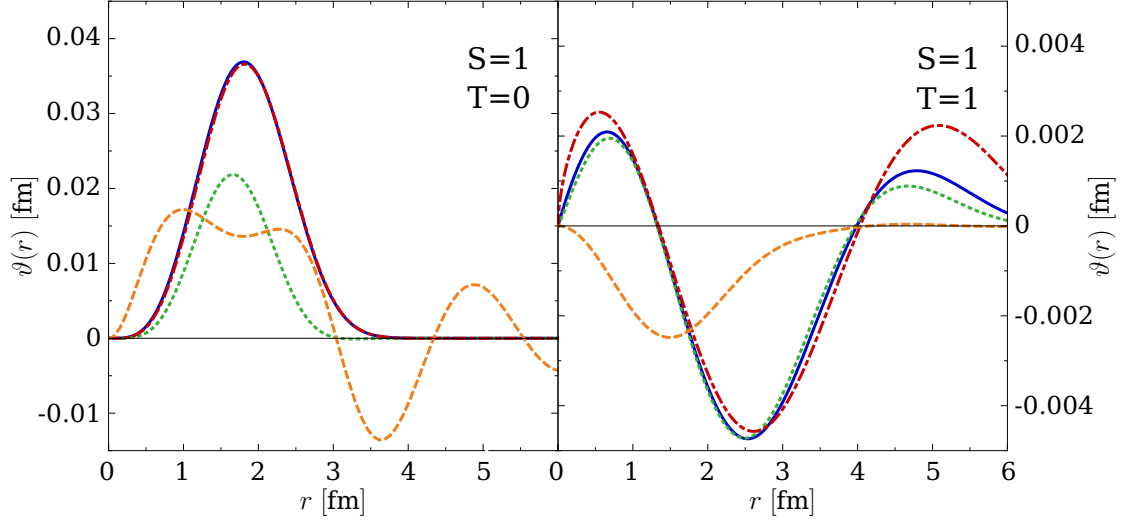


Figure 3.12: UCOM tensor correlation functions for parameter set N1 (—), parameter set N2 (---), parameter set N3 (-.-) and the SRG-generated UCOM correlation functions (---) for the N3LO potential for different spin and isospin channels. Note the different plot ranges in the two channels.

$$H_{\text{int}} = T_{\text{int}} + V = \frac{2}{mA} \sum_{i < j}^A \mathbf{q}_{ij} + \sum_{i < j}^A V_{ij}^{NN} \quad (3.17)$$

with the NN -interaction V^{NN} .

The calculations are performed in harmonic oscillator basis using the basis states

$$|\psi_n\rangle = \sum_i C_{ni} |\phi_i\rangle, \quad (3.18)$$

where the C_{ni} are evolution coefficients and the $|\phi_i\rangle = a_{\alpha 1}^\dagger \cdots a_{\alpha A}^\dagger |0\rangle$ Slater determinants.

The model-space is truncated in this basis to a $N_{\text{max}} \hbar\Omega$ space, where $\hbar\Omega$ is the harmonic oscillator frequency and N_{max} the maximum harmonic oscillator excitation energy. In this basis the eigenvalue problem

$$H_{\text{int}} |\psi_n\rangle = E_n |\psi_n\rangle \quad (3.19)$$

leads to the matrix-elements of the Hamiltonian:

$$H_{ij} = \langle \phi_j | H_{\text{int}} | \phi_i \rangle. \quad (3.20)$$

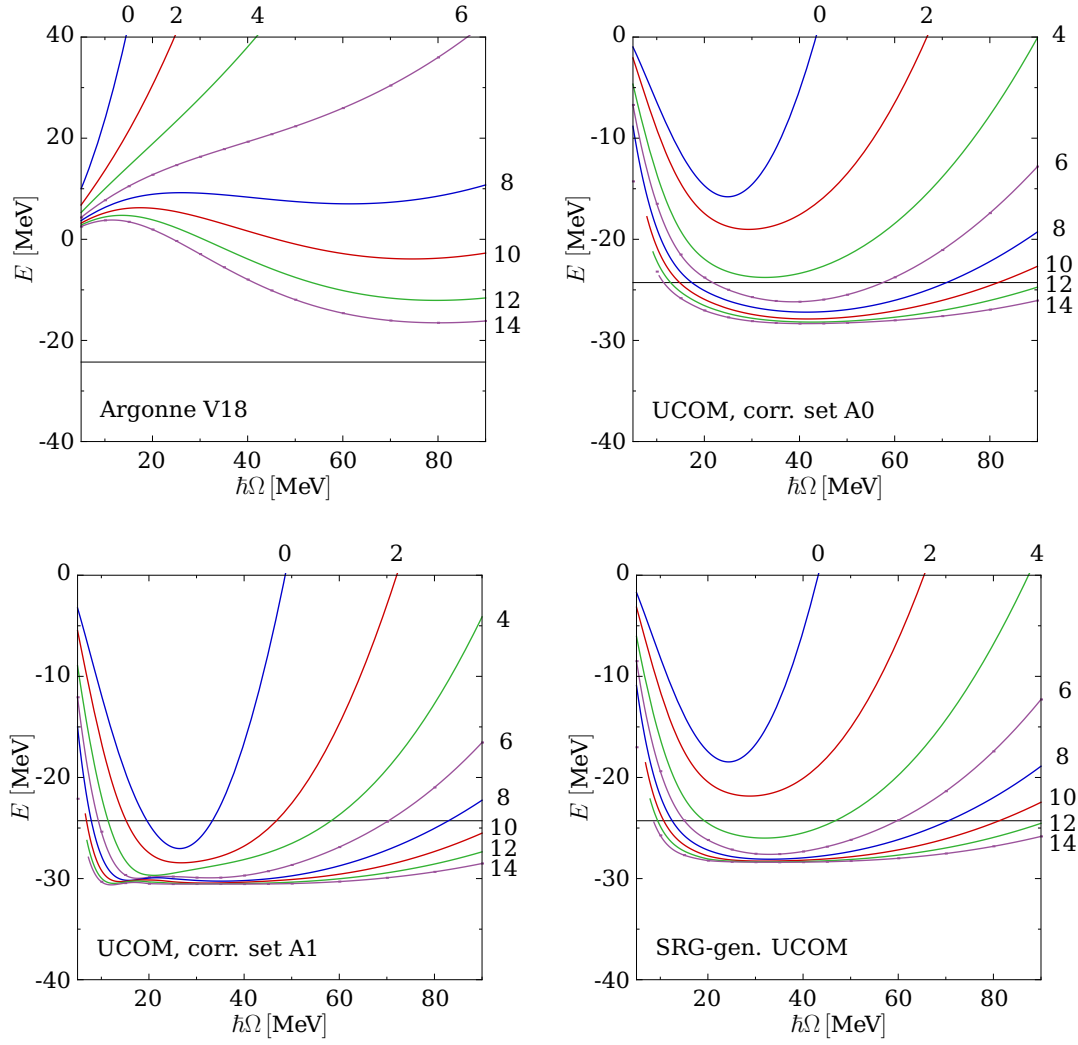


Figure 3.13: Convergence behavior of the NCSM calculations for the ${}^4\text{He}$ ground-state as a function of $\hbar\Omega$ for model-space sizes $N_{\text{max}} = 0 \dots 14$ for the AV18 interaction, UCOM with parameter set A0, UCOM with parameter set A1 and SRG-generated UCOM with $\alpha = 0.04 \text{ fm}^4$. The exact ground-state energy for the potential is denoted by the black line, taken from [52].

The eigenvalues of this matrix are then obtained by diagonalization. Since the description of short-range repulsion needs large model-spaces, effective interactions, as SRG or UCOM transformed interactions, are used to reduce the required model-space size.

In the following the NCSM will be used to study the effects of the central and tensor correlations beyond the deuteron level using effective interactions resulting from SRG and UCOM transformations.

In Figure 3.13 the ground-state energy of ${}^4\text{He}$ as a function of the oscillator parameter $\hbar\Omega$ and the model-space size is shown, obtained from NCSM calculations with the AV18 potential, the V_{UCOM} from parameter set A0 (where the tensor correlator is set to zero

3.2. OPTIMIZATION OF UCOM CORRELATION FUNCTIONS

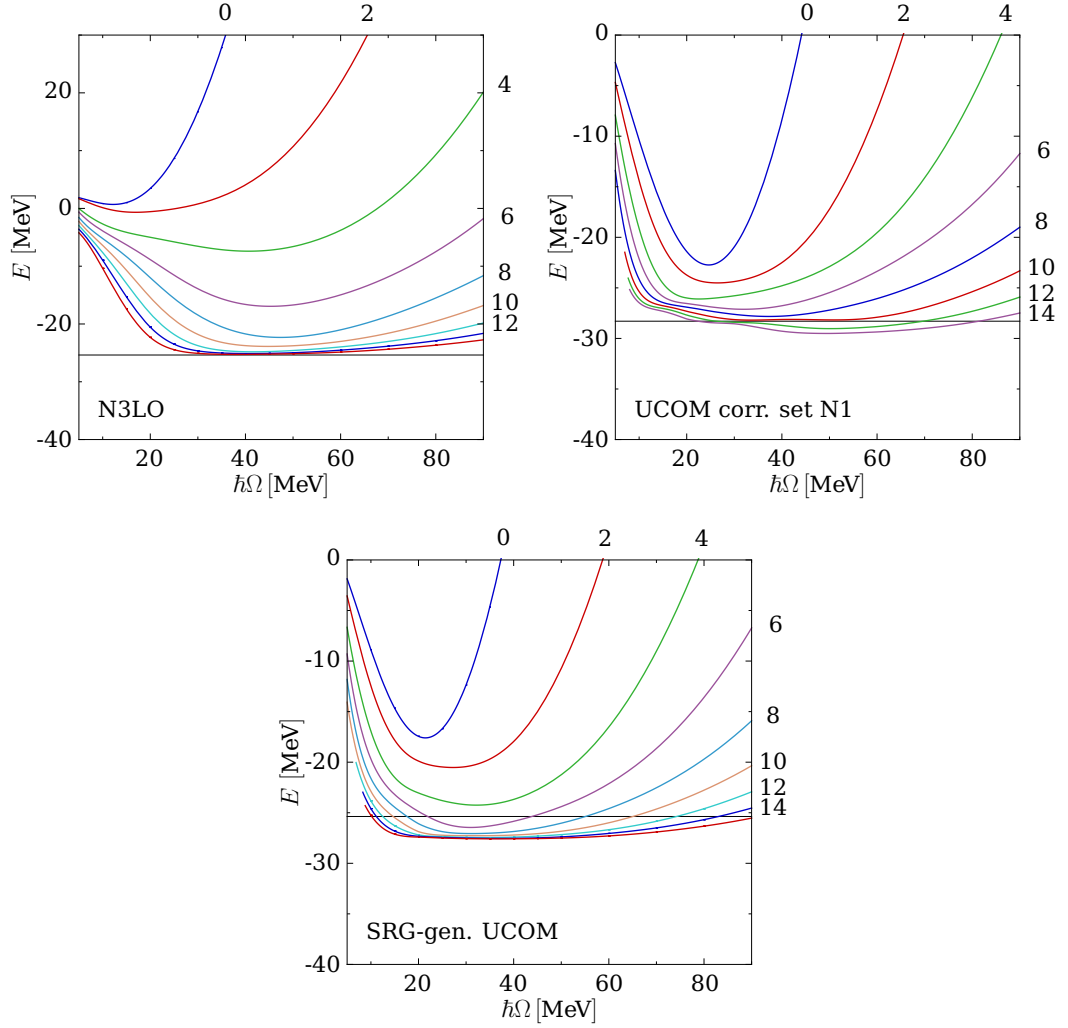


Figure 3.14: Convergence behavior of the NCSM calculations for the ^4He ground-state as a function of $\hbar\Omega$ for model-space sizes $N_{\text{max}} = 0 \dots 14$ for the N3LO interaction, UCOM with parameter set N1 and SRG-generated UCOM with $\alpha = 0.04 \text{ fm}^4$. The exact ground-state energy for the potential is denoted by the black line, taken from [53].

in the $(S, T) = (1, 1)$ channel), A1 and the SRG-generated UCOM correlators. The bare AV18 interaction is not converged even for model-space sizes $N_{\text{max}} = 12 - 14$. This convergence behavior changes when one of the UCOM interactions is used. All of these interactions have bound states even for model-spaces with $N_{\text{max}} = 0$. In this case the model-space consists of one Slater determinant, i.e., no correlations can be described by the state. This implies that the pre-diagonalization of the Hamiltonian in momentum-space reduces the induced short-range correlations in the many-body state. For V_{UCOM} obtained with correlator set A0 convergence is obtained at about $8 - 10 \hbar\Omega$ and for a wide range of oscillator parameters in contrast to the untransformed AV18 interaction. The NCSM calculations with the SRG-generated UCOM interaction

exhibit a somewhat faster convergence than the V_{UCOM} with correlator set A0 and depend very weakly on $\hbar\Omega$.

For V_{UCOM} with correlator set A1 the convergence is much faster, already starting at about $4 - 6\hbar\Omega$ and for a wider range than with correlator set A0. The two-minima structure for larger model-space sizes is a well known feature of NCSM calculations for ^3H with the V_{UCOM} with correlator set A0 [18]. This second minimum in the region of about $10\hbar\Omega$ can be explained by the resolution of structures, i.e., the oscillations of in the wave-functions, of the interaction for large model-space sizes. The converged energy is below the exact ground-state energy for the AV18 potential, which is obtained with Faddeev-Yakubovsky calculations [52], in all cases. This is caused by the omission of three- and four-body interactions in the cluster expansion. If the full cluster expansion would be performed, the energy eigenvalues of the Hamiltonian would not change because of the unitarity of the transformation.

In general, the correlation operators in Section 2.1 are constructed such that they treat only short-range correlations while the long-range correlations are described by the model-space. This can be observed in the convergence behaviour of the NCSM calculations, where the description of long-ranged correlations improves with increasing model-space size leading to additional binding energy.

The results of NCSM calculations for the pure N3LO interaction, the V_{UCOM} from parameter set N1 and with the SRG-generated UCOM are shown in Figure 3.14. In contrast to the AV18 interaction the N3LO interaction shows convergence, starting at model-space sizes of about $N_{\text{max}} = 10$ in a broad range of $\hbar\Omega$. For the interaction V_{UCOM} with parameter set N1 the minimum of the curve with model-space size $N_{\text{max}} = 0$ lies much lower in comparison to the pure interaction. With increasing N_{max} the curves move closer together, but are not fully converged to one fixed energy. This may be caused by the correlation functions which are very long ranged and therefore handling long-range correlations which should, by construction, be described by the many-body state only. Again, as for the V_{UCOM} interaction with correlator set A1 and the AV18 potential, a two-minima structure occurs. The SRG-generated UCOM correlation functions for this interaction show an improved convergence behavior in comparison to the untransformed interaction starting for model-space sizes of $N_{\text{max}} = 8$ over a broad range of $\hbar\Omega$. As for the calculations with V_{UCOM} interaction with correlator set N1 the curves converge to a lower energy compared to the exact ground-state energy for this potential, which is obtained with Faddeev-Yakubovsky calculations.

3.2.4 Many-Body Systems with the Different Correlation Functions

The NCSM is restricted to light nuclei due to computational requirements, because the dimension of the many-body basis at a given $N_{\text{max}}\hbar\Omega$ increases factorially with the particle number. The Hartree-Fock method [54] provides a possibility to perform approximate many-body calculations for any isotope on the nuclear chart. It uses a single Slater determinant to describe the ground-state, corresponding to the $0\hbar\Omega$ space in the NCSM calculations. This simple concept does obviously not allow for the

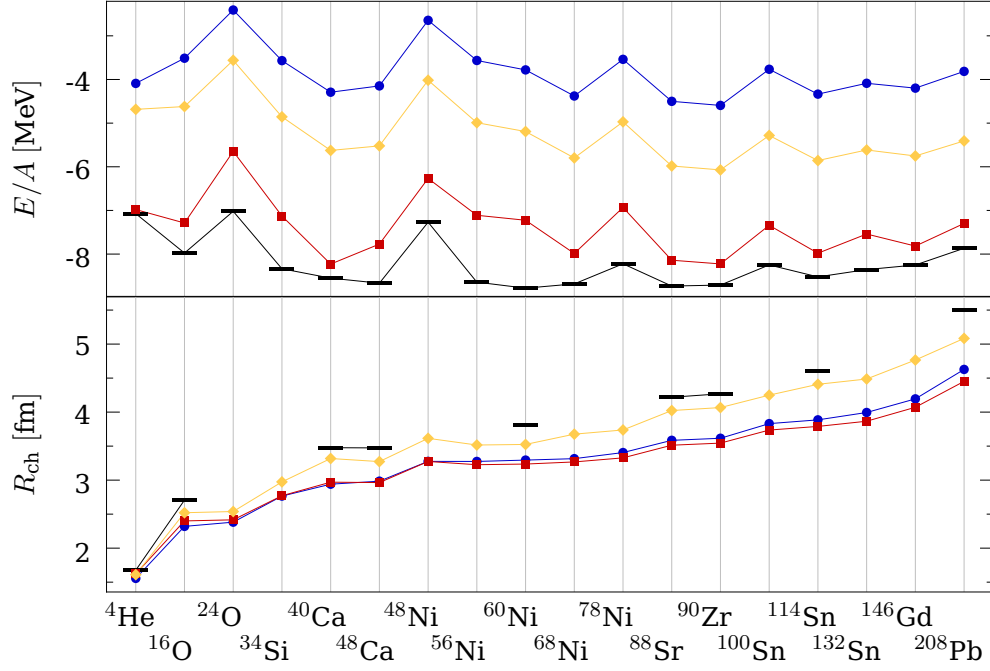


Figure 3.15: Ground-state energies per nucleon (top) and charge radii (bottom) for nuclei with closed j -shell obtained from Hartree-Fock calculations for UCOM with correlator set A0 (●), with correlator set A1 (■) and SRG-generated UCOM (◆). The black bars indicate the experimental values, from [57].

description of correlations, but gives a variational estimate and an upper bound for the exact ground-state energy and can be used for investigations of systematics of the binding energy as a function of mass numbers, for example. To account for the missing correlations other approximations as low-order perturbation theory, Random Phase Approximation or Padè resummation can be applied, see for example [47, 55, 56]. A derivation of the Hartree-Fock equations for a two-body Hamiltonian and application for correlated interactions can be found in Appendix A.

In the Hartree-Fock method the many-body state is represented by a single Slater determinant of single-particle states $|\phi_\nu\rangle$

$$|\Phi_{[\nu]}\rangle = \mathcal{A}(|\phi_{\nu 1}\rangle \otimes |\phi_{\nu 2}\rangle \otimes \cdots \otimes |\phi_{\nu A}\rangle), \quad (3.21)$$

where \mathcal{A} denotes the antisymmetrization operator. The variational solution of the many-body problem with this trial state leads to Hartree-Fock equations, which have to be solved self consistently [38].

The Hamiltonian used for the Hartree-Fock calculations consists of the intrinsic kinetic energy $T_{\text{int}} = T - T_{\text{cm}}$ and the two-body interaction including charge-dependent and Coulomb terms,

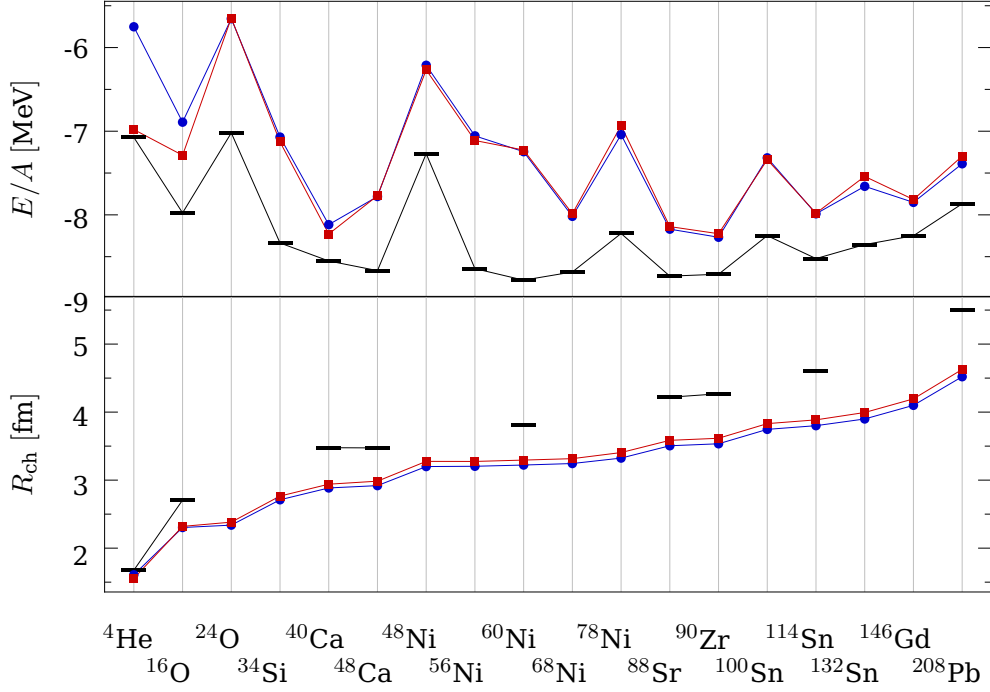


Figure 3.16: Ground-state energies per nucleon (top) and charge radii (bottom) for nuclei with closed j -shell obtained from Hartree-Fock calculations for UCOM with correlator set N1 (●) using the N3LO interaction and correlator set A1 (■) for the AV18 interaction. The black bars indicate the experimental values, from [57]

$$H_{\text{int}} = T_{\text{int}} + V_{NN}. \quad (3.22)$$

The Hartree-Fock single-particle states are expanded in spherical harmonic oscillator single-particle states $|nljmm_t\rangle$, with the radial quantum number n , the orbital angular momentum l , the total angular momentum j with projection m and the isospin projection quantum number m_t

$$|\phi_\nu\rangle = |\nu ljmm_t\rangle = \sum_n C_n^{\nu ljmm_t} |nljmm_t\rangle. \quad (3.23)$$

It is assumed that only harmonic oscillator states with the same quantum numbers l and j contribute in the expansion, and the magnetic substates given by m are degenerate due to spherical symmetry. In the following all calculations will be restricted to closed-shell nuclei, where $C_n^{\nu ljmm_t} = C_n^{\nu lj m_t}$.

In this chapter, as well as in the next chapter for the SRG, the Hartree-Fock calculations are performed with untransformed radii. A detailed discussion of unitary transformed radii with the UCOM as well as the SRG method is presented in Chapter 5.

In Figure 3.15 the Hartree-Fock ground-state energies and the charge radii for closed-shell nuclei ranging from ${}^4\text{He}$ up to ${}^{208}\text{Pb}$. For all three UCOM interactions the binding

energy per nucleon follows the structure of the experimental results, but the binding energy per nucleon is too small by an almost A -independent amount, because long-range correlations are not included in the calculation. This can be corrected for by applying many-body perturbation theory [47]. In general the charge radii are too small and they deviate linearly for increasing mass number.

Interactions derived from correlation functions with negative contributions give larger binding energies per nucleon. V_{UCOM} from SRG-generated correlation functions leads to slightly lower energies in comparison to V_{UCOM} with correlator set A0. For V_{UCOM} with correlator set A1 the energies are much closer to the experimental values than for the other two cases. The radii for correlator set A1 are near the results for the SRG-generated case. Correlator set A0 leads to results much closer to the experimental results. In the Hartree-Fock method a single Slater determinant is chosen as the reference state which means that no correlations can be described by the state. The results compare to the $N_{\text{max}} = 0\hbar\Omega$ model-space of the NCSM. The improvement of the binding energies with correlator set A1 are caused by induced many-body contributions.

For the N3LO potential only Hartree-Fock calculations of V_{UCOM} with correlator set N1 lead to bound states. The binding energy and the charge radii are displayed in Figure 3.16. They are very similar to the Hartree-Fock results for V_{UCOM} obtained with correlator set A1 for the AV18 interaction, which are shown in this figure in addition. The binding energy mimics the structure of the experimental results, but with higher values and the charge radii are smaller than the experiment and the difference increases for heavier nuclei.

The discussion in this section has shown that the new parameterizations for the UCOM correlation functions lead to good convergence in NCSM calculations, showing an oscillating structure, and reasonable Hartree-Fock wave-functions, which are the starting point for more sophisticated methods like Many-Body Perturbation Theory [20, 56] or Coupled Cluster theory [58], as well as RPA calculations for collective modes [47, 21]. In the case of the AV18 potential the correlation functions show structures which are in good agreement with the idea of the UCOM, but unfortunately the correlation functions for the N3LO potential are very long-ranged. This implies that they describe not only the short-range correlations as requested in the construction of the UCOM, but also long-range correlations. In addition the range constraint of the tensor correlation functions, used to control the contribution of induced three-body interactions [38], is not applicable in the case of the N3LO potential. Therefore, it is not possible to control their effect in subsequent calculations. In the philosophy of the UCOM scheme the parameterizations are a possible choice for the AV18 interactions, but not for the N3LO interaction, because it produces long ranged correlation functions, which are caused by the oscillations in the wave-function. In general both, correlator set A1 and N1, contain strong induced many-body forces, which will lead to problems when including three-body forces in the interaction.

Chapter 4

SRG with Alternative Generators

4.1 Λ -SRG

In Section 2.2 the generator of the SRG transformation is defined as the commutator of the relative kinetic energy and the SRG-evolved Hamiltonian. This is a commonly used choice that works quite well. Other choices of generators are suggested in the field of condensed matter theory [59] and nuclear structure physics [42]. Most of these methods use a commutator of diagonal parts of the Hamiltonian and the Hamiltonian itself. A detailed discussion on other generators commuting a function of the kinetic energy with the Hamiltonian is given in [60].

In practice the generator can be adapted to the respective problem [15, 16]. Wegners original choice, using the commutator of the diagonal part of the Hamiltonian with the Hamiltonian itself, is used for example for in-medium SRG calculations [61, 62]. It was shown [63] that this choice of the generator leads to a better decoupling of scales and flow towards diagonal when using initial interactions from EFTs with large cutoffs, than the generator containing the relative kinetic energy.

During the SRG evolution the diagonalization of the momentum-space matrix-elements is driven forward, leading to a decoupling of scales. But during the evolution, induced many-body contributions are obtained, which are neglected for many-body calculations since we consider only one- and two-body terms. For these calculations the transformations leads to simpler states which improve the convergence, where the simpler the state is, the better is the convergence. But this also leads to increasing contributions of the many-body effects and therefore the neglected contributions become larger. The idea is now to search for a generator which leads to good convergence in many-body calculations and generates only small induced many-body contributions. In the following some choices for the generator are tested how they fit in this scheme.

4.1.1 Basic Idea

As already discussed in Section 2.2 the SRG evolution of an Hamiltonian with the generator (2.46) leads to a band-diagonalization of the momentum-space matrix-elements. As shown in in Figure 2.4 two major effects can be observed: a suppression of the off-diagonal matrix-elements and, for $L = 0$ partial-waves, an increase of the attraction of the low-momentum matrix-elements. The first effect, the suppression of the off-diagonal matrix-elements for large $q - q'$ signals the diminution of the short-range correlations. In the deuteron solution of the interaction it is responsible for the elimination of the short-range correlation hole and the reduction of the $L = 2$ admixture [46]. The enhancement of the low-momentum attraction on the other hand means that longer-ranged parts of the tensor interaction are generated during the evolution [38].

As for the UCOM one is interested in the effect of the short-range correlations, while the long ranged part should be described by the many-body state. Therefore, the SRG generator (2.46) has to be adapted to band-diagonalize the momentum-space matrix but leave the low-momentum attractive region unchanged as much as possible, and thereby minimize the contribution of longer-ranged tensor interactions during the evolution. To achieve this behavior an additional parameter, the momentum scale parameter Λ , is introduced in the generator, leading to

$$\eta_\alpha^\Lambda = 2\mu[f(q), H_\alpha] \quad \text{with} \quad f(q) = \begin{cases} 0; & q \leq \Lambda \\ (q - \Lambda)^2; & q > \Lambda. \end{cases} \quad (4.1)$$

SRG transformations with this generator will be referred to as Λ -SRG in the following. A sketch of the function $f(q)$, and the function q^2 for comparison, is shown in Figure 4.1. For the generator η_α^Λ the transformation of the Hamiltonian for small momenta $q \leq \Lambda$ is suppressed and higher momenta are transformed as with η_α . Note that the generator adapts during the SRG flow and consequently the matrix-elements in the region of $q \leq \Lambda$ are changed as well, but less than for the generator η_α .

For $\Lambda = 0$ the flow-equation is identical to the one with the generator η_α and for large Λ the evolution leads to the unevolved potential, because the original potential has

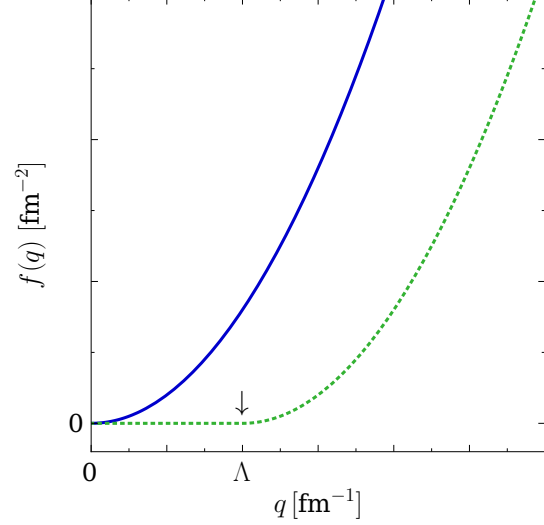


Figure 4.1: Schematic plot of the function q^2 (—) and a partial-wave representation of $f(q)$ appearing in the modified SRG generator η_α^Λ (·····).

contributions up to a certain momentum and decays to zero afterwards.

The SRG flow-equation can be rewritten with generator (4.1), considering just the part for $q > \Lambda$, since the generator is zero otherwise:

$$\frac{dH_\alpha}{d\alpha} = [[(q - \Lambda)^2, H_\alpha], H_\alpha] \quad (4.2)$$

$$\begin{aligned} &= q^2 H_\alpha H_\alpha - 2H_\alpha q^2 H_\alpha + H_\alpha H_\alpha q^2 - 2\Lambda q H_\alpha H_\alpha + 4\Lambda H_\alpha q H_\alpha - 2\Lambda H_\alpha H_\alpha q \\ &= [[q^2, H_\alpha], H_\alpha] - 2\Lambda [[q, H_\alpha], H_\alpha]. \end{aligned} \quad (4.3)$$

We see that the flow-equation with generator η_α is included in the one with generator η_α^Λ , but an extra Λ -dependent term is contained in the latter. Note that this similarity does not imply that the two parts of (4.3) can be evolved separately.

In a partial-wave momentum-space basis the flow-equation for the modified generator can be written as

$$\begin{aligned} \frac{d\mathcal{V}_\alpha^\Lambda(q, q')}{d\alpha} &= -[(q - \Lambda)^2 - (q' - \Lambda)^2]^2 \mathcal{V}_\alpha^\Lambda(q, q') \\ &\quad + 2\mu \int dQ Q^2 [(q - \Lambda)^2 + (q' - \Lambda)^2 - 2(Q - \Lambda)^2] \mathcal{V}_\alpha^\Lambda(q, Q) \mathcal{V}_\alpha^\Lambda(Q, q'), \end{aligned} \quad (4.4)$$

with

$$\mathcal{V}_\alpha^\Lambda(q, q') = V_\alpha^{\Lambda, LL}(q, q') \quad (4.5)$$

for $L = L' = J$ and

$$\mathcal{V}_\alpha^\Lambda(q, q') = \begin{pmatrix} V_\alpha^{\Lambda, LL}(q, q') & V_\alpha^{\Lambda, LL'}(q, q') \\ V_\alpha^{\Lambda, L'L}(q, q') & V_\alpha^{\Lambda, L'L'}(q, q') \end{pmatrix}. \quad (4.6)$$

for the coupled channels, where $V_\alpha^{\Lambda, LL'}(q, q') = \langle q(LS)JT | V_\alpha^\Lambda | q'(L'S)JT \rangle$.

In Figure 4.2 the momentum-space matrix-elements of the Λ -SRG-evolved N3LO potential with the generator η_α^Λ in the flow-equation are shown for two different values of the flow parameter ($\alpha = 0.04 \text{ fm}^4$ and $\alpha = 0.5 \text{ fm}^4$) and three values of Λ ($\Lambda = 0, 1, 2 \text{ fm}^{-1}$). For a fixed value of Λ the matrix is driven towards the diagonal during the evolution. The negative part for small momenta becomes more attractive and the off-diagonal matrix-elements decrease, the diagonal is more pronounced and the matrix-elements for large (q, q') are eliminated. For a fixed value of α and with increasing parameter Λ , the band-diagonalization of the matrix seems to be driven backwards and the repulsive part at low momenta becomes larger. Assuming a fixed value for Λ , the matrix-elements for $q \leq \Lambda$ are affected less for an evolution with the

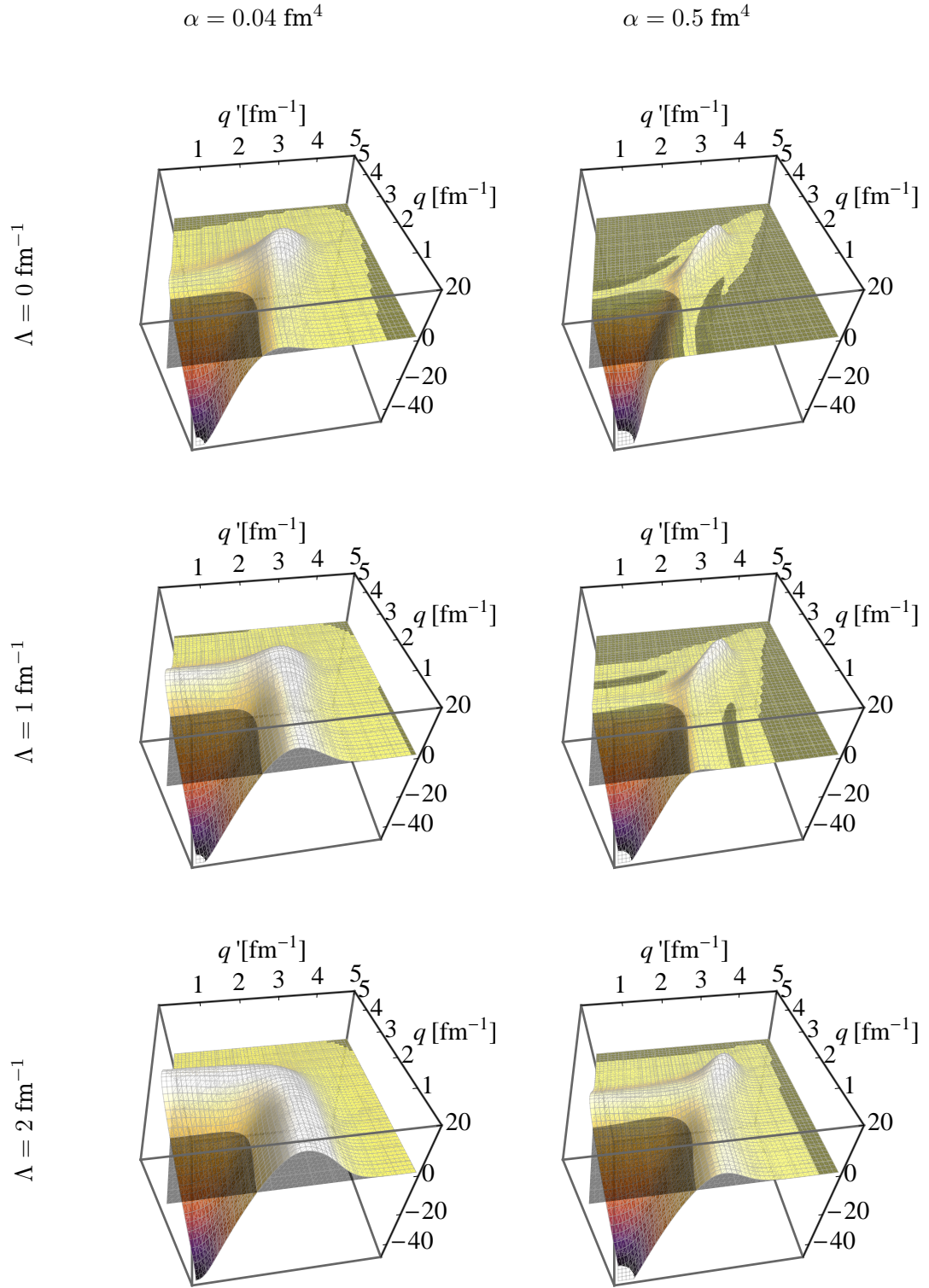


Figure 4.2: Momentum-space matrix-elements in units of MeV fm^3 for the 1S_0 channel of the Λ -SRG-evolved N3LO potential for the flow parameters $\alpha = 0.04 \text{ fm}^4$ and $\alpha = 0.5 \text{ fm}^4$ with $\Lambda = 0, 1, 2 \text{ fm}^{-1}$.

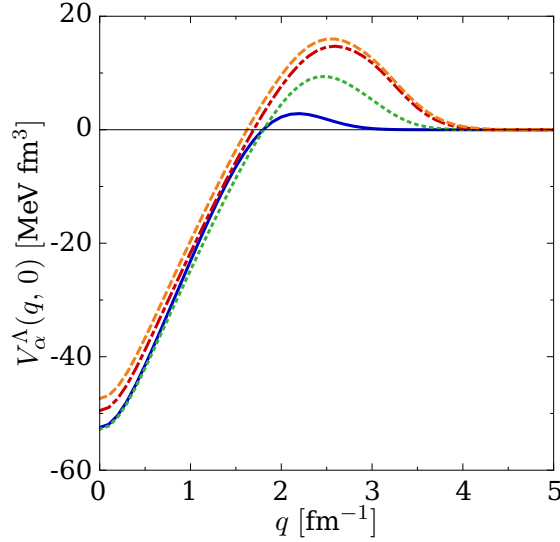


Figure 4.3: Off-diagonal matrix-elements of the evolved N3LO interaction $V_\alpha^\Lambda(q, 0)$ for the flow parameter $\alpha = 0.04 \text{ fm}^4$ with $\Lambda = 0 \text{ fm}^{-1}$ (—), $\Lambda = 1 \text{ fm}^{-1}$ (····) and for $\Lambda = 2 \text{ fm}^{-1}$ (-.-.-). In addition, the unevolved matrix-elements are shown (---).

generator η_α^Λ than for the evolution with the generator η_α . The function in the generator then begins to act with increasing strength leading to a band-diagonalization, but with shifted starting point. Therefore, it is necessary to evolve the potential up to a higher value of α to obtain results which are comparable to the ones for $\Lambda = 0 \text{ fm}^{-1}$.

The off-diagonal matrix-elements $V_\alpha^\Lambda(q, 0)$ for the N3LO potential are shown for fixed $\alpha = 0.04 \text{ fm}^4$ and $\Lambda = 0 \text{ fm}^{-1}$, $\Lambda = 1 \text{ fm}^{-1}$ and $\Lambda = 2 \text{ fm}^{-1}$ in Figure 4.3. For comparison the unevolved matrix-elements are shown as well. Comparing the results for $\Lambda = 0 \text{ fm}^{-1}$ and $\Lambda = 1 \text{ fm}^{-1}$, the matrix-element for $(q, q') = (0, 0)$ is very similar, it decreases just a tiny bit. The width of the repulsive region for these two cases is a bit greater for $\Lambda = 1 \text{ fm}^{-1}$ due to the form of the generator. For $\Lambda = 2 \text{ fm}^{-1}$ the matrix-elements increase and almost coincide with the matrix-elements of the unevolved potential for larger values. As already described in the discussion of Figure 4.2, the positive, repulsive matrix-elements increase for larger values of Λ and are smallest for the evolution with η_α .

4.1.2 Λ -SRG and the Deuteron

The deuteron wave-functions for $\alpha = 0.04 \text{ fm}^4$ and $\Lambda = 0 \text{ fm}^{-1}$, $\Lambda = 1 \text{ fm}^{-1}$ and $\Lambda = 2 \text{ fm}^{-1}$ as well as the deuteron wave-function for the unevolved N3LO potential are shown in Figure 4.4. The D-wave for $\Lambda \neq 0 \text{ fm}^{-1}$ is almost identical to the one of the unevolved potential, as desired by construction. The D-wave of the evolved potential with $\Lambda = 0 \text{ fm}^{-1}$ in contrast is much weaker and the maximum shifted towards larger distances. The correlation hole of the unevolved S-wave vanishes with decreasing Λ . The correlation hole, which is largest for the unevolved wave-function, as expected, is reduced with decreasing scale parameter. For $\Lambda = 0 \text{ fm}^{-1}$ it is completely disappeared

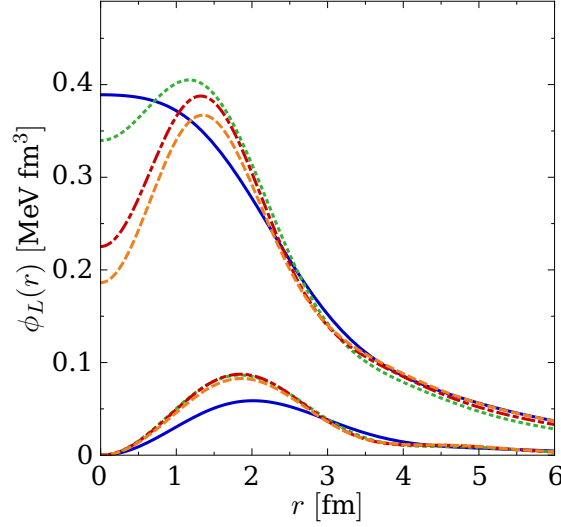


Figure 4.4: Deuteron wave-function $\phi_L(r)$ for the flow parameter $\alpha = 0.04 \text{ fm}^4$ with $\Lambda = 0 \text{ fm}^{-1}$ (—), $\Lambda = 1 \text{ fm}^{-1}$ (---) and for $\Lambda = 2 \text{ fm}^{-1}$ (-.-.-). In addition, the wave-function for the unevolved potential is shown (- - -).

from the wave-function. The difference in the D-wave for the evolved potential with $\Lambda = 0 \text{ fm}^{-1}$ and for $\Lambda > 0 \text{ fm}^{-1}$ shows, that momentum-space matrix-elements in the region $q \leq \Lambda = 1.0 \text{ fm}^{-1}$ have to be responsible for the change in the D-wave. The form of the function $f(q)$ surely plays an important role for this behaviour, as well.

4.1.3 Few- and Many-Body Calculations

NCSM Results for Λ -SRG

For further investigations of the effects the parameter Λ has in the SRG transformation NCSM and Hartree-Fock calculations can be used.

In Fig. 4.5, the convergence of the ^4He ground-state energy in the NCSM with Λ -SRG interactions for a fixed value of the flow parameter $\alpha = 0.04 \text{ fm}^4$ and $\Lambda = 0 \text{ fm}^{-1}$, 1 fm^{-1} , 1.5 fm^{-1} and 3 fm^{-1} is studied. For $\Lambda = 0 \text{ fm}^{-1}$, the energy for optimal $\hbar\Omega$ is practically converged for an $N_{\text{max}} = 6$ model-space, and the $\hbar\Omega$ -dependence is rapidly flattened as the model-space is increased. With increasing Λ , larger model-space sizes are necessary to obtain convergence. For the $N_{\text{max}} = 0$ model-space the two cases for the smaller Λ have very similar results, while for $\Lambda = 1.5 \text{ fm}^{-1}$ the energy becomes higher, i.e., the short-ranged repulsive parts of the interaction are not transformed as strongly, as Λ is increased. For $\Lambda = 1 \text{ fm}^{-1}$ the binding energy increases in comparison to $\Lambda = 0 \text{ fm}^{-1}$, but for the larger value of Λ it becomes slightly smaller again. With the drastic gain of binding energy for $\Lambda \neq 0 \text{ fm}^{-1}$ the minimum of the curves moves towards larger values of $\hbar\Omega$. This implies much smaller rms-radii in this case than for the calculations with $\Lambda = 0 \text{ fm}^{-1}$. Another point to note here is the effect of induced many-nucleon forces, which are stronger for $\Lambda \neq 0 \text{ fm}^{-1}$ and whose strength

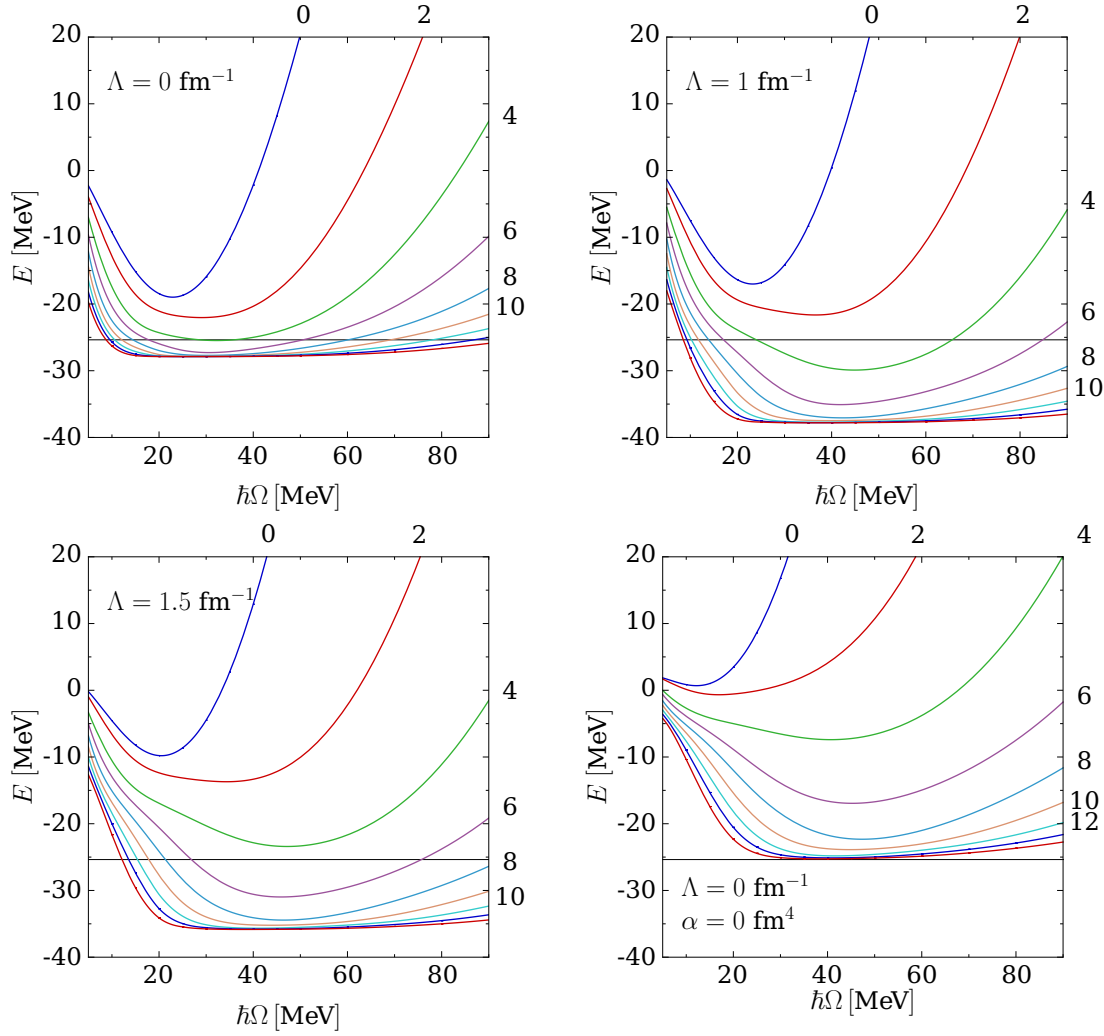


Figure 4.5: Convergence behavior of the NCSM calculations for the ${}^4\text{He}$ ground-state as a function of $\hbar\Omega$ for model-space sizes $N_{\text{max}} = 0 \dots 16$ for the SRG-evolved N3LO interaction with $\alpha = 0.04 \text{ fm}^4$ and $\Lambda = 0 \text{ fm}^{-1}$, $\Lambda = 1 \text{ fm}^{-1}$, $\Lambda = 1.5 \text{ fm}^{-1}$, and the bare interaction, respectively. The exact ground-state energy for the potential is denoted by the black line, taken from [53].

is modified by changing the generator.

In Figure 4.6 the evolution of the converged energy from NCSM calculations as a function of the flow parameter α is shown for $N_{\text{max}} = 16$ and $\hbar\Omega = 50 \text{ MeV}$ in the ${}^4\text{He}$ ground-state for different values of Λ ranging from 0 fm^{-1} up to 3 fm^{-1} . A detailed view of the region for smaller flow parameters up to $\alpha = 0.16 \text{ fm}^4$ is shown in Figure 4.7. For $\Lambda = 0 \text{ fm}^{-1}$ the energy depends on the flow parameter which leads to changes of a few MeV over the whole α -range. Increasing the scale parameter leads to a very strong dependence on the flow parameter. For $\Lambda = 3 \text{ fm}^{-1}$ the results are the same as for the unevolved interaction and show only a weak dependence on the flow parameter.

Comparing the obtained energies for the different scale parameter for $\alpha = 0.1 \text{ fm}^4$ with

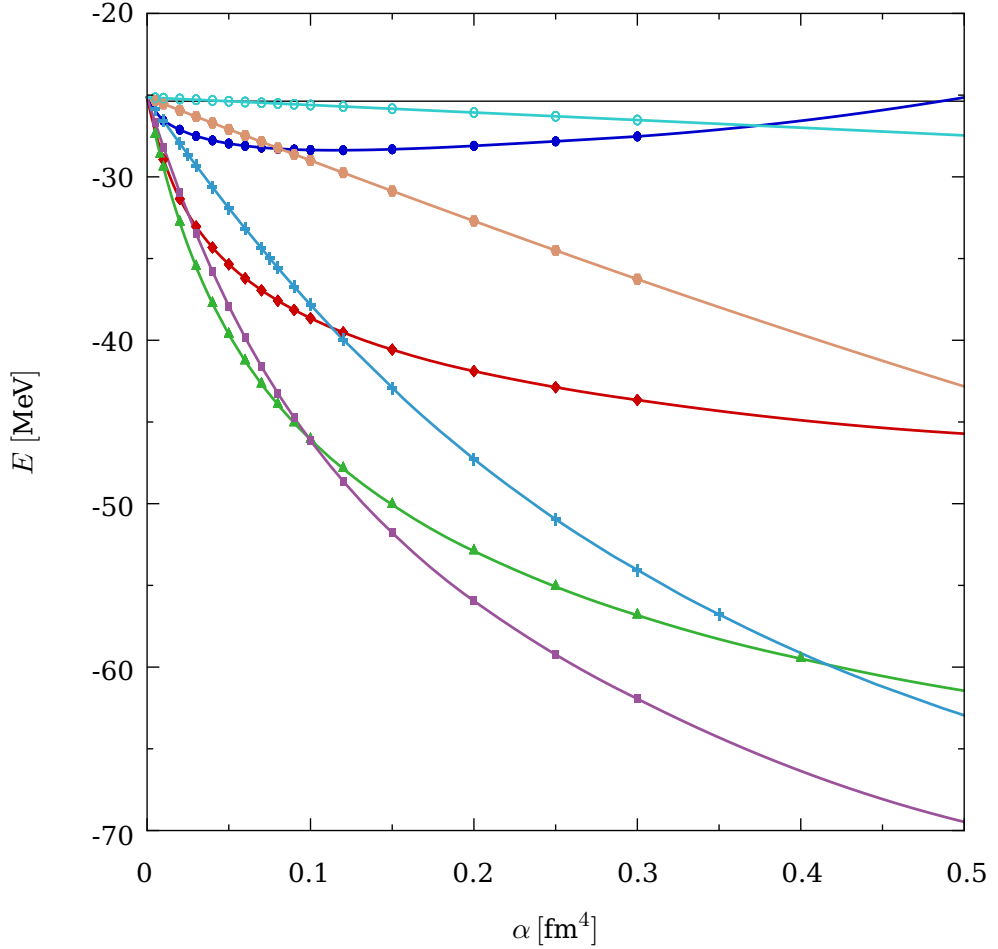


Figure 4.6: Evolution of the energy as a function of the flow parameter α from NCSM calculations with $N_{\max} = 16$ and $\hbar\Omega = 50$ MeV for the ${}^4\text{He}$ ground-state with $\Lambda = 0 \text{ fm}^{-1}$ (\bullet), $\Lambda = 0.5 \text{ fm}^{-1}$ (\blacklozenge), $\Lambda = 1 \text{ fm}^{-1}$ (\blacktriangle), $\Lambda = 1.5 \text{ fm}^{-1}$ (\blacksquare), $\Lambda = 2 \text{ fm}^{-1}$ ($\color{cyan}+$), $\Lambda = 2.5 \text{ fm}^{-1}$ (\circ), and $\Lambda = 3 \text{ fm}^{-1}$ ($\color{cyan}\diamond$).

the energy at $\alpha = 0.0 \text{ fm}^4$, the effect of the Λ -SRG is significant. For the unevolved case ($\alpha = 0.0 \text{ fm}^4$) the energy is identical for all scale parameters. For $\alpha = 0.1 \text{ fm}^4$ the interaction obtained with $\Lambda = 3 \text{ fm}^{-1}$ has the closest value compared to the unevolved energy. For $\Lambda = 1.5 \text{ fm}^{-1}$ and $\Lambda = 2 \text{ fm}^{-1}$ the initial energy is overestimated by about 25 MeV, which means a deviation of 100%. This strong dependence on the flow parameter is caused by the induced three- and four nucleon forces which appear during the evolution. This appearance leads to much lower energies in comparison to the $\Lambda = 0 \text{ fm}^{-1}$ generator.

Hartree-Fock Calculations for Λ -SRG

Next the effect of the Λ -SRG in Hartree-Fock calculations is studied. As already mentioned in Section 3.2.4 in this section only untransformed radii are considered. Fig-

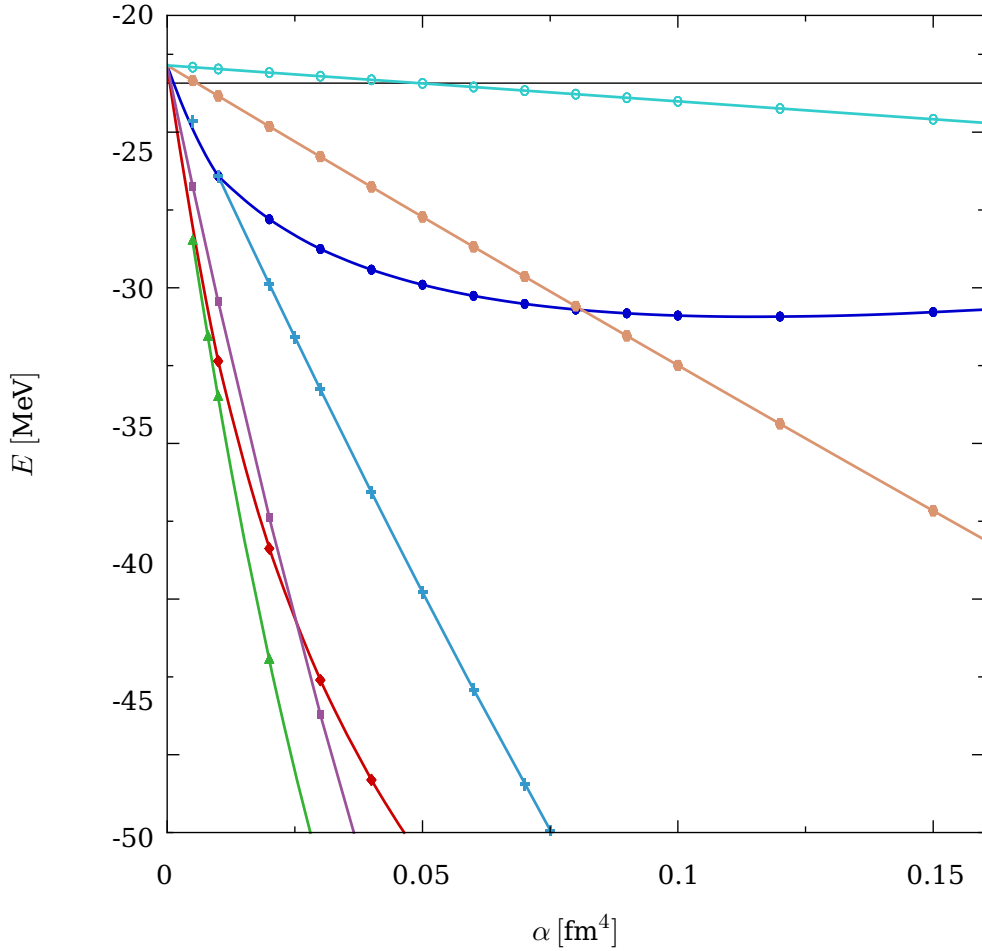


Figure 4.7: Evolution of the energy as a function of the flow parameter α from NCSM calculations with $N_{\max} = 16$ and $\hbar\Omega = 50$ MeV for the ${}^4\text{He}$ ground-state with $\Lambda = 0 \text{ fm}^{-1}$ (\bullet), $\Lambda = 0.5 \text{ fm}^{-1}$ (\blacklozenge), $\Lambda = 1 \text{ fm}^{-1}$ (\blacktriangle), $\Lambda = 1.5 \text{ fm}^{-1}$ (\blacksquare), $\Lambda = 2 \text{ fm}^{-1}$ (+), $\Lambda = 2.5 \text{ fm}^{-1}$ (\circ), and $\Lambda = 3 \text{ fm}^{-1}$ (\diamond).

Figure 4.1.3 summarizes the ground-state binding energies and charge radii for a set of closed-shell nuclei ranging from ${}^4\text{He}$ to ${}^{208}\text{Pb}$ for $\alpha = 0.04 \text{ fm}^4$ and $\Lambda = 0 \dots 3 \text{ fm}^{-1}$. For all values of Λ the binding energy per nucleon mimics the structure of the experimental values, but this curve is tilted to lower energies for heavier nuclei in the case of the smaller Λ . As Λ increases, the curve is shifted upwards until it is parallel to the experimental curve for $\Lambda = 2 \text{ fm}^{-1}$. Further increasing Λ tilts the curve into the other direction, and leads to smaller binding energies per nucleon.

The Hartree-Fock results compare with the $N_{\max} = 0$ model-space in the NCSM. Therefore it is obvious that the changes in the Hartree-Fock energies are much less pronounced for the different scale parameter as in the case of the NCSM for higher N_{\max} , as shown in Figure 4.6 and Figure 4.7. The effect of the induced many-nucleon forces, a lowering of the energies in comparison to the unevolved case, can be observed here as well but not that strong as in the NCSM.

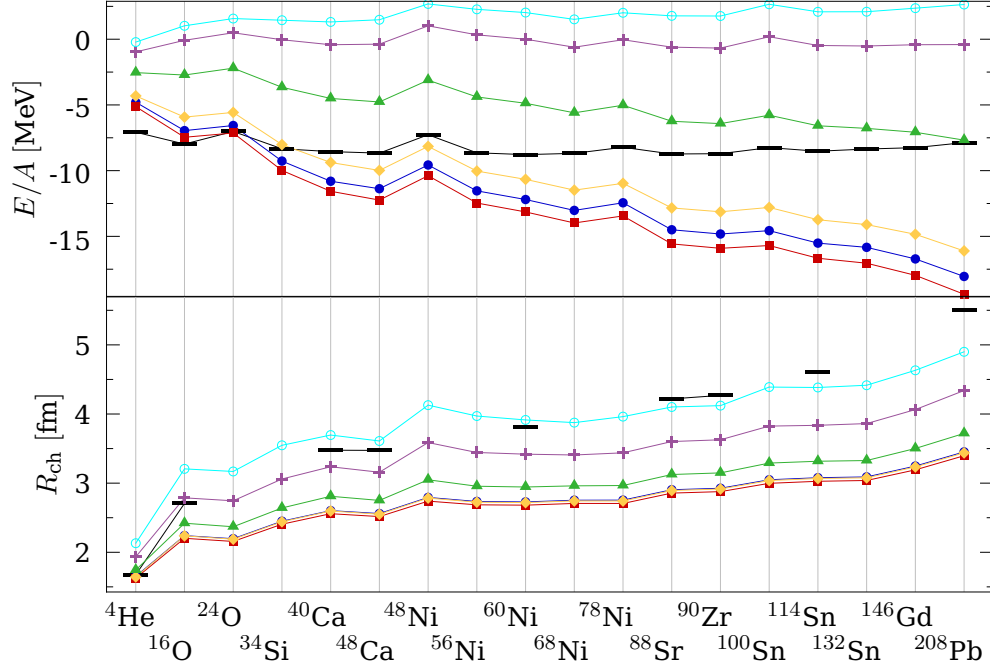


Figure 4.8: Ground-state energies per nucleon (top) and charge radii (bottom) for nuclei with closed j -shell obtained from HF calculations for Λ -SRG with $\Lambda = 0 \text{ fm}^{-1}$ (\bullet), $\Lambda = 0.5 \text{ fm}^{-1}$ (\blacksquare), $\Lambda = 1 \text{ fm}^{-1}$ (\blacklozenge), $\Lambda = 1.5 \text{ fm}^{-1}$ (\blacktriangle), $\Lambda = 2 \text{ fm}^{-1}$ (\blackplus) and $\Lambda = 2.5 \text{ fm}^{-1}$ (\circ) and with the flow parameter $\alpha = 0.04 \text{ fm}^4$ in all cases. The black bars indicate the experimental values.

The charge radii for the three smallest values of Λ are very similar, they mimic the behavior of the experimental values, but they are much lower than the experimental results and the difference to the experimental values increases for higher mass numbers. For higher values of Λ the offset to the experimental results becomes smaller. But the whole curve of the radii is shifted upwards, leading to unbound states for lighter nuclei.

The calculations with the Λ -SRG generator lead to significant changes in the wavefunctions in comparison to the generator used in the previous chapter. Calculations with the NCSM and Hartree-Fock show that induced three- and four-nucleon forces, which are generated during the evolution of the interaction, are very prominent for these generators. These many-body contributions are of a very larger order and hard to handle.

4.2 Generators Containing Different Powers of the Momentum

To decouple long- and short-range properties of an interaction the Hamiltonian is band-diagonalized in momentum-space by means of a SRG transformation. So far this transformation was performed using a SRG generator containing \mathbf{q}^2 . In principle an arbitrary function of $|\mathbf{q}|$ has the same feature. Therefore, such functions can be chosen to investigate how the decoupling can be improved. In [60] a discussion can be found, where an exponential and a geometric function containing the kinetic energy are chosen as generators.

4.2.1 Formulation of the Generators

As a simple alternative to the standard generator with \mathbf{q}^2 , we can allow other powers of $|\mathbf{q}|$ for instance:

$$\eta_{\alpha}^q = \hbar c (2\mu)^2 [\mathbf{q}, H_{\alpha}] \quad \text{and} \quad (4.7)$$

$$\eta_{\alpha}^{q^3} = \frac{1}{\hbar c} [\mathbf{q}^3, H_{\alpha}]. \quad (4.8)$$

Inserting these generators in the general SRG flow-equation (2.39) and transforming it in a partial-wave momentum-space basis, the resulting equations for generators containing q to the power of n are

$$\begin{aligned} \frac{d\mathcal{V}_{\alpha}^n(q, q')}{d\alpha} = & -(2\mu)^{-(n-2)} (\hbar c)^{2-n} \left[q^{(n+2)} + -q'^{(n+2)} - q^2 q'^n - q^n q'^2 \right] \mathcal{V}_{\alpha}^n(q, q') \\ & + (2\mu)^{-(n-3)} (\hbar c)^{2-n} \int dQ Q^2 [q^n + q'^n - 2Q^n] \mathcal{V}_{\alpha}^n(q, Q) \mathcal{V}_{\alpha}^n(Q, q'), \end{aligned} \quad (4.9)$$

with

$$\mathcal{V}_{\alpha}^n(q, q') = V_{\alpha}^{n, LL}(q, q') \quad (4.10)$$

for channels with $L = L' = J$ and

$$\mathcal{V}_{\alpha}^n(q, q') = \begin{pmatrix} V_{\alpha}^{n, LL}(q, q') & V_{\alpha}^{n, LL'}(q, q') \\ V_{\alpha}^{n, L'L}(q, q') & V_{\alpha}^{n, L'L'}(q, q') \end{pmatrix}. \quad (4.11)$$

for the coupled channels, where $V_{\alpha}^{n, LL'}(q, q') = \langle q (LS)JT | V_{\alpha} | q' (L'S)JT \rangle$.

With these generators, the SRG transformation of the N3LO potential is performed for

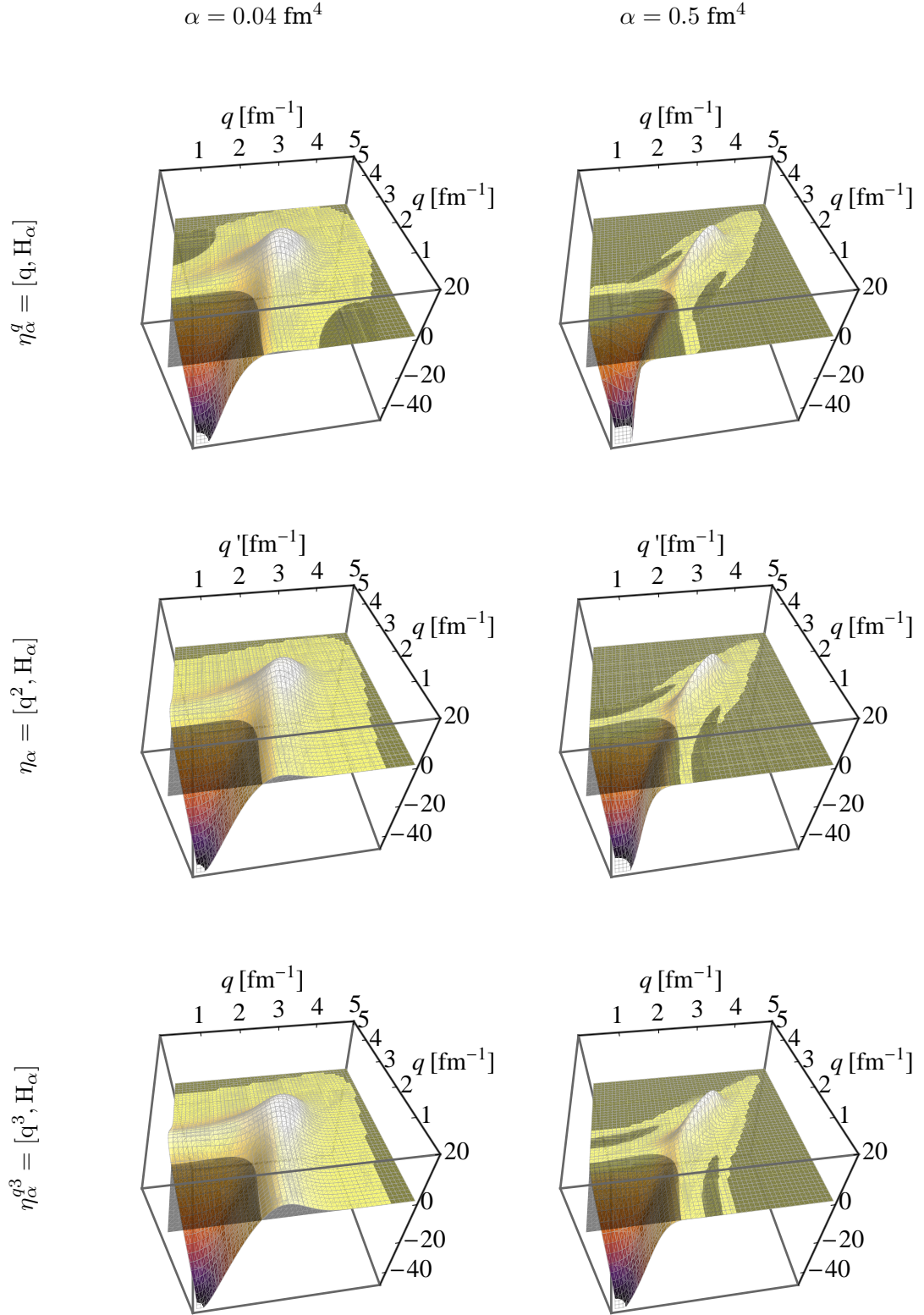


Figure 4.9: Momentum-space matrix-elements in units of MeV fm^3 for the 1S_0 channel of the SRG-evolved N3LO potential for the flow parameters $\alpha = 0.04 \text{ fm}^4$ and $\alpha = 0.5 \text{ fm}^4$ using the generators η_α^q , η_α and $\eta_\alpha^{q^3}$.

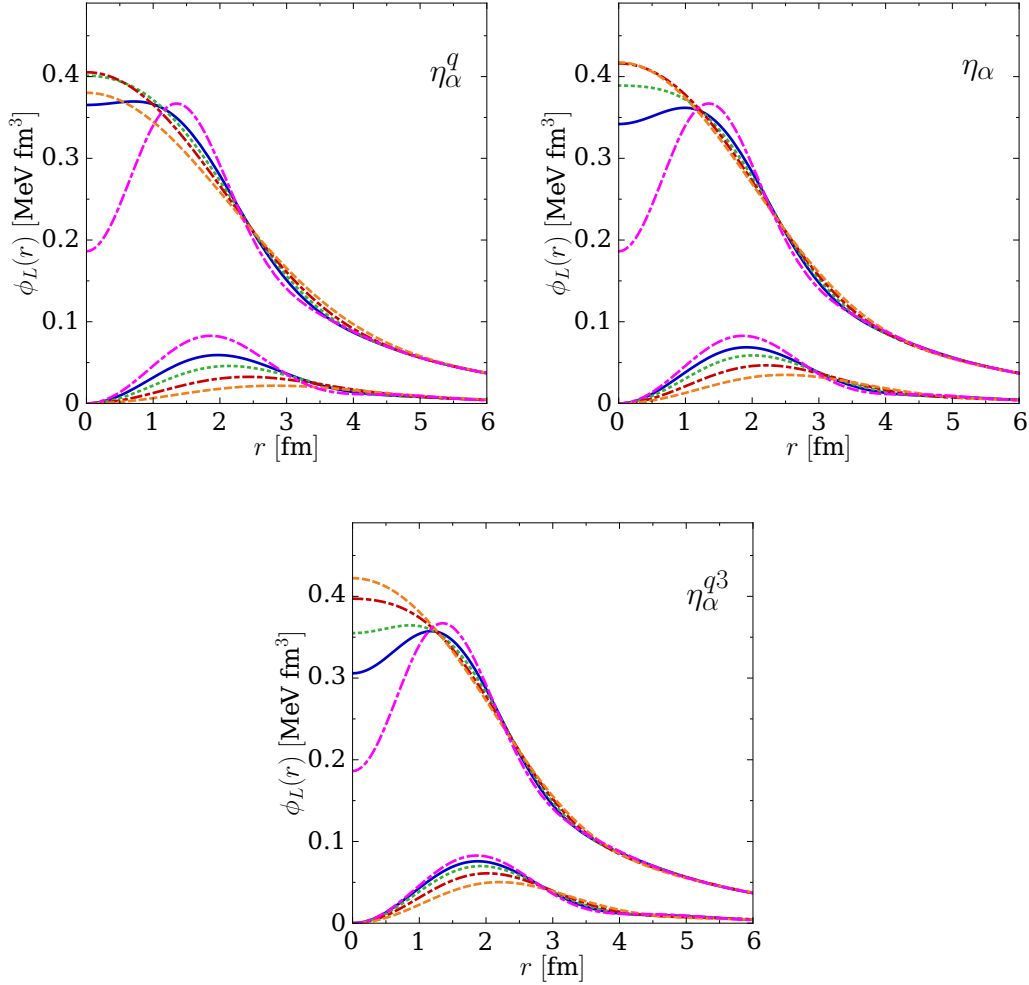


Figure 4.10: Deuteron wave-function $\phi_L(r)$ for the flow parameter $\alpha = 0.02 \text{ fm}^4$ (—), $\alpha = 0.04 \text{ fm}^4$ (·····), for $\alpha = 0.08 \text{ fm}^4$ (-.-.-), $\alpha = 0.16 \text{ fm}^4$ (---) and the unevolved (---) with η_α^q on the left, η_α in the middle and η_α^{q3} on the right.

two different values of the flow parameter, $\alpha = 0.04 \text{ fm}^4$ and $\alpha = 0.5 \text{ fm}^4$, leading to the momentum-space matrix-elements shown in Figure 4.9 for SRG transformations with η_α^q , η_α and η_α^{q3} . All generators lead to a band-diagonalization which is driven forward for increasing flow parameter. For a fixed flow parameter the structure of the matrix-elements is similar for all generators and driven a bit faster to the diagonal for smaller powers of momentum in the generator.

4.2.2 The Transformed Deuteron Wave-Function

Looking at the deuteron wave-functions shown in Figure 4.10 for flow parameters ranging from $\alpha = 0.02 \text{ fm}^4$ up to 0.16 fm^4 and generators η_α^q , η_α and η_α^{q3} , the behavior of the matrix-elements is reflected here. The correlation hole is suppressed in case

4.2. GENERATORS CONTAINING DIFFERENT POWERS OF THE MOMENTUM

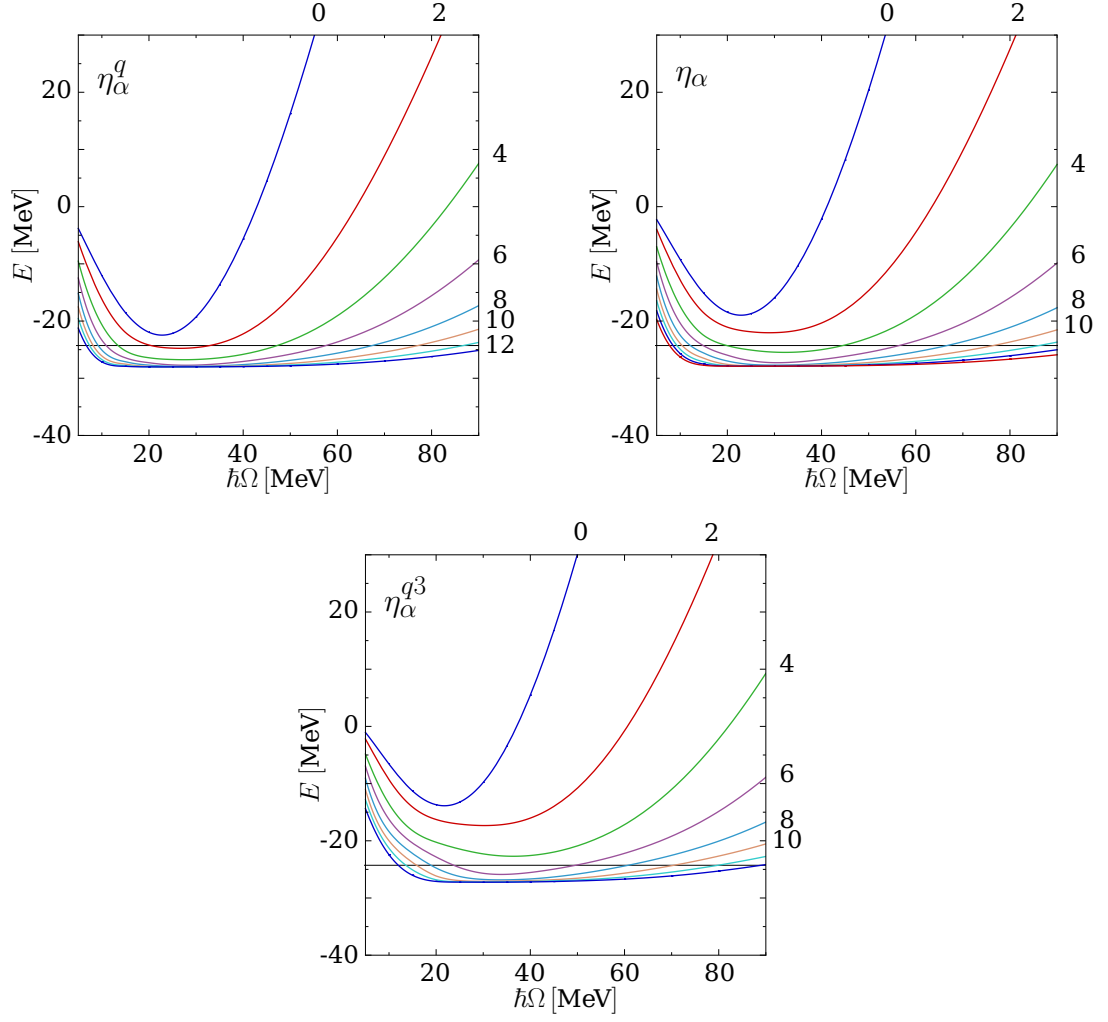


Figure 4.11: Convergence behavior of the NCSM calculations for the ${}^4\text{He}$ ground-state energy as a function of $\hbar\Omega$ for model-space sizes $N_{\max} = 0 \dots 16$ for the SRG-evolved N3LO interaction with $\alpha = 0.04 \text{ fm}^4$ for the generators η_α^q , η_α , and $\eta_\alpha^{q^3}$, respectively. The exact ground-state energy for the potential is denoted by the black line, taken from [53].

of all three considered generators, where the flow parameter necessary to obtain this effect increases slightly for increasing power of momentum in the generator. In case of the generator η_α^q the correlation hole is removed completely for $\alpha = 0.04 \text{ fm}^4$ while the other generators need larger flow parameters. The suppression of the D-wave is achieved the faster the smaller the power of momentum in the generator. For $\eta_\alpha^{q^3}$ the effect on the D-wave is smaller in comparison to the effect of the transformation using η_α^q .

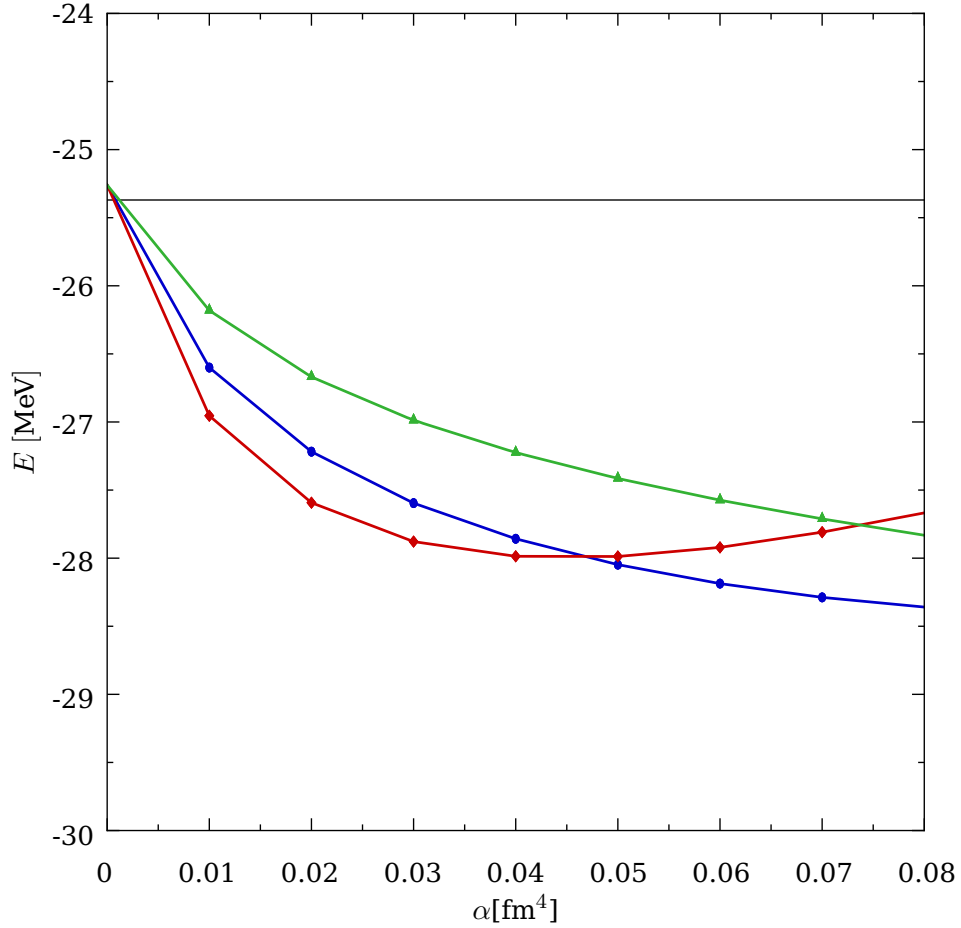


Figure 4.12: Evolution of Energy as a function of the flow parameter α from NCSM calculations with $N_{\max} = 16$ and $\hbar\Omega = 40$ MeV for the ${}^4\text{He}$ ground-state with η_α (\bullet), η_α^q (\blacklozenge) and $\eta_\alpha^{q^3}$ (\blacktriangle). The black line indicates the exact ground-state energy for the potential.

4.2.3 Few-Nucleon System

The NCSM results for the SRG evolved N3LO interaction using the three generators $\eta_\alpha^q = \hbar c(2\mu)^2[q, H_\alpha]$, $\eta_\alpha = (2\mu)^2[q^2, H_\alpha]$, and $\eta_\alpha^{q^3} = (\hbar c)^{-1}[q^3, H_\alpha]$ are shown in Figure 4.11 for a fixed flow parameter $\alpha = 0.04$ fm⁴. All three generators lead to convergence where the resulting energy lies below the exact value. In case of the generator η_α^q the difference between the minimum of the $N_{\max} = 0$ curve and the converged energy is about 5 MeV. For increasing power of momentum in the generator this difference increases up to about 15 MeV for the calculations with $\eta_\alpha^{q^3}$. As already observed for the matrix-elements and the deuteron wave-function, the results converge better the smaller the power of momentum in the generator.

The dependence of the binding energy on the flow parameter for the three different generators is shown in Figure 4.12 for $N_{\max} = 16$ and $\hbar\Omega = 40$ MeV for the ground state

4.2. GENERATORS CONTAINING DIFFERENT POWERS OF THE MOMENTUM

of ${}^4\text{He}$. For all generators the converged energies are below the exact value for the initial interaction. All three generators lead to a similar behaviour of the converged energy. The curves have a minimum which is only shown for η_α^q in this figure. It is shifted towards larger flow parameters for increasing powers of momentum.

The NCSM results for the generators containing different powers of momentum show, that all generators lead to similar results. Since no clear improvement is obtained when using the generators η_α^q and $\eta_\alpha^{q^3}$, the standard generator η_α will be used in the remainder of this thesis.

Chapter 5

Transformed Observables

5.1 Unitary Transformation of Operators

In the previous chapters the UCOM and SRG approaches were used to obtain effective interactions. As already mentioned in Chapter 2, these unitary transformations must be consistently applied to other observables as well. In the following sections, radius and electromagnetic transition operators, are unitarily transformed to investigate their dependence on short-range correlations.

In general, such unitary transformations are performed by application of a unitary operator U to an operator O leading to a transformed operator \tilde{O} :

$$\tilde{O} = U^\dagger O U. \quad (5.1)$$

In the case of the UCOM, the correlation operators $C_r C_\Omega$ introduced in Section 2.1, take the role of the U in this transformation and can be applied directly to the observable under consideration:

$$\tilde{O} = C_\Omega^\dagger C_r^\dagger O C_r C_\Omega. \quad (5.2)$$

In the SRG framework the operator U_α , used in equation (2.40) for the transformation of the Hamiltonian, takes the place of the unitary operator U . To obtain the unitary operator, equation (2.41) is rearranged leading to a flow-equation for U_α :

$$\frac{dU_\alpha}{d\alpha} = -U_\alpha \eta_\alpha. \quad (5.3)$$

In contrast to the UCOM, where the correlation operators are calculated directly for one set of parameters, this equation contains the generator η_α which depends on the Hamiltonian H_α . Therefore, equation (5.3) has to be solved simultaneously with the SRG flow-equation for the Hamiltonian (equation (2.39)) to obtain the unitary operator U_α for a fixed value of the flow parameter α .

In practice the unitary transformation is performed in a two-body harmonic oscillator basis. The matrix-elements of the unitary operator and the observables are evaluated in this basis and the transformation is performed via matrix multiplication. To obtain accurate results the matrix of the observable has a much larger maximum oscillator quantum number, i.e., a larger dimension as the resulting matrix. This value is chosen to be about ten times the oscillator quantum number as for the resulting matrix.

For the description of a transition one assumes an exact spectrum at $\alpha = 0$ with a well known transition operator $O(\alpha = 0)$. The transition from an initial state $|i, \alpha = 0\rangle$ to a final state $|f, \alpha = 0\rangle$ is then given by

$$\langle i, \alpha = 0 | O(\alpha = 0) | f, \alpha = 0 \rangle = \langle i, \alpha = 0 | UU^\dagger O(\alpha = 0) UU^\dagger | f, \alpha = 0 \rangle \quad (5.4)$$

$$= \langle i, \alpha | \tilde{O}(\alpha) | f, \alpha \rangle \quad \forall \alpha. \quad (5.5)$$

Here the transformed operator $\tilde{O}(\alpha)$ and the transformed states $|i/f, \alpha\rangle$ are evolved up to a flow parameter α . This equation has to be fulfilled since the expectation value should be invariant under unitary transformation. For a SRG transformation the initial states include many correlations and other details, depending on the underlying interaction. Throughout the evolution the resolution is lowered to obtain simpler states. But with this simplification of the states the evolved operators may become more complicated, because one- or two-body operators are transformed to A -body operators, where for an exact treatment all of these contributions would have to be considered [64].

Many-body methods like Hartree-Fock or the Random Phase Approximation (RPA) make a simple ansatz for the states. Within the unitary transformation informations from the states are included in the operator and therewith taken from the states. This leads to simpler states which are better suited for many-body calculations than the initial states. In exact methods like NCSM smaller model-space sizes are required to reach convergence, when working with these transformed states. But one has to note that the more the state is simplified, the more complicated becomes the transformed operator, including many-body contributions (2-, 3- or higher body-contributions) which are not negligible in further calculations. Therefore, it is necessary to evolved the state so far that a description with many-body methods is possible, but the many-body contributions in the operator are manageable.

In case of the UCOM the information of equation (5.5) has to be fulfilled as well, i.e., the expectation value should stay unchanged within the UCOM transformation. It is not depending on the SRG flow parameter but on the parameterizations of the correlation functions and their range constraints. This, as well, will lead to simpler states and therefore better input for many-body methods, where a balance between simple states and operators with manageable induced many-body contributions has to be found.

An initial investigation of the transformed radius operator in the UCOM found only small changes in the expectation values compared to the untransformed operator [20].

Likewise, the response functions of UCOM-correlated monopole and quadrupole operators are similar to those of the untransformed operators in the RPA [21]. All these operators are long ranged and thus weakly affected by the short-range correlations [65], because unitary transformations are designed to affect short-range correlations and leave the long-range correlations as unaffected as possible.

For the SRG the transformation of observables is discussed extensively in [25], but only for the deuteron case.

5.2 Radii

The root-mean-square radius of a many-body system is defined by

$$r_{\text{ms}} = \frac{1}{A} \sum_{i=1}^A (\mathbf{x}_i - \mathbf{X}_A)^2, \quad (5.6)$$

where $\mathbf{X}_A = \frac{1}{A} \sum_i \mathbf{x}_i$ denotes the center-of-mass coordinate. The pre-factor $1/A$ is introduced to average over all particles. Rewritten as a two-particle operator and after some algebraic transformations, the mean-square radius for nucleons r_{ms} , protons r_{ms}^p and neutrons r_{ms}^n are given by [66, 46]

$$r_{\text{ms}} = \frac{1}{2A^2} \sum_{ij} r_{ij}^2, \quad (5.7)$$

$$r_{\text{ms}}^p = \frac{1}{AZ} \sum_{ij} r_{ij}^2 \Pi_{ij}^p - \frac{1}{2A^2} \sum_{ij} r_{ij}^2, \quad (5.8)$$

$$r_{\text{ms}}^n = \frac{1}{AN} \sum_{ij} r_{ij}^2 \Pi_{ij}^n - \frac{1}{2A^2} \sum_{ij} r_{ij}^2, \quad (5.9)$$

where i, j run over all nucleons, and Π_{ij}^p and Π_{ij}^n projects on proton and neutron pairs, respectively. Here $\mathbf{r}_{ij} = \mathbf{x}_i - \mathbf{x}_j$ denotes the relative coordinates of a nucleon pair.

The charge radius R_{ch} is then obtained by also including finite-size corrections for protons and neutrons [47]

$$R_{\text{ch}} = \sqrt{r_{p,\text{ms}}^2 + r_{p,\text{ch}}^2 + \frac{N}{Z} r_{n,\text{ch}}^2} \quad (5.10)$$

with the proton charge radius $r_{p,\text{ch}} = 0.87$ fm and the neutron charge radius $r_{n,\text{ch}}^2 = -0.116$ fm² [67].

Like the Hamiltonian, the transformed radius operator is an A -body operator (see Section 2.1.5). As before, the following calculations are restricted to operators containing one- and two-body contributions. Therefore, the two-body approximation of the oper-

ator has to be calculated.

Following [12] the many-body components of a unitary transformation of an operator B in A particle space, leading to the transformed operator \tilde{B} , can be evaluated by decomposing it into irreducible n -body operators via

$$\tilde{B}_A \equiv U^\dagger B_A U = \sum_{n=1}^A \sum_{i_1 < \dots < i_n}^A \tilde{b}_{i_1, \dots, i_n}^{[n]}. \quad (5.11)$$

The irreducible n -body operator $\tilde{b}^{[n]}$ with the n particle indices $i_1 \dots i_n$ is given by

$$\tilde{b}^{[n]} = \tilde{B}_n - \sum_{k=1}^{n-1} \tilde{B}_n^{[k]} \quad (5.12)$$

$$= U_n^\dagger B_n U_n - \sum_{k=1}^{n-1} \sum_{i_1 < \dots < i_k}^n \tilde{b}_{i_1, \dots, i_k}^{[k]}, \quad (5.13)$$

with the unitary operator U_n in n -body space. Applying this expansion to the radius operator leads to the result that the two-body part of the unitarily transformed radius operator is given by the difference of the transformed and the untransformed operator for $A = 2$ particles:

$$\tilde{r}_{\text{ms}}^{[2]} = U^\dagger r_{\text{ms}} U - r_{\text{ms}}. \quad (5.14)$$

Assuming the radius operator $r = 1/(2A) \sum_{ij} r_{ij}^2$, the two-body contribution in two-body space evaluates to

$$\tilde{r}_{\text{ms}}^{[2]} = \left(U_{ij}^\dagger \frac{1}{4} \sum_{ij} r_{ij}^2 U_{ij} - \frac{1}{4} \sum_{ij} r_{ij}^2 \right), \quad (5.15)$$

with the two-body unitary operator U_{ij} .

To obtain the mean-square radius the averaging over the particle number has to be performed, i.e., the equation is multiplied with the factor $1/A$. The pre-factor $1/4$ in equation (5.15) is obtained by evaluating the equation for the radius for $A = 2$ particles.

The transformed rms-radius operator in two-body approximation is then given by

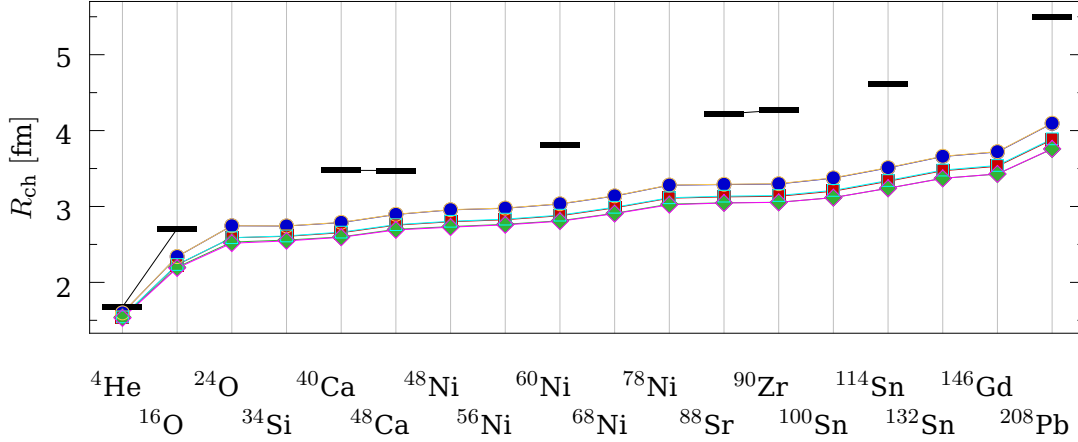


Figure 5.1: Charge radii for nuclei with closed j -shell obtained from Hartree-Fock calculations for the N3LO interaction for $\alpha = 0.04 \text{ fm}^4$ with untransformed (\bullet) and explicitly SRG-transformed (\circ) radii, for $\alpha = 0.08 \text{ fm}^4$ with untransformed (\blacksquare) and transformed (\square) radii and for $\alpha = 0.16 \text{ fm}^4$ with untransformed (\blacklozenge) and transformed (\blacklozenge) radii.

$$\tilde{r}_{\text{ms}} = \tilde{r}_{\text{ms}}^{[1]} + \tilde{r}_{\text{ms}}^{[2]} = r_{\text{ms}} + \tilde{r}_{\text{ms}}^{[2]} \quad (5.16)$$

$$= \frac{1}{2A^2} \sum_{ij} r_{ij}^2 + \frac{1}{4A} \sum_{ij} \left(U^\dagger r_{ij}^2 U - r_{ij}^2 \right), \quad (5.17)$$

where $\tilde{r}_{\text{ms}}^{[1]} = r_{\text{ms}}$ is the bare one-body operator and the unitary transformation in the second term has to be evaluated in two-body space.

5.2.1 Hartree-Fock Calculations with Unitary Transformed Radii

In the previous chapters Hartree-Fock results have been shown for SRG and UCOM transformed interactions, but untransformed charge radii. In the following the effect of unitary transformations on radii will be investigated using the unitary operators obtained from SRG and UCOM calculations, respective.

Figure 5.1 shows SRG-evolved charge radii and the corresponding bare radii for the N3LO interaction for flow parameters from $\alpha = 0.04 \text{ fm}^4$ up to $\alpha = 0.16 \text{ fm}^4$ for a series of nuclei with closed j -shells. Here and in the following bare calculations denote unevolved observables but calculations with states evolved up to the respective flow parameter. All charge radii mimic the trend of the experimental values and for higher mass numbers the difference to the experimental values increases. For $\alpha = 0.04 \text{ fm}^4$ the radii are closest to the experimental values. With increasing flow parameter the difference of the calculated and the experimental measured values increases.

The effect of the transformation is so small that it is not possible to distinguish the

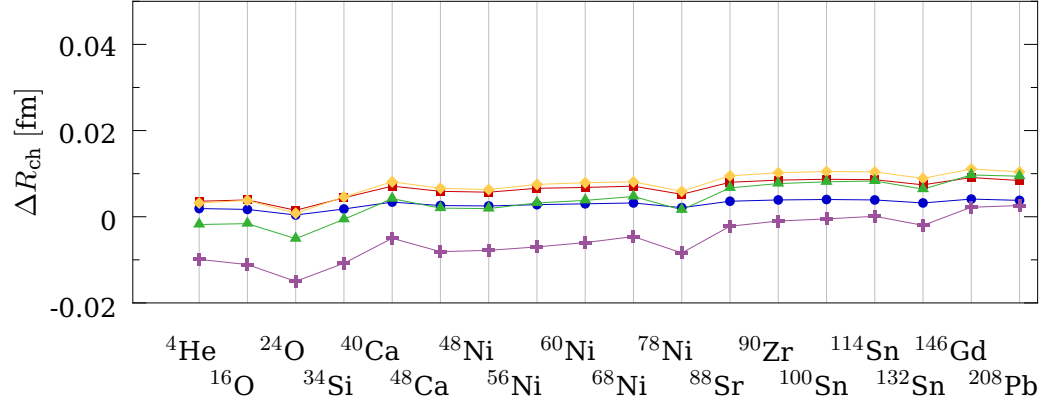


Figure 5.2: Difference of the untransformed and SRG-transformed charge radii with closed j -shell nuclei obtained from Hartree-Fock calculations for the N3LO interaction for $\alpha = 0.04 \text{ fm}^4$ (●), $\alpha = 0.0625 \text{ fm}^4$ (■), $\alpha = 0.08 \text{ fm}^4$ (◆), $\alpha = 0.12 \text{ fm}^4$ (▲) and $\alpha = 0.16 \text{ fm}^4$ (✦). The black bars indicate the experimental values.

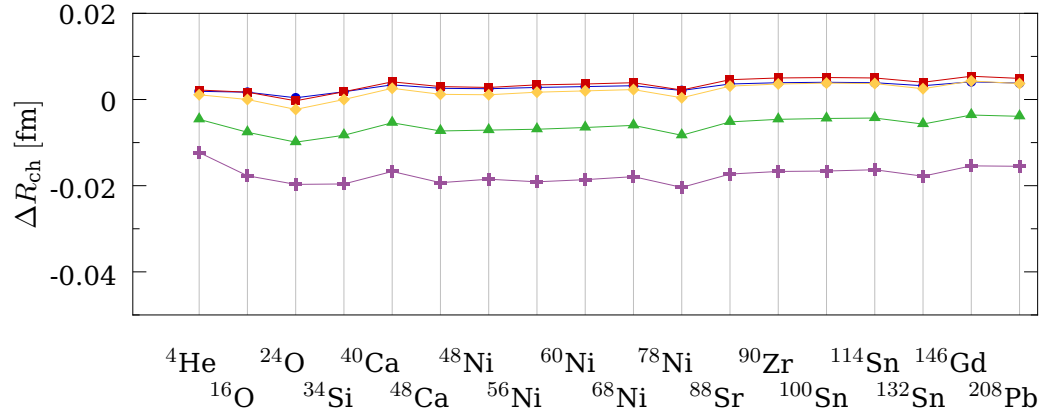


Figure 5.3: Difference of the untransformed and SRG-transformed charge radii with closed j -shell nuclei obtained from Hartree-Fock calculations for the N3LO interaction where the flow parameter is set to $\alpha = 0.04 \text{ fm}^4$ for the interaction and the radii are transformed with $\alpha = 0.04 \text{ fm}^4$ (●), $\alpha = 0.0625 \text{ fm}^4$ (■), $\alpha = 0.08 \text{ fm}^4$ (◆), $\alpha = 0.12 \text{ fm}^4$ (▲) and $\alpha = 0.16 \text{ fm}^4$ (✦).

corresponding transformed and bare curves in Figure 5.1. Therefore, for further investigations the difference between the transformed and the bare radii is calculated, i.e., $\Delta R_{\text{ch}} = [R_{\text{ch}}]^{\text{evolved}} - [R_{\text{ch}}]^{\text{unevolved}}$. Figure 5.2 shows the ΔR_{ch} for the same values of the flow parameter α as Figure 5.1. The effect of the SRG transformation on the charge radii is small compared to the value of the obtained radii. For the three smaller values of α the SRG transformation of the radii leads to slightly larger charge radii. For $\alpha = 0.12 \text{ fm}^4$ the transformed radii are slightly smaller than the bare for light nuclei and become larger for heavier nuclei. In the case of $\alpha = 0.16 \text{ fm}^4$ they are smaller

for light nuclei and the value of the difference decreases for heavier nuclei and the transformed radii are larger than the bare only for nuclei with the highest mass numbers. An interesting effect one observes here is a dependence on the mass number of the nucleus under consideration. For the neutron-rich nuclei ^{24}O , ^{78}Ni and ^{132}Sn the curves show structures which are more pronounced the larger the flow parameter. In general the deviations of the transformed from the bare radii is very small and does not exceed 1%.

Figure 5.3 shows the differences of the bare and transformed charge radii for flow parameters from $\alpha = 0.04 \text{ fm}^4$ up to $\alpha = 0.16 \text{ fm}^4$ computed with Hartree-Fock wavefunctions obtained for an interaction evolved with $\alpha = 0.04 \text{ fm}^4$ in all cases. This evolution scheme will be referred to as inconsistent in the following. A consistent treatment is defined as the evolution of the observable and the interaction with the same α .

For the inconsistent case, there is still some dependency on the nucleus under consideration, but it is less pronounced than in the consistent case. Increasing the flow parameter leads to a parallel shift of the differences towards smaller radii over the whole mass region.

In both figures the differences of the bare and transformed radii for $\alpha = 0.16 \text{ fm}^4$ show the largest effects of the evolution of the operator. For $\alpha = 0.12 \text{ fm}^4$ the results shown in Figure 5.4 start to deviate significantly from the results obtained with smaller flow parameters. To investigate the dependence on α the charge radii obtained from Hartree-Fock calculations with consistent and inconsistent treatment of the bare and evolved radii are shown in Figure 5.4. Here the nuclei ^4He , ^{40}Ca , ^{78}Ni and ^{114}Sn for flow parameters ranging from $\alpha = 0.04 \text{ fm}^4$ up to $\alpha = 0.5 \text{ fm}^4$ are chosen. In case of the inconsistent transformation of the bare radius, the results are shown as a straight line. This is, because the radii are only calculated for this fixed parameter and used as input for calculations of the transformed radii for all considered flow parameters.

In the region of small flow parameters the curves of transformed and bare radii for both, consistent and inconsistent treatment of the interaction, are close to each other. But at a range of about $\alpha = 0.1 \text{ fm}^4$ to $\alpha = 0.16 \text{ fm}^4$ the curves cross and then start to diverge for all nuclei. This shows that the assumption that the transformed and bare radii do not deviate much is applicable for flow parameters up to about $\alpha = 0.15 \text{ fm}^4$, but for larger values the difference increases. Since typically the flow parameters for SRG calculations are chosen to be $\alpha = 0.16 \text{ fm}^4$ and below the effect of explicitly transformed radii is very small. But, as mentioned in Section 5.1, one has to notice here, that Hartree-Fock is a mean-field approach. Therefore the accuracy of the approximations becomes better for higher flow parameters where more correlations are described within the transformed operator. For larger flow parameters the impact of these correlations as well as neglected induced many-body contributions lead to increasing differences of the transformed and bare radii. In the consistently transformed case the radii seem to converge for higher flow parameters, except for the ^4He nucleus. This independence on the flow parameter is desired in general, because it shows that no higher-body contributions are necessary to be included in the transfor-

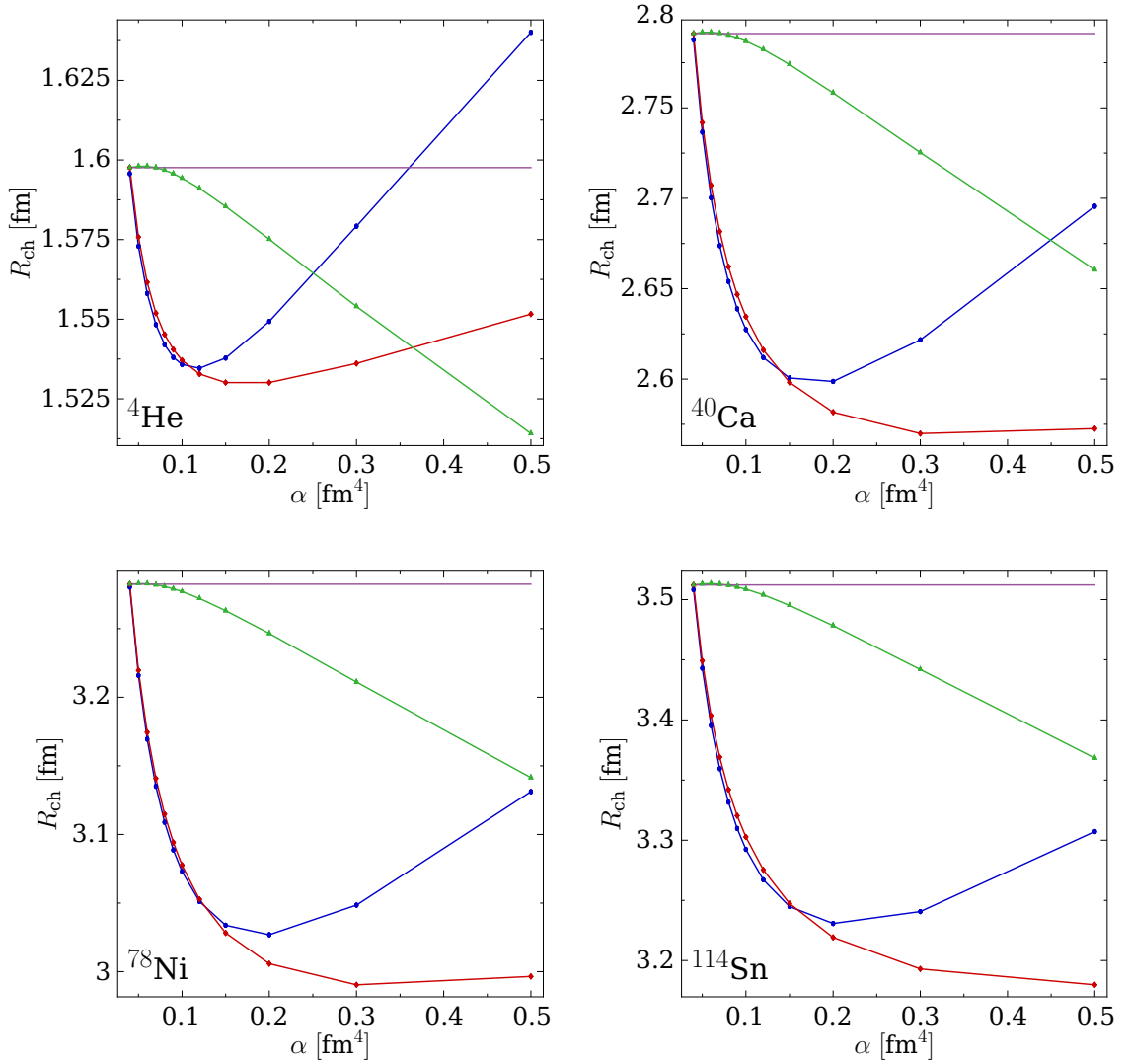


Figure 5.4: Hartree-Fock results for charge radii of the ^4He , ^{40}Ca , ^{78}Ni and ^{114}Sn nuclei in dependence on the flow parameter α for bare (●) and SRG-transformed (◆) radii as well as the results for transformed radii with constant flow parameter for the evaluation of H_α (▲) and the corresponding result for bare radii (—).

mation. Nevertheless, this effect occurs here at very high flow parameters, i.e., in a region where higher many-body effects increase. This leads to the conclusion that the effects observed here are caused by the Hartree-Fock method.

Hartree-Fock results for the bare and UCOM transformed radii for the AV18 interaction using correlator sets A0 and A1 are shown in Figure 5.5 for nuclei with closed j -shells. Both correlator set are introduced in Chapter 3 and differ in their parameterisation, where correlator set A1 includes a cosine-function allowing for negative contributions in the correlation functions. The obtained results are similar to the SRG results, i.e., the effect of a UCOM transformation of the radii does not change the

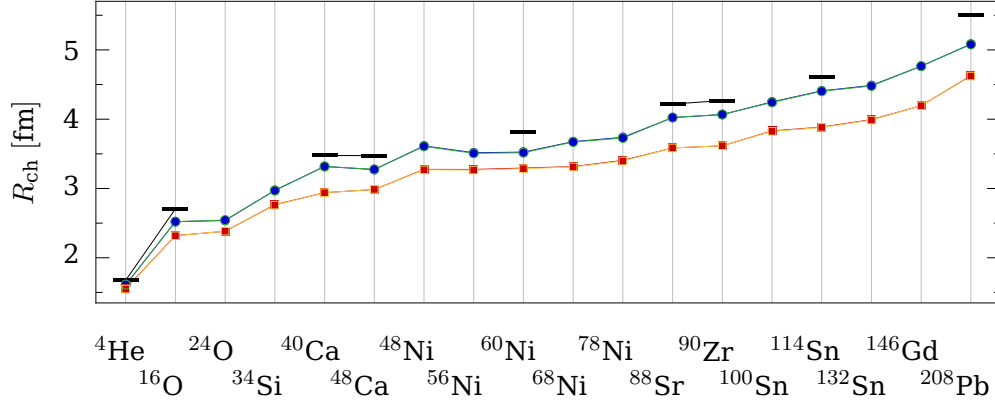


Figure 5.5: Charge radii with closed j -shell nuclei obtained from Hartree-Fock calculations for AV18 with correlator set A0 with the bare radii (●) and the UCOM transformed radii (○) and A1 with bare radii (■) and transformed radii (□).

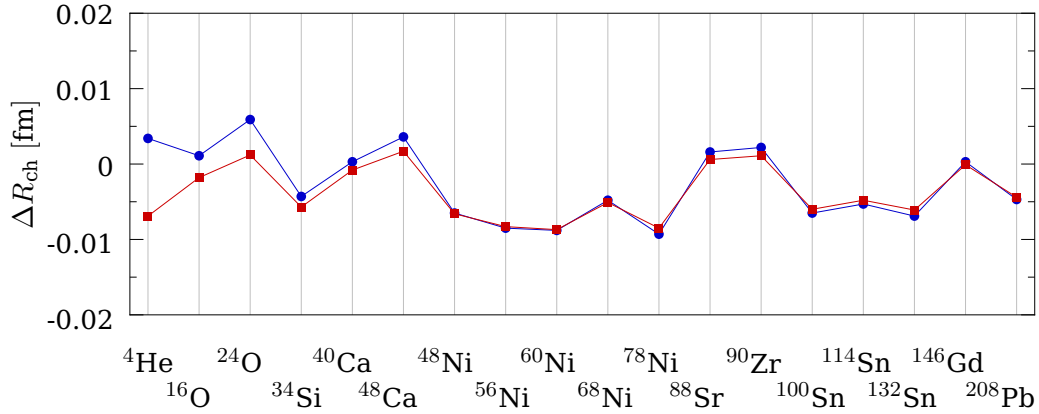


Figure 5.6: Difference of the bare and UCOM transformed charge radii for the AV18 interaction with closed j -shell nuclei obtained from Hartree-Fock calculations for the correlator sets A0 (●) and A1 (■).

Hartree-Fock results significantly. The differences ΔR_{ch} of both curves are shown in Figure 5.6. The effect of the transformation is, similar to the SRG transformation, smaller than 1%.

5.2.2 NCSM Calculations with SRG-Transformed Radii

For further investigations of the effect of the SRG evolution of a radius operator, NCSM calculations are performed using the N3LO interaction. Figure 5.7 shows the unevolved radii (r_{ms}) in dependence of the model-space size N_{max} for the ^4He nucleus using flow parameters ranging from $\alpha = 0.04 \text{ fm}^4$ up to $\alpha = 0.16 \text{ fm}^4$ and additionally the dependence of the radii on the flow parameter for $N_{max} = 14$.

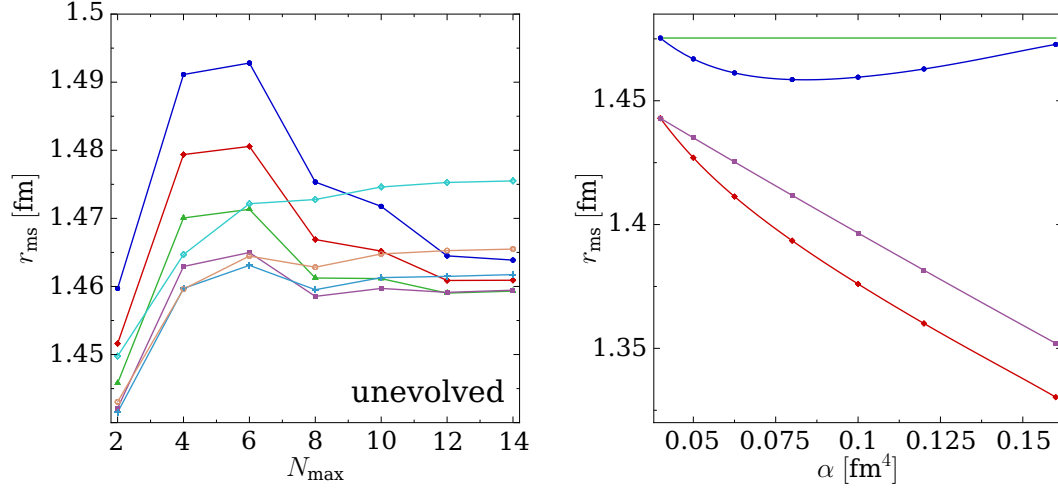


Figure 5.7: NCSM results for the ${}^4\text{He}$ nucleus for unevolved mean-square radii (left) for $\alpha = 0.04 \text{ fm}^4$ (●), $\alpha = 0.05 \text{ fm}^4$ (◆), $\alpha = 0.0625 \text{ fm}^4$ (▲), $\alpha = 0.08 \text{ fm}^4$ (■), $\alpha = 0.1 \text{ fm}^4$ (+), $\alpha = 0.12 \text{ fm}^4$ (○), and $\alpha = 0.16 \text{ fm}^4$ (◇). The dependence on the flow parameter for $N_{\text{max}} = 8$ for the unevolved (●) and the evolved (◆), as well as the unevolved with fixed α (—) and evolved with fixed α in the Hamiltonian (◆) is shown on the right.

Figure 5.8 shows results for evolved radii with Hamiltonians evolved up to the same flow parameter and results for consistent and inconsistent calculations using $\alpha = 0.04 \text{ fm}^4$ and for comparison also the differences $\Delta r_{\text{ms}} = [r_{\text{ms}}]^{\text{evolved}} - [r_{\text{ms}}]^{\text{unevolved}}$ for both cases. The plots show that convergence is obtained for larger N_{max} in case of the consistently and inconsistently evolved radii. In both cases the unitary transformation reduces the radius and leads to similar results. Also the differences are similar in both cases and show deviations of up to about 10% for the largest flow parameter considered. The unitary transformation sorts the radii by the flow parameter. In case of the unevolved radii, the converged results become lower for increasing flow parameter but move up again for $\alpha \geq 0.08 \text{ fm}^4$. This is caused by the explicit transformation of the radii and therewith a difference in the handling of induced many-body forces.

The comparison of the α -trend of the radii in Figure 5.7 with the Hartree-Fock results in Figure 5.4, shows a similar trend of the curves, but the NCSM results do not produce the crossings of the fully evolved with the unevolved curve as in the Hartree-Fock calculations. This can be explained by the mean-field approach in Hartree-Fock where the approximation becomes better with increasing flow parameter because more long-range correlations are included which cannot be described by the Hartree-Fock method for small values of the flow parameter. The general trend, that the unitary transformation leads to smaller radii and the difference of the transformed and bare radii increases with increasing flow parameter can be observed for both, the Hartree-Fock and the NCSM method. Since no convergence behaviour occurs in the NCSM results in contrast to the Hartree-Fock results, the convergence seems to be an artifact.

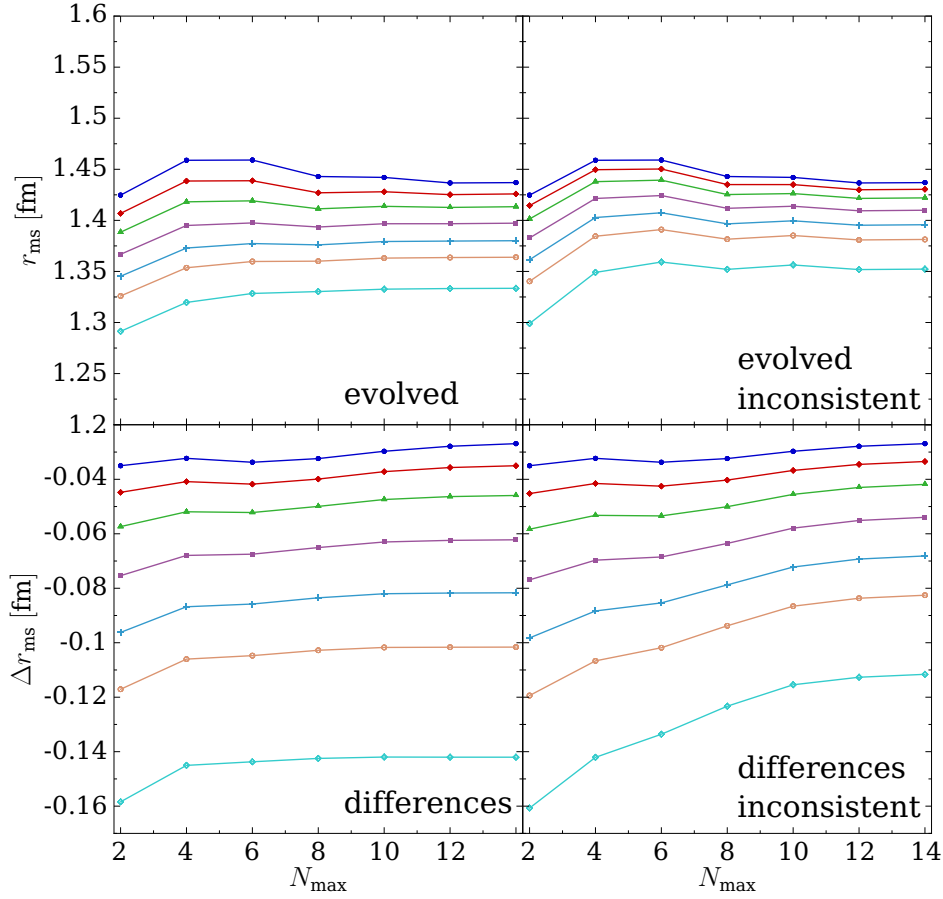


Figure 5.8: NCSM results for the ${}^4\text{He}$ nucleus for the for N3LO interactions with SRG-evolved mean-square radii using Hamiltonians which are evolved up to the same flow parameter (column lower left) or to $\alpha = 0.04 \text{ fm}^4$ (column lower right), respective, for $\alpha = 0.04 \text{ fm}^4$ (\bullet), $\alpha = 0.05 \text{ fm}^4$ (\blacklozenge), $\alpha = 0.0625 \text{ fm}^4$ (\blacktriangle), $\alpha = 0.08 \text{ fm}^4$ (\blacksquare), $\alpha = 0.1 \text{ fm}^4$ (\oplus), $\alpha = 0.12 \text{ fm}^4$ (\circ), and $\alpha = 0.16 \text{ fm}^4$ (\diamond).

5.3 Multipole Transition Operators

The reduced transition probability for an electric multipole transition is given by [23, 22, 21]

$$B^T(EJ, J_i \rightarrow J_f) = \frac{1}{2J_i + 1} |\langle i || Q_J^T || f \rangle|^2, \quad (5.18)$$

where J indicates the multipolarity of the transition, $T = 0, 1$ is the isospin and $\langle i || Q_J^T || f \rangle$ is the reduced matrix-element connecting the initial state $|i\rangle$ and the final state $|f\rangle$ by means of the multipole transition operator Q_J^T . The isoscalar monopole transition is given by

$$Q_{00}^0 = \sum_{i=1}^A x_i^2 Y_{00}(\vartheta_i, \varphi_i), \quad (5.19)$$

the isovector dipole excitations are described by the transition operator

$$Q_{1M}^1 = e \sum_{i=1}^A \tau_3^{(i)} x_i Y_{1M}(\vartheta_i, \varphi_i) \quad (5.20)$$

and the isoscalar quadrupole transition operator is defined as

$$Q_{2M}^0 = e \sum_{i=1}^A x_i^2 Y_{2M}(\vartheta_i, \varphi_i). \quad (5.21)$$

Here e is the elementary charge, τ_3 the third component of the isospin and $Y_{JM}(\vartheta, \varphi)$ are the spherical harmonics.

Since the unitary transformation only acts on the relative component of an operator, we express the isoscalar monopole and quadrupole operator in a decomposition into two-body relative and center of mass contributions:

$$Q_{00}^0 = \frac{1}{4(A-1)} \sum_{ij}^A [r_{ij}^2 Y_{00}(\mathbf{r}_{ij}) + 4X_{ij}^2 Y_{00}(\mathbf{X}_{ij})] \quad (5.22)$$

in case of the monopole and

$$Q_{2M}^0 = \frac{e}{4(A-1)} \sum_{ij}^A [r_{ij}^2 Y_{2M}(\mathbf{r}_{ij}) + 4X_{ij}^2 Y_{2M}(\mathbf{X}_{ij})], \quad (5.23)$$

for the quadrupole operator, with the two-body center of mass coordinates $X_{ij} = (x_i + x_j)/2$. The dipole operator can be expressed in a similar form, but the following discussions are restricted to monopole and quadrupole operators.

As for the radius operator, the two-body approximation is given by

$$\tilde{Q} = \tilde{Q}^{[1]} + \tilde{Q}^{[2]} = Q + \tilde{Q}^{[2]}, \quad (5.24)$$

where again $\tilde{Q}^{[1]} = Q$, i.e., the one-body part is given by the one-body transition operator. The two-body part of the unitarily transformed operator is obtained by applying equations (5.11)-(5.13) in two-body space and leads to

$$[\tilde{Q}_{00}^0]^{[2]} = \frac{1}{4} \sum_{ij}^A [U_{ij}^\dagger (r_{ij}^2 Y_{00}(\mathbf{r}_{ij})) U_{ij} - r_{ij}^2 Y_{00}(\mathbf{r}_{ij})] \quad (5.25)$$

in the case of the isoscalar monopole transition operator and

$$[\tilde{Q}_{2M}^0]^{[2]} = \frac{1}{4} \sum_{ij}^A \left[U_{ij}^\dagger (r_{ij}^2 Y_{2M}(\mathbf{r}_{ij})) U_{ij} - r_{ij}^2 Y_{2M}(\mathbf{r}_{ij}) \right] \quad (5.26)$$

for the isoscalar quadrupole transition operator.

5.3.1 Transition Operators in the RPA Framework

The RPA (see Appendix B for details) is a simple method to calculate excited states of nuclei. In the following it will be used to investigate the effect of unitary transformations via UCOM and SRG, respective, on the transitions to the excited states. The transition amplitude

$$\langle \omega | Q_{JM}^{T\dagger} | \text{RPA} \rangle \quad (5.27)$$

has to be evaluated for that purpose. Here $|\omega\rangle = Q_\omega^\dagger | \text{RPA} \rangle$ is the excited state and $| \text{RPA} \rangle$ is the RPA ground-state. Rewriting (5.27) leads to

$$\begin{aligned} \langle \text{RPA} | Q_{JM}^T | \omega \rangle &= \langle \text{RPA} | Q_{JM}^T Q_\omega^\dagger | \text{RPA} \rangle = \langle \text{RPA} | [Q_{JM}^T, Q_\omega^\dagger] | \text{RPA} \rangle \\ &= \langle \text{HF} | [Q_{JM}^T, Q_\omega^\dagger] | \text{HF} \rangle, \end{aligned} \quad (5.28)$$

where in the last step the quasi-boson approximation [23] was applied. Here the Hartree-Fock ground-state is denoted by $| \text{HF} \rangle$. The commutator could be introduced because $Q_\omega | \text{RPA} \rangle = 0$ and therefore the second term will vanish (cf. Appendix A).

The transition matrix-elements for a bare one-body operator Q_{JM}^T are given by

$$\sum_M \langle \text{HF} | [Q_{JM}^T, Q_\omega^\dagger] | \text{HF} \rangle = \sum_{ph} \frac{1}{\hat{j}} \langle p || Q_J^T || h \rangle [X_{ph}^{\nu J} + (-1)^{J+1} Y_{ph}^{\nu J}], \quad (5.29)$$

with $\hat{j} = 2J + 1$. Here p indicates states above the Fermi energy (particles) and h indicates states below the Fermi energy (holes) and the forward and backward amplitudes X_{ph}^ν and Y_{ph}^ν .

The unitary UCOM or SRG transformation of a multipole operator leads to a structure with many-body contributions. As in the previous chapters the two-body approximation will be considered in the following. The matrix-elements of the two-body contribution can be evaluated to

$$\begin{aligned}
 \sum_M \langle \text{HF} | [Q_{JM}^T]^{[2]}, Q_{\omega JM}^\dagger | \text{HF} \rangle &= \sum_{phh'J_1J_2} (-1)^{1-J+j_{h'}} \frac{\hat{J}_1 \hat{J}_2}{\hat{J}} \begin{Bmatrix} j_p & j_h & J \\ J_1 & J_2 & j_{h'} \end{Bmatrix} \\
 &\left[(-1)^{j_h+J_1} \langle h'hJ_1 || [Q_J^T]^{[2]} || h'pJ_2 \rangle X_{ph}^{(\nu,J)} \right. \\
 &\left. + (-1)^{j_p+J_2} \langle h'pJ_1 || [Q_J^T]^{[2]} || h'hJ_2 \rangle Y_{ph}^{(\nu,J)} \right], \quad (5.30)
 \end{aligned}$$

where $[Q_{JM}^T]^{[2]}$ is the two-body part of the transition operator. The reduced matrix-elements $\langle h'hJ_1 || [Q_J^T]^{[2]} || h'pJ_2 \rangle$ connects two-body states via the two-body contribution of the transition operator. The derivation of this equation can be found in Appendix B.3. The transition amplitude including the one-body and two-body contribution of the transition operator is now given by

$$B^T(EJ, J_i \rightarrow J_f) = \frac{1}{2J_i + 1} |\langle i || Q_J^T || f \rangle + \langle i || [Q_J^T]^{[2]} || f \rangle|^2. \quad (5.31)$$

In the following also strength functions will be shown which are obtained by convolving the calculated discrete strength distributions with a Lorentzian function leading to a continuous energy-dependent strength function [21, 47]:

$$R_J^T(E) = \sum_{\nu} B_J^T(\omega_{\nu}) \frac{1}{\pi} \frac{\Gamma/2}{(E - \omega_{\nu})^2 + (\Gamma/2)^2}. \quad (5.32)$$

The width of the Lorentzian distribution is set to the arbitrary value of $\Gamma = 2$ MeV. The form of the continuous strength function is chosen such that energy-weighted sum of the matrix-elements of the transition strength is equal to the integral over the continuous energy-dependent strength function

$$\sum_{\nu} E_{\nu} B_J^T(\omega_{\nu}) = \int dE E R_J^T(E). \quad (5.33)$$

5.3.2 Giant Multipole Resonances

The effect of the unitary transformation to the multipole transitions obtained with RPA calculations will be examined in the following. In addition NCSM calculations of quadrupole transitions are discussed.

Isoscalar Giant Monopole Resonance with SRG-Transformed Operators

The isoscalar giant monopole resonance can be described as a spherically symmetric oscillation or a compression of a nucleus, which means that protons and neutrons move in phase.

In Figure 5.9 the isoscalar monopole (ISM) strength function for ^{16}O , ^{40}Ca , ^{90}Zr and

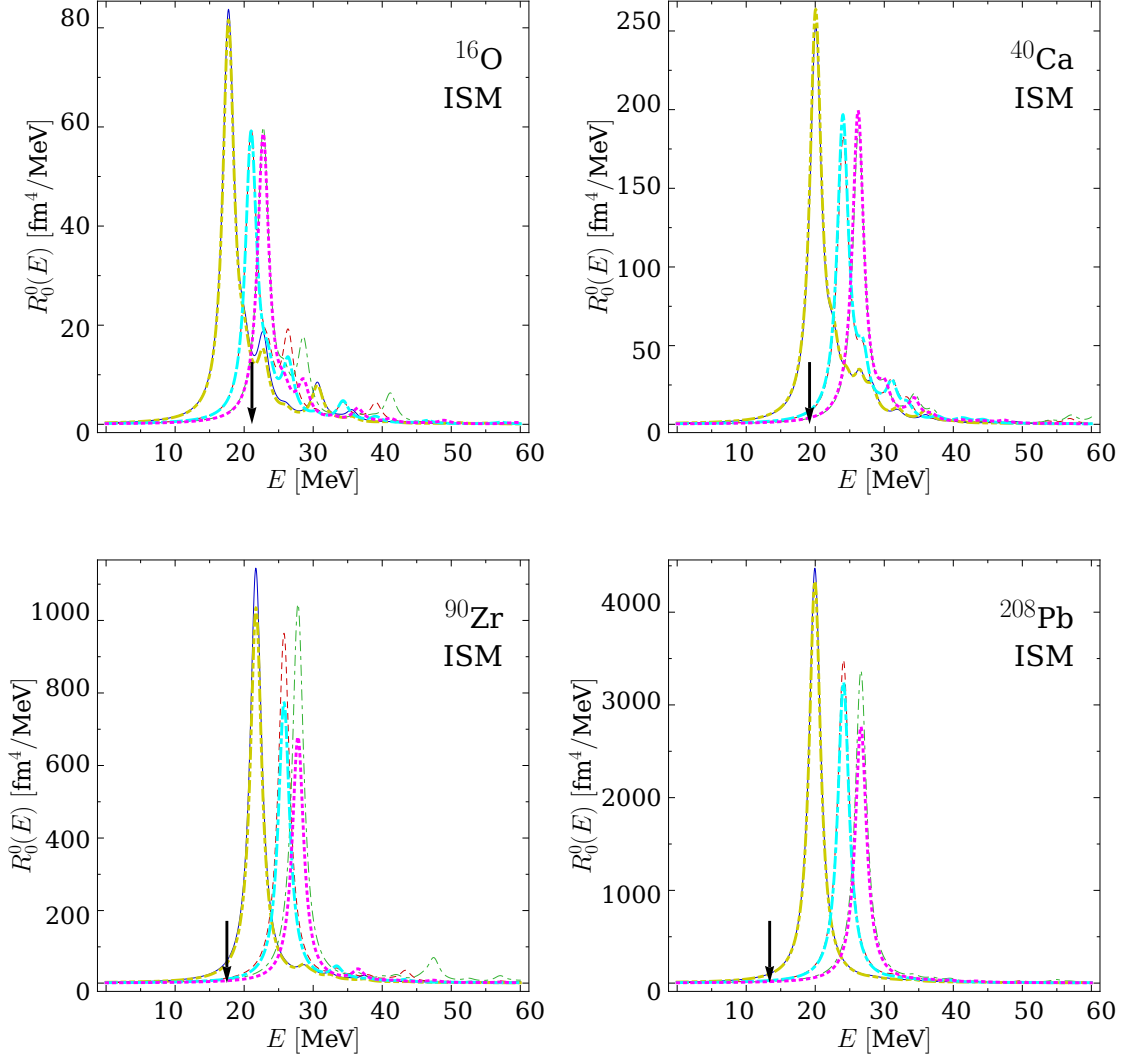


Figure 5.9: Isoscalar monopole strength distribution for ^{16}O , ^{40}Ca , ^{90}Zr and ^{208}Pb for the SRG evolved transition operator with flow parameters $\alpha = 0.04 \text{ fm}^4$ (—), $\alpha = 0.08 \text{ fm}^4$ (---) and $\alpha = 0.16 \text{ fm}^4$ (-.-.-) and the unevolved transition operators with flow parameters $\alpha = 0.04 \text{ fm}^4$ (---), $\alpha = 0.08 \text{ fm}^4$ (-.-.-) and $\alpha = 0.16 \text{ fm}^4$ (.....). The arrow indicates the centroid energy from experiment [68, 69, 70].

^{208}Pb is shown for the untransformed and the SRG-transformed monopole transition operator with flow parameters $\alpha = 0.04 \text{ fm}^4$, $\alpha = 0.08 \text{ fm}^4$ and $\alpha = 0.16 \text{ fm}^4$ for the N3LO interaction. The arrow indicates the experimental centroid which can be extracted from experiment. For ^{16}O the main peak of the response function for $\alpha = 0.08 \text{ fm}^4$ is in good agreement with experiment, for ^{40}Ca the response function for $\alpha = 0.04 \text{ fm}^4$ fits very well. For the heavier nuclei the peaks are shifted to higher energies in comparison to experiment. For all considered nuclei the peaks of the strength functions are shifted towards higher energies with increasing flow parameter. This shift is caused by the spreading of the Hartree-Fock single particle spectra for in-

creasing flow parameters. The shift leading to the higher excitation energies makes a transition more difficult which leads to smaller strengths. This effect can be observed in the figure as well, i.e., with increasing flow parameter the peaks are shifted and the strength decreases. The unitary transformation of the transition operator leads to higher peaks in the response functions of ^{16}O , ^{90}Zr and ^{208}Pb , but to smaller peaks for ^{40}Ca , where the effect of the transformation becomes larger for increasing flow parameters. In addition, at high energies additional structures in the strength functions appear.

The reduced matrix-elements of the one- and two-body contributions to the transition strength as well as the unevolved and evolved discrete transition strength and their difference $\Delta B_0^0 = [B_0^0]^{\text{evolved}} - [B_0^0]^{\text{unevolved}}$ are shown in Figure 5.10 for ^{16}O , in Figure 5.11 for ^{40}Ca , in Figure 5.12 for ^{90}Zr and in Figure 5.13 for ^{208}Pb . The reduced matrix-elements of the two-body contribution are smaller than the one-body part and have more strength at higher energies, whereas the one-body matrix-elements have more strength in the region of the peak in the Lorentzian functions. The increase of the flow parameter leads to larger matrix-elements of the two-body part and is therefore in good agreement with the observations made for the strengths functions discussed before.

The bare and evolved strengths and their differences show that the unitary transformation leads to an increase of strength for the considered nuclei except ^{40}Ca . The larger the flow parameter, the larger the difference of the transformed and untransformed strength. In case of ^{40}Ca the transformation leads to smaller values for the strength for all flow parameters, where the difference is largest for $\alpha = 0.08 \text{ fm}^4$. The deviations of the transformed and the untransformed strengths reaches 10% in the case of ^{16}O with the largest flow parameter, 5% in case of ^{40}Ca , about 30% in case of ^{90}Zr and 13% for ^{208}Pb .

Intuitively one would expect the unitary transformation of the transition operators to show similar effects as for the charge radii. Since the discussion of the radii is based on the mean-square radius, which is averaged over the particle number a direct comparison is not possible. In order to compare the results one would have to divide the reduced two-body matrix-elements $\langle \omega || Q^{[2]} || \text{RPA} \rangle$ by the respective particle number and use them to calculate the response function. This will lead to smaller two-body contributions due to the unitary transformation.

Isoscalar Giant Monopole Resonance with UCOM Transformed Operators

The ISM strength distribution for the UCOM-transformed transition operator for ^{16}O , ^{40}Ca , ^{90}Zr and ^{208}Pb is shown in Figure 5.14 for the AV18 interaction with correlator sets A0 and A1. For the three lighter nuclei the experimental centroid is underestimated by the results with correlator set A0 and overestimated with correlator set A1. For ^{208}Pb both response functions have a peak at higher energies than the experimental value. For all nuclei the difference of the unitary transformed and bare response function is very small. Correlator set A1 leads to peaks at higher energies

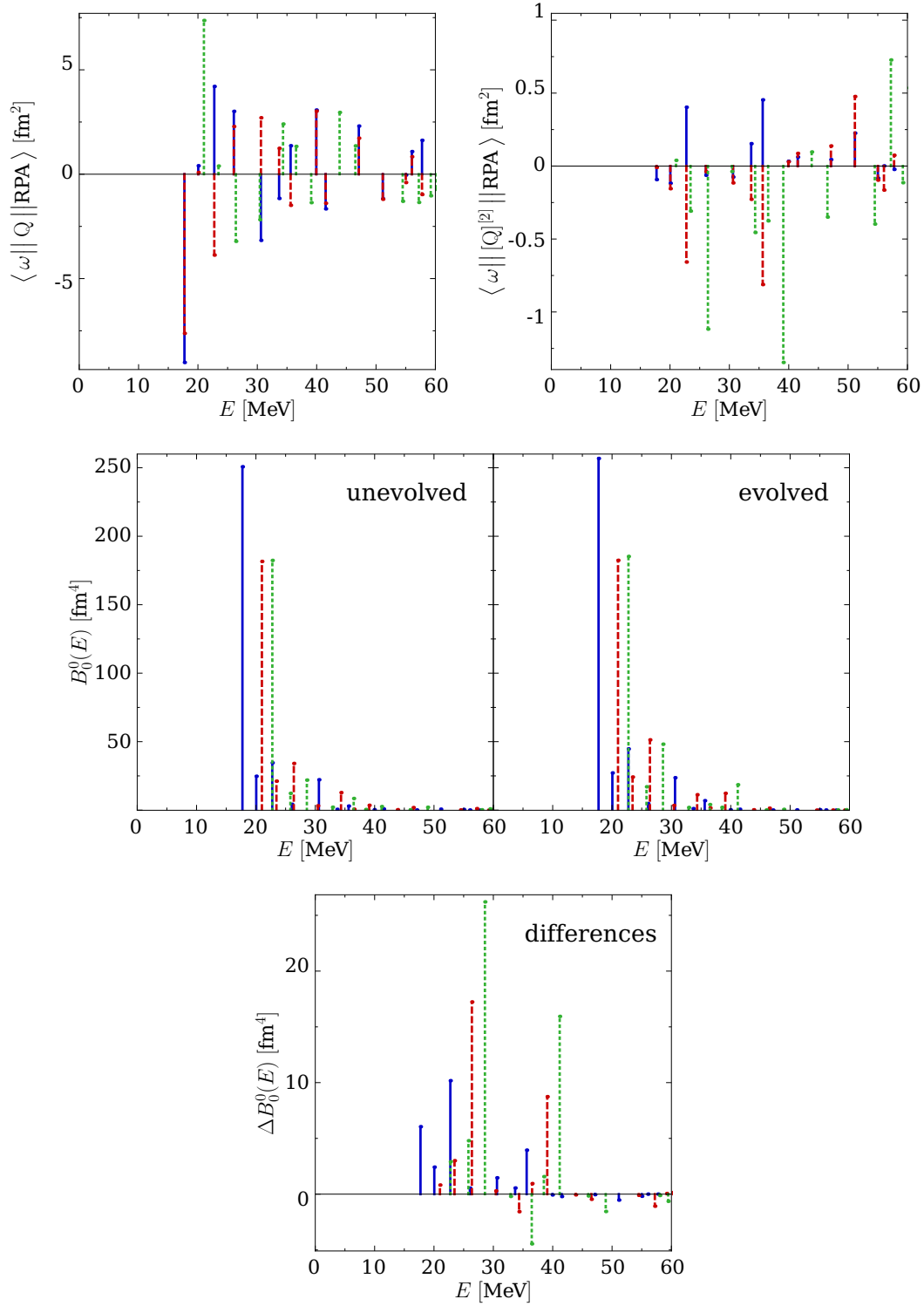


Figure 5.10: Reduced matrix-elements of the one-body (upper left) and two-body (upper right) contribution of the transition operator for the isoscalar monopole transition of the ^{16}O nucleus and the unevolved (middle, left) and evolved matrix-elements (middle, right) and their differences (bottom). The flow parameters used are $\alpha = 0.04 \text{ fm}^4$ (—), $\alpha = 0.08 \text{ fm}^4$ (---) and $\alpha = 0.16 \text{ fm}^4$ (·····).

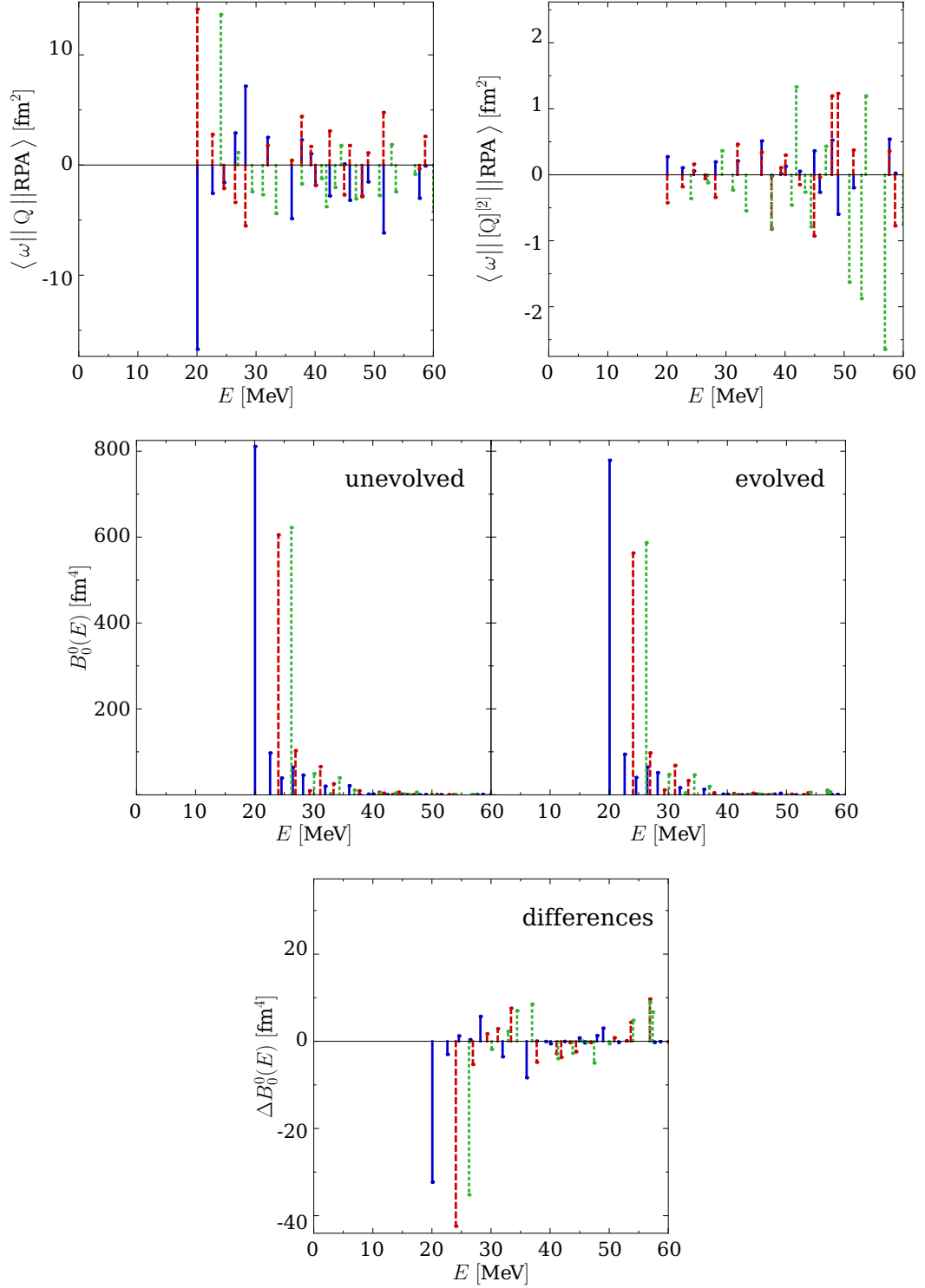


Figure 5.11: Reduced matrix-elements of the one-body (upper left) and two-body (upper right) contribution of the transition operator for the isoscalar monopole transition of the ^{40}Ca nucleus and the unevolved (middle, left) and evolved matrix-elements (middle, right) and their differences (bottom). The flow parameters used are $\alpha = 0.04 \text{ fm}^4$ (—), $\alpha = 0.08 \text{ fm}^4$ (---) and $\alpha = 0.16 \text{ fm}^4$ (·····).

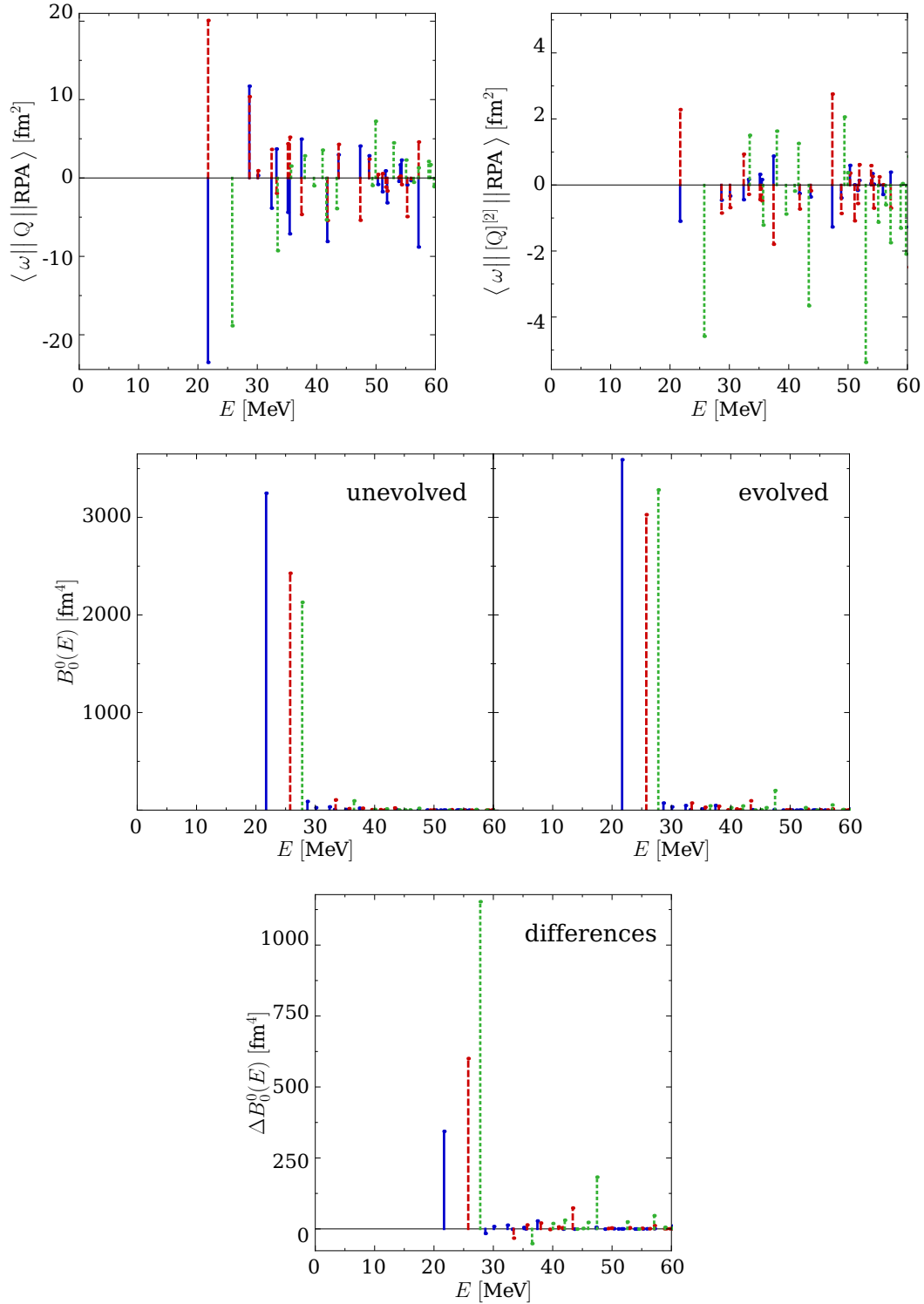


Figure 5.12: Reduced matrix-elements of the one-body (upper left) and two-body (upper right) contribution of the transition operator for the isoscalar monopole transition of the ^{90}Zr nucleus and the unevolved (middle, left) and evolved matrix-elements (middle, right) and their differences (bottom). The flow parameters used are $\alpha = 0.04 \text{ fm}^4$ (—), $\alpha = 0.08 \text{ fm}^4$ (---) and $\alpha = 0.16 \text{ fm}^4$ (·····).

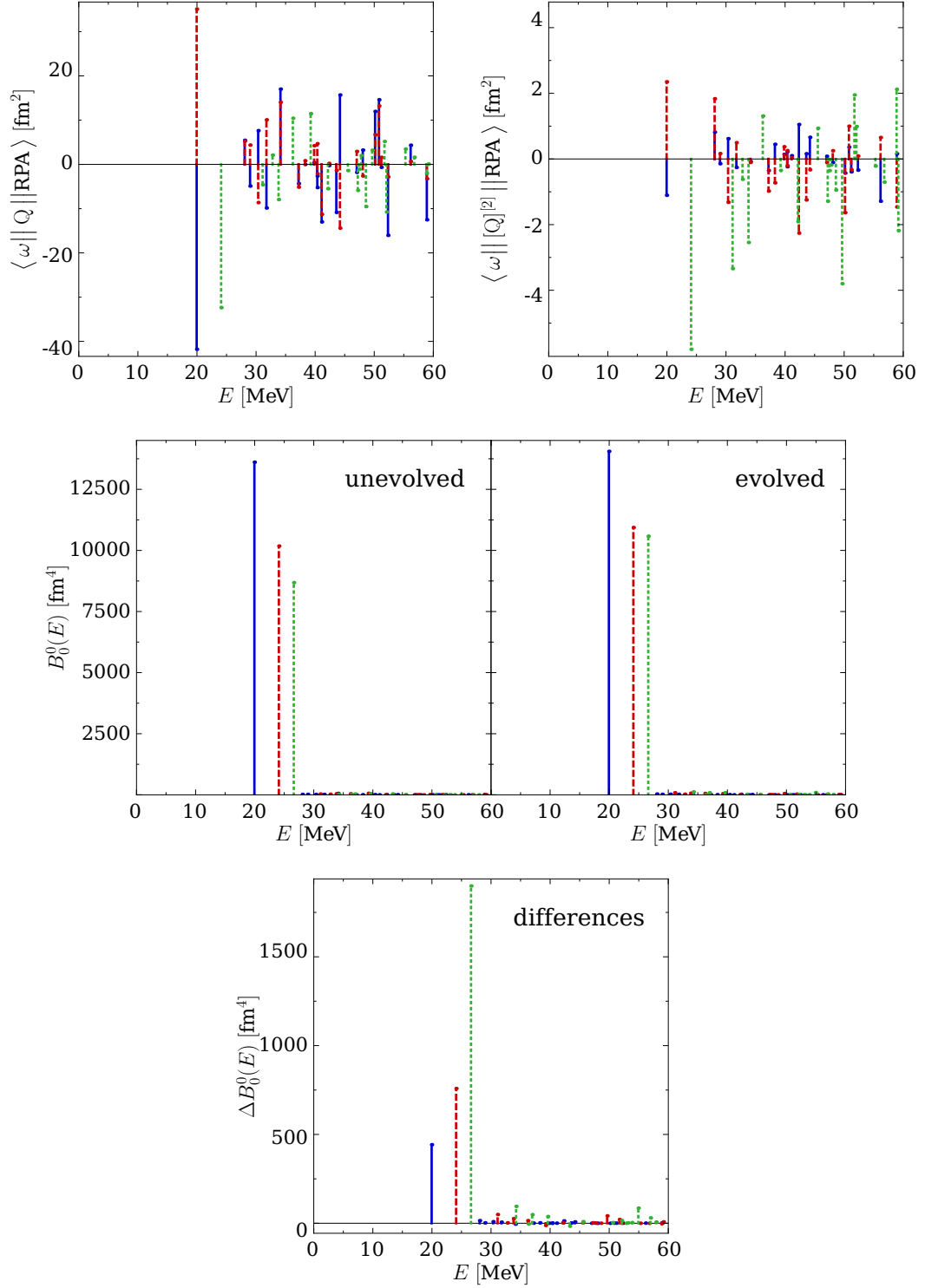


Figure 5.13: Reduced matrix-elements of the one-body (upper left) and two-body (upper right) contribution of the transition operator for the isoscalar monopole transition of the ^{208}Pb nucleus and the unevolved (middle, left) and evolved matrix-elements (middle, right) and their differences (bottom). The flow parameters used are $\alpha = 0.04 \text{ fm}^4$ (—), $\alpha = 0.08 \text{ fm}^4$ (---) and $\alpha = 0.16 \text{ fm}^4$ (·····).

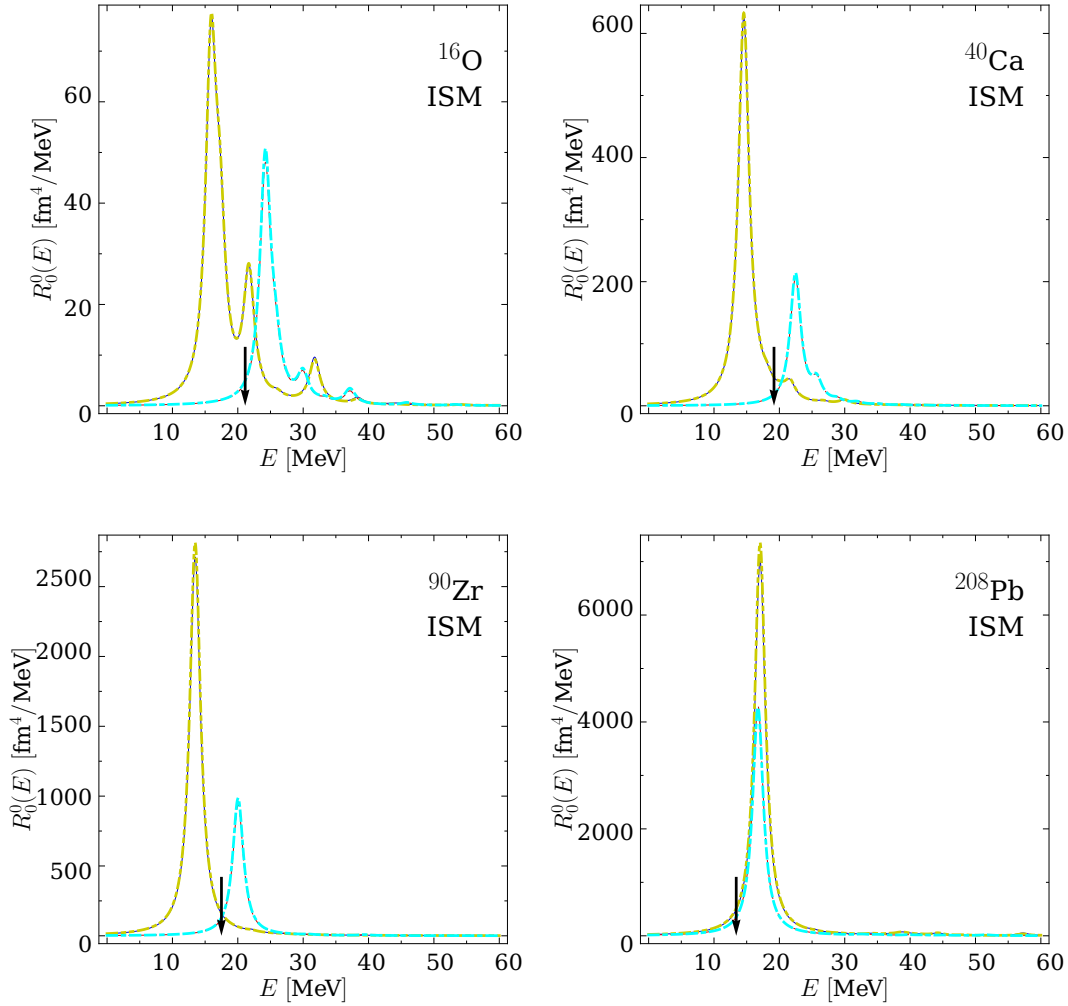


Figure 5.14: Isoscalar monopole strength distribution for ^{16}O , ^{40}Ca , ^{90}Zr and ^{208}Pb for the unitary transformed transition operator using UCOM correlator set A0 (—) and A1 (---) and the untransformed transition operators for A0 (····) and A1 (-·-·-). The arrow indicates the centroid energy from experiment [68, 69, 70].

than correlator set A0 except for ^{208}Pb , where they are at slightly smaller energies. The suppression of strength and the shift to higher energies are similar to the observations for the SRG with increasing flow parameters. But in contrast to the SRG the effect of the unitary transformation is very small. Since the transition operators are sensitive to long-range effects and the UCOM is restricted to short ranges, the transformation has only small effects on the operator. In case of the SRG there is no strict separation of long- and short-range correlations and, therefore, a different behaviour is expected. Since the SRG calculations are performed with the N3LO interaction while in the UCOM the AV18 interaction is used it is clear that the results can only be compared schematically because these two potentials have a completely different structure and, therefore, lead to different contributions in the states and operators

during transformation.

Isoscalar Giant Quadrupole Resonance with SRG-Transformed Operators

The isoscalar quadrupole (ISQ) strength distributions are investigated next. The ISQ distributions for ^{16}O , ^{40}Ca , ^{90}Zr and ^{208}Pb are shown in Figure 5.15 with the unevolved and SRG-evolved strength operators for the N3LO interaction using the flow parameters $\alpha = 0.04 \text{ fm}^4$, $\alpha = 0.08 \text{ fm}^4$, and $\alpha = 0.16 \text{ fm}^4$. The peaks of the response functions are shifted towards larger energies in comparison to the experimental values, except for the low-lying 2^+ state in ^{208}Pb , which is in good agreement with experiment for the smallest flow parameter while the other flow parameters overestimate this energy. The effect of the SRG transformation is very small for all four nuclei and all flow parameters.

The effect of the unitary transformation on the quadrupole transition operator are now investigated in more detail. The reduced one- and two-body matrix-elements as well as the unevolved and evolved discrete strength distributions and their differences are shown in Figure 5.16 for ^{16}O , in Figure 5.17 for ^{40}Ca , in Figure 5.18 in case of ^{90}Zr and in Figure 5.19 for the ^{208}Pb nucleus. For all nuclei the two-body matrix-elements are larger for larger flow parameters and their contributions are shifted to higher energies in comparison to the one-body part. The effect of the transformation cannot be seen at the unevolved and evolved strength distributions. The difference shows that the unitary transformation leads to changes of about 1% for all nuclei.

Comparing these observations for the ISQ transitions with the ISM transitions the effect of the SRG transformation is much smaller in case of the quadrupole. A possible explanation for this is, that a one-body operator with momentum transfer $q \rightarrow 0$ is chosen as the ansatz for the quadrupole transition operator. In case of the monopole an additional r^2 term is introduced in the equation to obtain results different from zero. This difference in the operators might be responsible for the difference in the effect of the transformation.

Isoscalar Giant Quadrupole Resonance with UCOM Transformed Operators

The ISQ strength distributions for the UCOM correlated quadrupole operator are shown in Figure 5.20 for the ^{16}O , ^{40}Ca , ^{90}Zr and ^{208}Pb nuclei for the AV18 interaction using correlator sets A0 and A1. For both correlator sets the peaks of the response functions are at higher energies than the experimental centroid except the low-lying 2^+ excitation in ^{208}Pb which is well described by correlator set A1. As in case of the monopole transitions the peaks of the strength functions are shifted to larger energies for A1 in comparison to A0 and they have less strength. This means that the probability for a transition is higher for correlator set A0. The effect of the unitary transformation is very small, as for the ISM strength distributions. A comparison with the SRG results is very difficult here because the effect of the UCOM transformation on the quadrupole transition operator is very small in contrast to the SRG results and

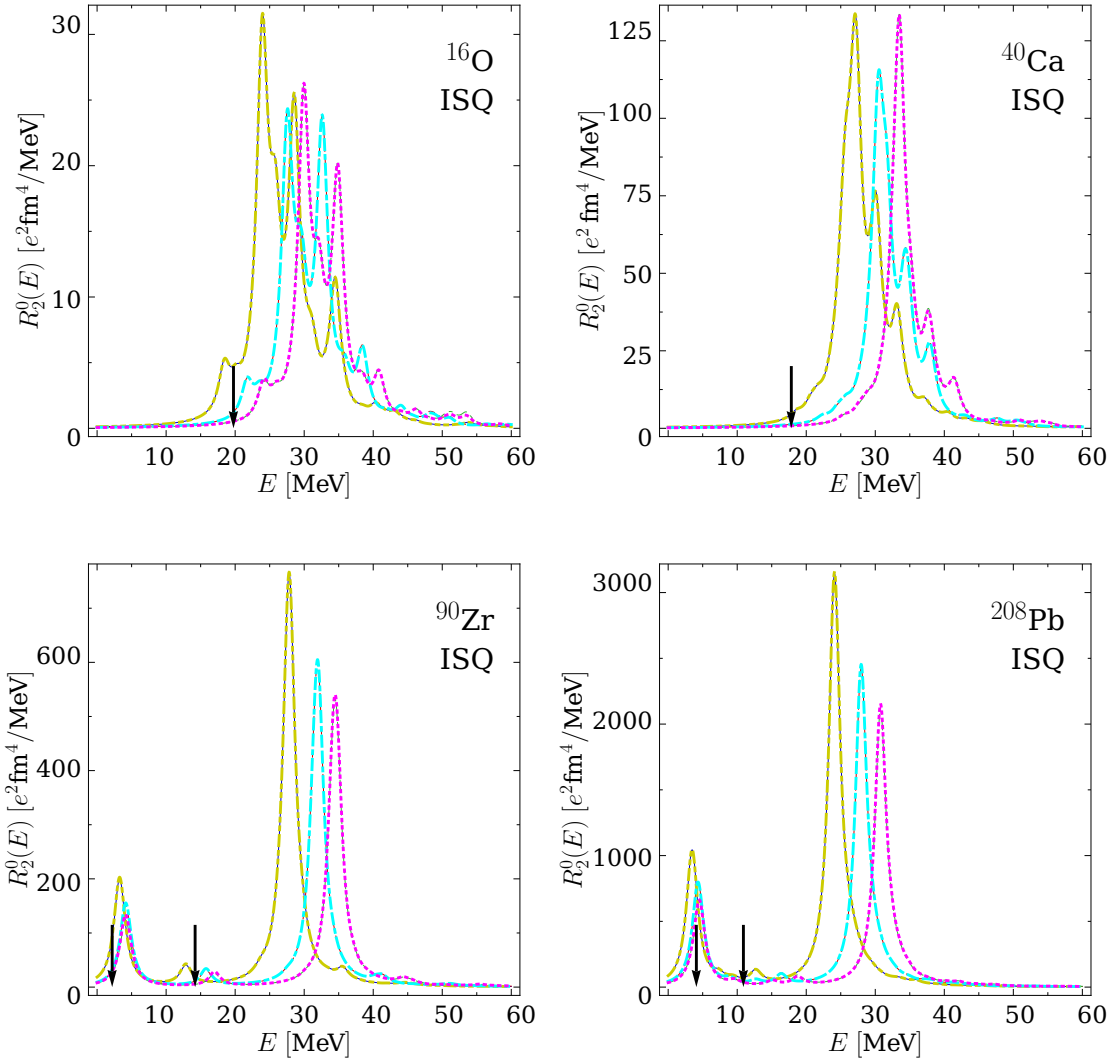


Figure 5.15: Isoscalar quadrupole strength distribution for ¹⁶O, ⁴⁰Ca, ⁹⁰Zr and ²⁰⁸Pb for the SRG evolved transition operator with flow parameters $\alpha = 0.04$ fm⁴ (—), $\alpha = 0.08$ fm⁴ (---) and $\alpha = 0.16$ fm⁴ (-.-.-) and the unevolved transition operators with flow parameters $\alpha = 0.04$ fm⁴ (-.-.-), $\alpha = 0.08$ fm⁴ (-.-.-) and $\alpha = 0.16$ fm⁴ (-.-.-). The arrow indicates the centroid energy from experiment [68]-[71].

therefore the one cannot distinguish between effects of the underlying interaction and the transformed operator.

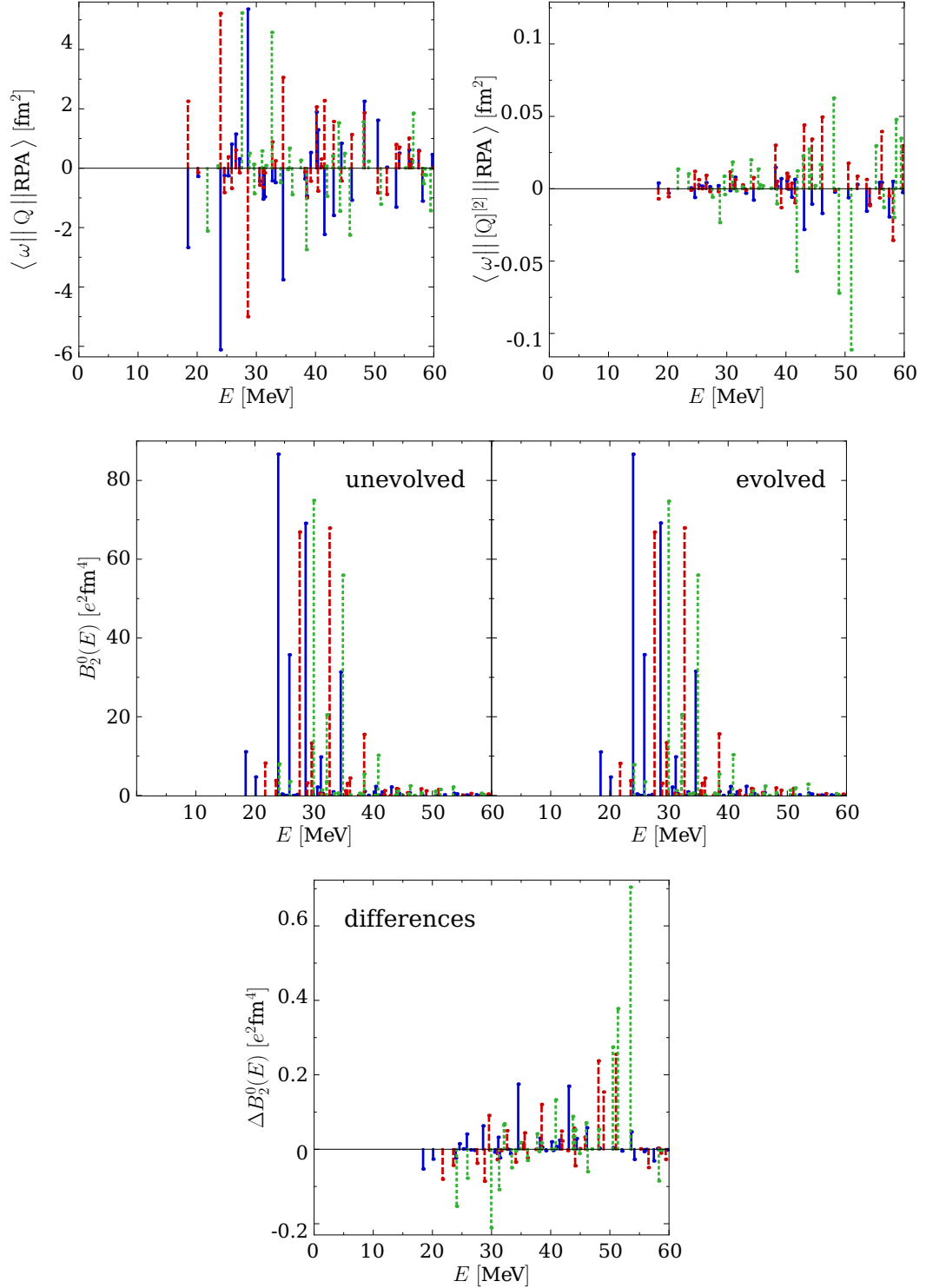


Figure 5.16: Reduced matrix-elements of the one-body (upper left) and two-body (upper right) contribution of the transition operator for the isoscalar quadrupole transition of the ^{16}O nucleus and the unevolved (middle, left) and evolved matrix-elements (middle, right) and their differences (bottom). The flow parameters used are $\alpha = 0.04 \text{ fm}^4$ (—), $\alpha = 0.08 \text{ fm}^4$ (---) and $\alpha = 0.16 \text{ fm}^4$ (·····).

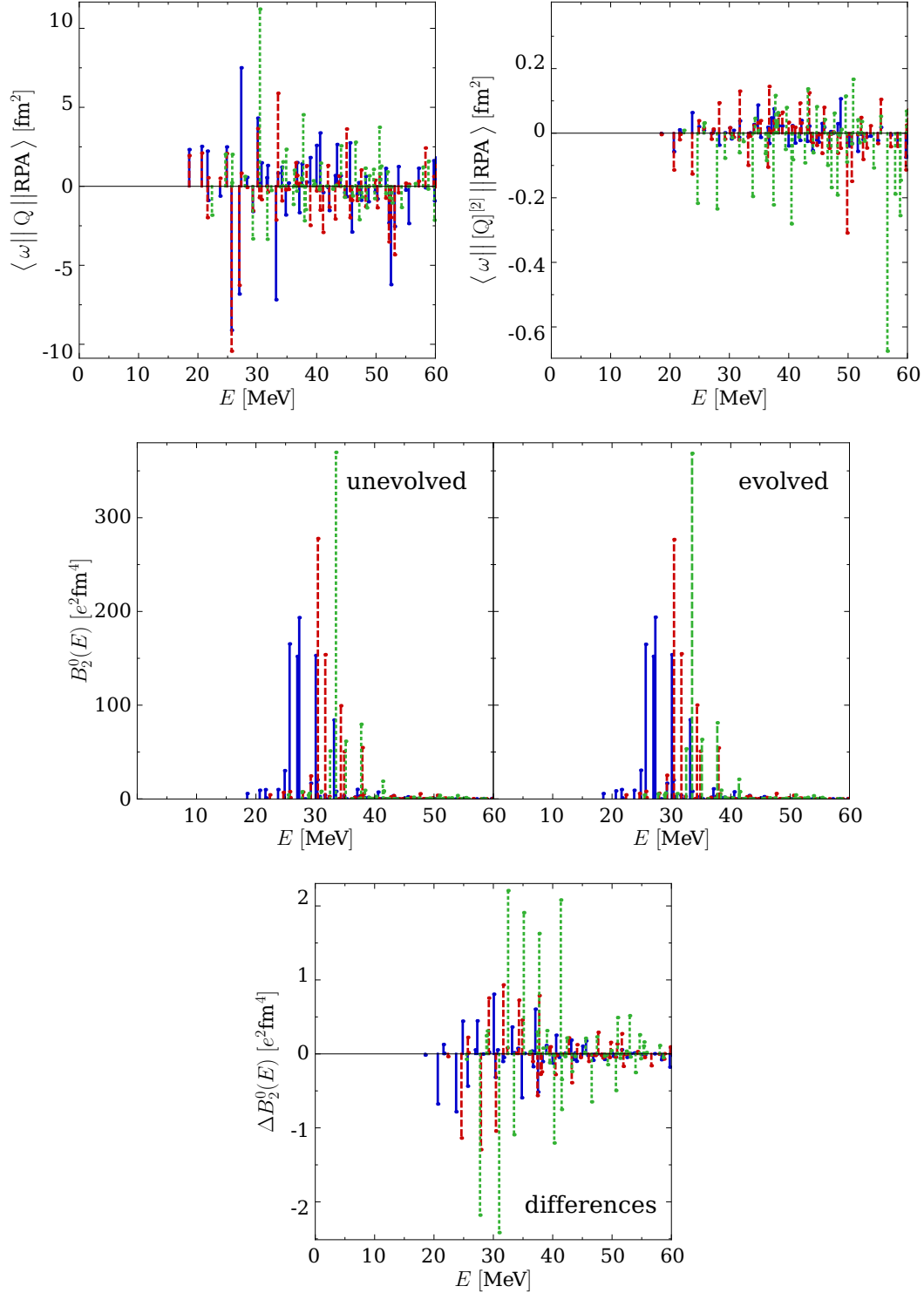


Figure 5.17: Reduced matrix-elements of the one-body (upper left) and two-body (upper right) contribution of the transition operator for the isoscalar quadrupole transition of the ^{40}Ca nucleus and the unevolved (middle, left) and evolved matrix-elements (middle, right) and their differences (bottom). The flow parameters used are $\alpha = 0.04 \text{ fm}^4$ (—), $\alpha = 0.08 \text{ fm}^4$ (---) and $\alpha = 0.16 \text{ fm}^4$ (····).

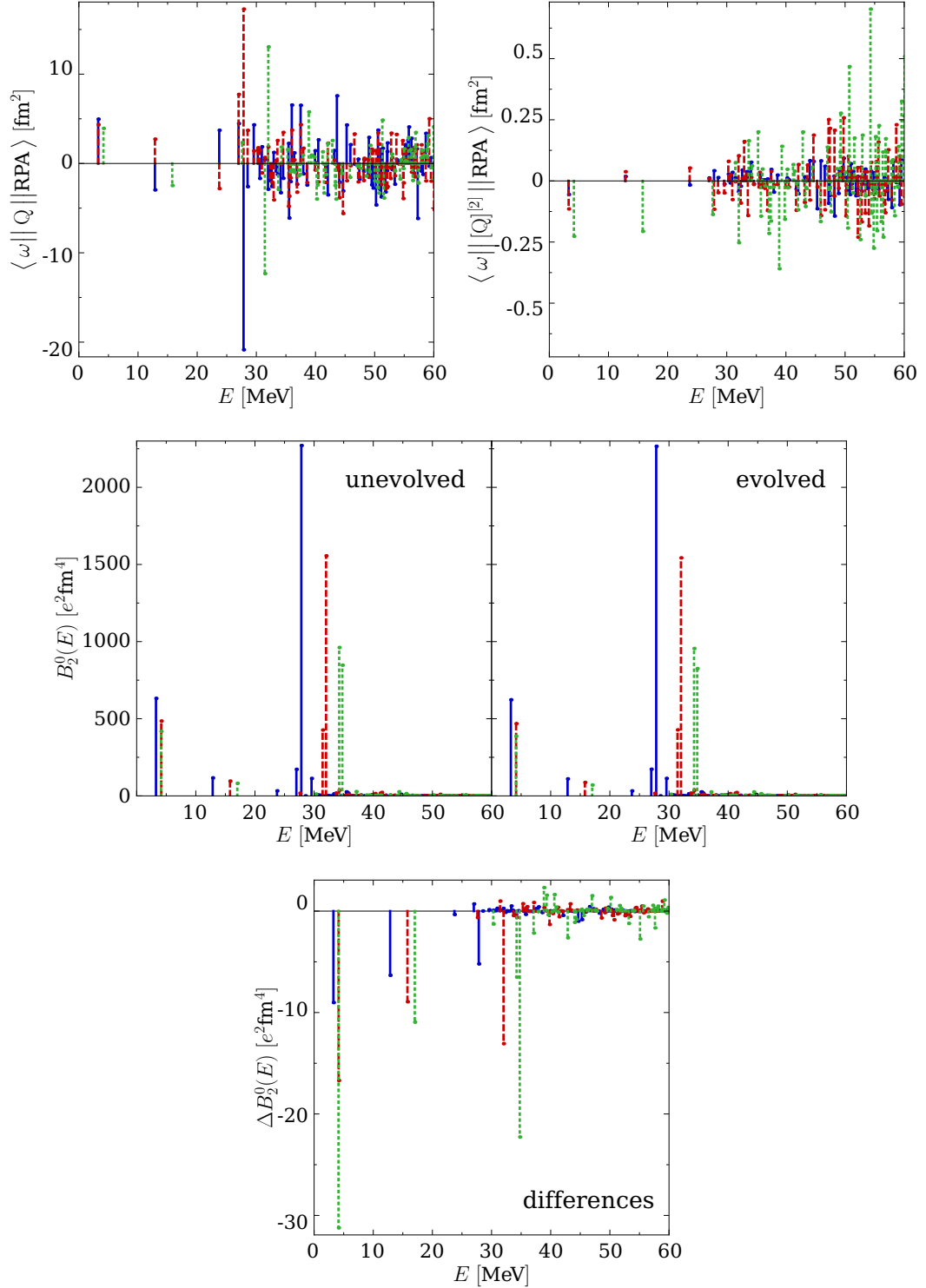


Figure 5.18: Reduced matrix-elements of the one-body (upper left) and two-body (upper right) contribution of the transition operator for the isoscalar quadrupole transition of the ^{90}Zr nucleus and the unevolved (middle, left) and evolved matrix-elements (middle, right) and their differences (bottom). The flow parameters used are $\alpha = 0.04$ fm⁴ (—), $\alpha = 0.08$ fm⁴ (---) and $\alpha = 0.16$ fm⁴ (·····).

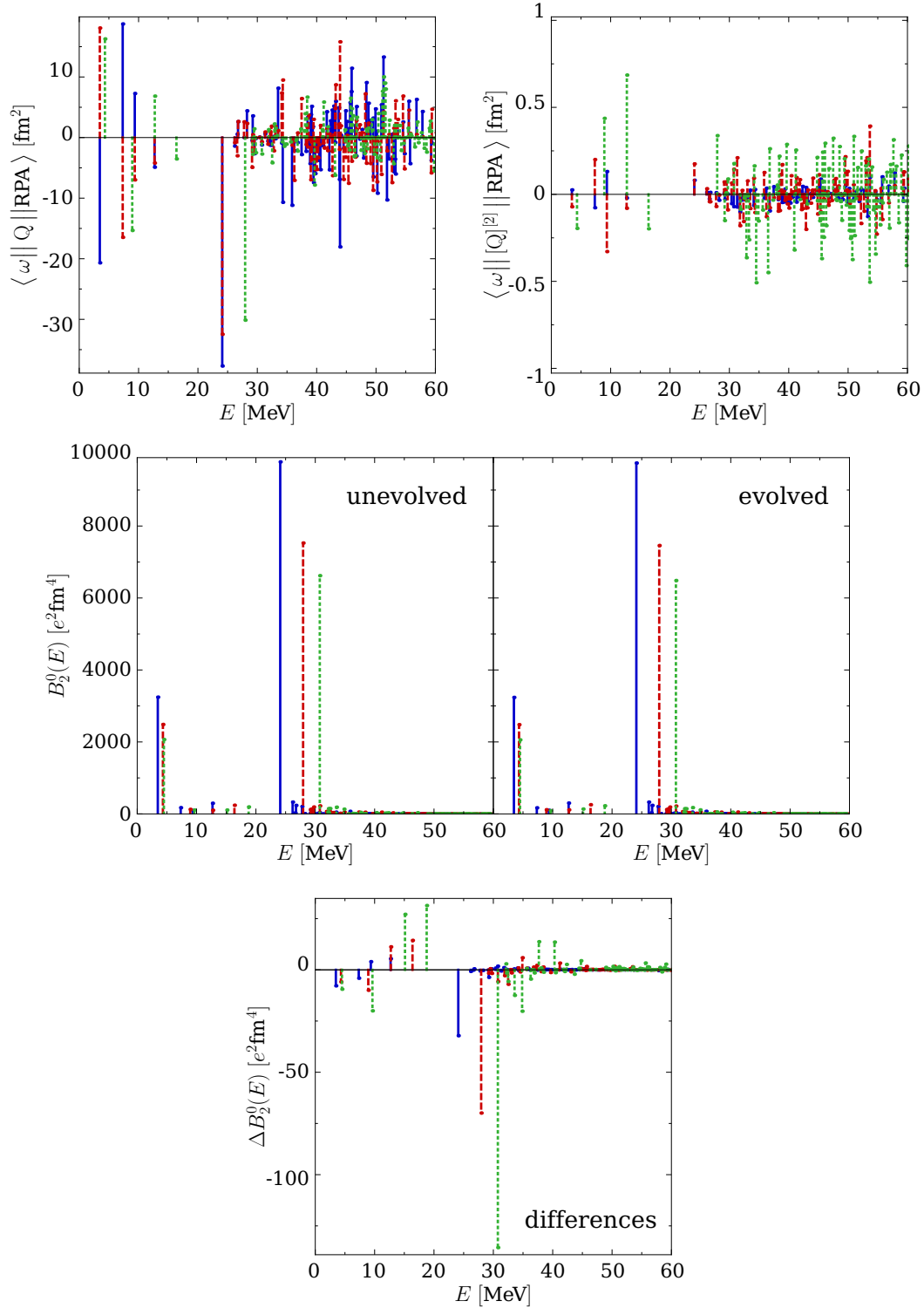


Figure 5.19: Reduced matrix-elements of the one-body (upper left) and two-body (upper right) contribution of the transition operator for the isoscalar quadrupole transition of the ^{208}Pb nucleus and the unevolved (middle, left) and evolved matrix-elements (middle, right) and their differences (bottom). The flow parameters used are $\alpha = 0.04$ fm^4 (—), $\alpha = 0.08$ fm^4 (---) and $\alpha = 0.16$ fm^4 (····).

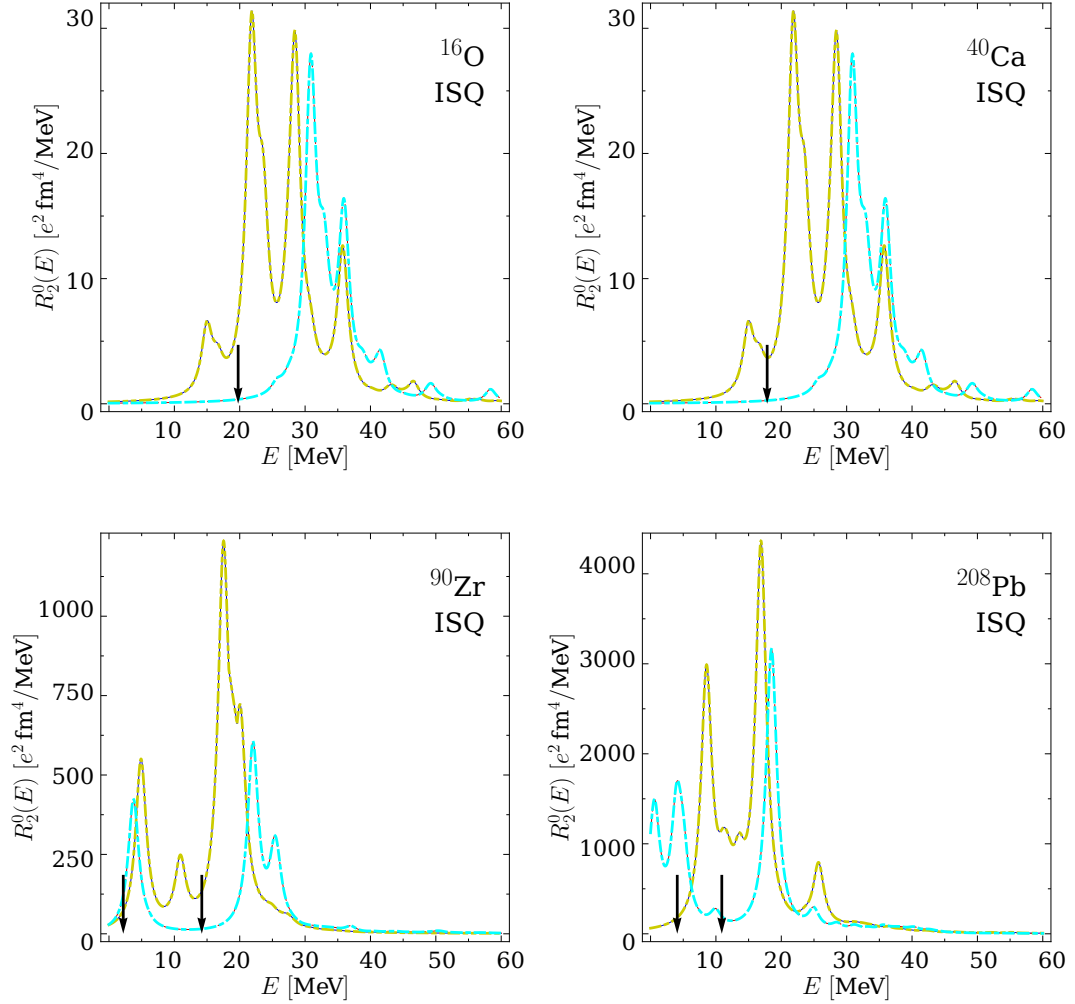


Figure 5.20: Isoscalar quadrupole strength distribution for ^{16}O , ^{40}Ca , ^{90}Zr and ^{208}Pb for the unitary transformed transition operator using UCOM correlator set A0 (—) and A1 (---) and the untransformed transition operators for A0 (····) and A1 (-·-·-). The arrow indicates the centroid energy from experiment [68]-[71].

5.3.3 NCSM Calculations with SRG-Transformed Quadrupole Transition Strengths

The ISQ strengths of the transition from the 3^+ state to the 1^+ ground-state of the ^6Li nucleus obtained with NCSM calculations¹ of the bare and SRG-evolved quadrupole operator as well as their difference are shown in Figure 5.21 for a set of flow parameters ranging from $\alpha = 0.04 \text{ fm}^4$ up to $\alpha = 0.16 \text{ fm}^4$. As in case of the NCSM calculations with the radii discussed in Section 5.2.2, the calculations are not converged. Increasing the flow parameter leads to increasing strength, where the difference of the α -curves becomes larger for increasing N_{max} . The evolution leads to an increase

¹The calculations for $N_{\text{max}} = 10$ are obtained with the IT-NCSM method [72].

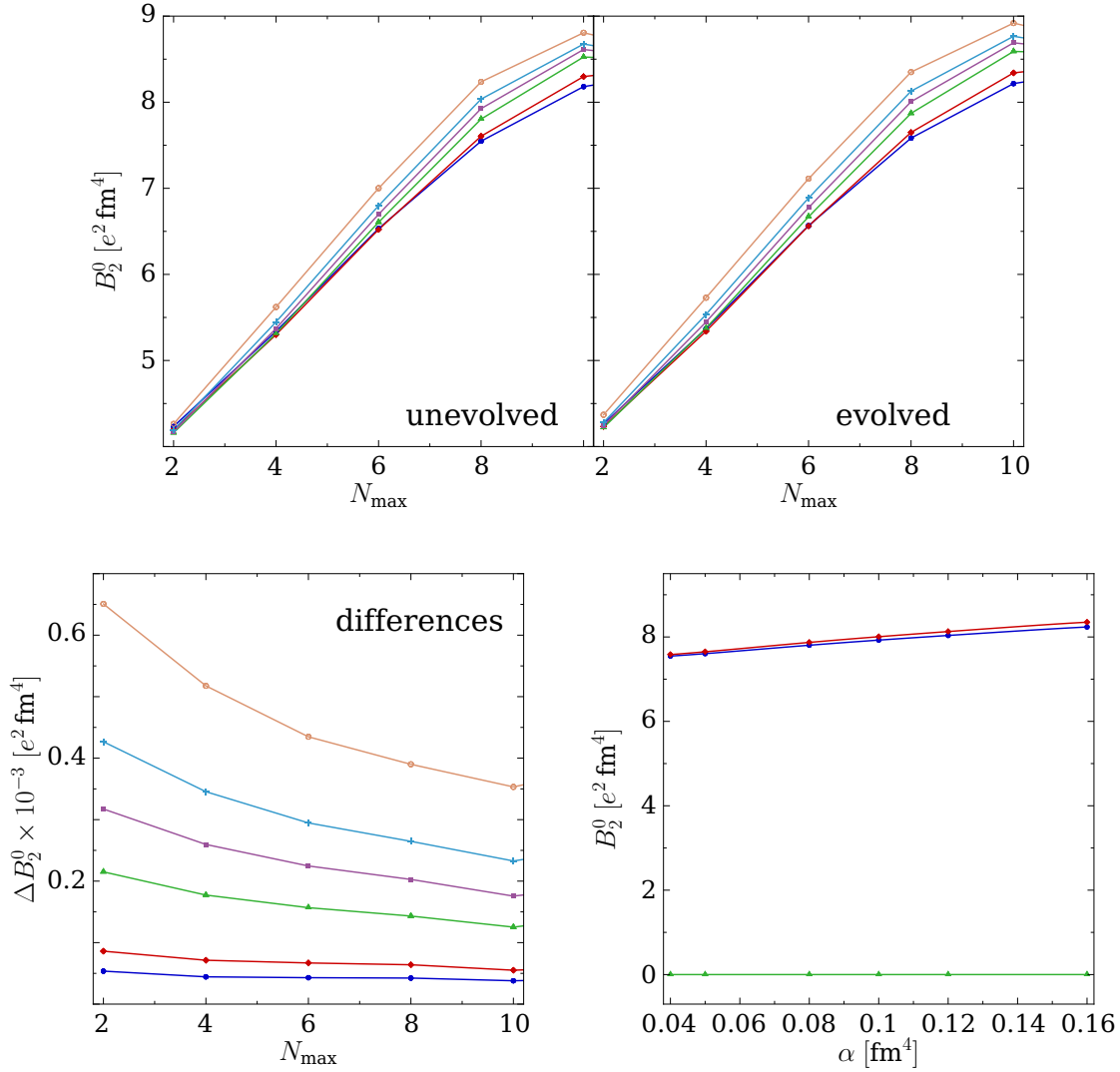


Figure 5.21: NCSM results for isoscalar quadrupole transition strength in dependency of the model-space size for the ${}^6\text{Li}$ nucleus for unevolved and SRG-evolved quadrupole operators, as well as the differences of the evolved and the unevolved transition strength, with $\alpha = 0.04 \text{ fm}^4$ (●), $\alpha = 0.05 \text{ fm}^4$ (◆), $\alpha = 0.08 \text{ fm}^4$ (▲), $\alpha = 0.1 \text{ fm}^4$ (■), $\alpha = 0.12 \text{ fm}^4$ (+), $\alpha = 0.16 \text{ fm}^4$ (○). And dependency on the flow parameter for the unevolved (●) and evolved (◆) transition strength as well as the differences (▲) at $N_{\text{max}} = 8$ (lower right).

of the strength, the more, the larger the flow parameter. The differences of the evolved and unevolved strengths show a dependency on N_{max} , where the differences become smaller for fixed flow parameter and increasing N_{max} because increasing the model-space size leads to a better description in the NCSM. In general the effect of the unitary transformation is very small, much smaller than the effects observed in the RPA calculations for the nuclei considered in that case.

5.3. MULTIPOLE TRANSITION OPERATORS

The strength as function of the flow parameter is shown in Figure 5.21 for $N_{\max} = 8$, for the bare and the evolved transition strength and their differences. One observes a very small effect of the transformation which is nearly constant in that range of the flow parameter.

Chapter 6

Conclusions

The Unitary Correlation Operator Method (UCOM) and the Similarity Renormalization Group (SRG) are two methods to explicitly treat short-range correlations generated by chiral as well as realistic potentials. The effects of these transformations have been investigated by performing many-body calculations like Hartree-Fock and No-Core Shell Model (NCSM) with the resulting interactions.

Both, the UCOM and the SRG approach are based on a unitary transformation of an initial nucleon-nucleon potential leading to effective interactions which show several similarities in momentum-space. Conceptually these two methods are designed completely differently. While the UCOM introduces central and tensor correlation functions that are constructed explicitly, the SRG is based on a renormalization group flow-equation. Considering the initial SRG flow-equation, a generator leading to a band-diagonalization of the interaction in momentum-space has the same structure as the UCOM generators.

UCOM correlation functions can be obtained either by extracting them from SRG calculations or via an explicit parameterization. The SRG-generated UCOM correlation functions show structures that are not described by the previous parameterizations. In addition, for the N3LO and the N3LOS potential, strong long-range oscillations appear which are manifested in the deuteron wave-functions. New choices of parameterizations of the UCOM correlation functions, containing a cosine-function, allow to mimic these structures which are characteristic for the SRG-generated correlation functions. The adapted parameterizations as well as the SRG-generated UCOM correlation functions lead to improved convergence in NCSM calculations for the Argonne V18 potential. In case of the N3LO potential a treatment via UCOM was not possible with the standard parameterizations for the correlation functions. Using the SRG-generated or the cosine-parameterized correlation functions, NCSM calculations converge faster, i.e., the difference between the minimum of the $N_{\max} = 0$ curve and the converged energy is smaller in that case. Nevertheless, for the Argonne V18 as well as for the N3LO potential, the use of the correlation functions obtained with the cosine-parameterized correlation functions leads to a two-minimum structure in the NCSM results. Here structures of the interaction are resolved for large model-spaces.

Hartree-Fock calculations of interactions obtained with all different types of UCOM correlation functions lead to reasonable results.

The standard SRG generator contains a commutator of the relative kinetic energy and the evolved Hamiltonian. It leads to a band-diagonalization of the momentum-space matrix-elements. To investigate this and the effect of induced many-body contributions, the generator can be adapted to leave the low-momentum region as little affected as possible. The resulting matrix-elements of the so called Λ -SRG transformation in the 1S_0 channel show, that the effect on the low-momentum matrix-elements is weaker than in the case of the SRG transformation. But the matrix-elements for large momentum differences obtained with Λ -SRG are changed too. The evolution leads to a slower diagonalization in comparison to the SRG calculations. The deuteron wave-function confirms that the attraction in the low-momentum region is controlled by the tensor correlations, because for Λ -SRG calculations the D-wave does not change much in comparison to the D-wave of unevolved interaction. The S-wave, in contrast, shows a shift of the maximum of the wave functions towards smaller distances. The correlation hole is reduced the more, the smaller the scale parameter of the Λ -SRG is chosen. NCSM calculations with the Λ -SRG interaction lead to worse convergence than when using the standard SRG. Additionally, the binding energy increases in comparison to the SRG case and the minimum is shifted towards larger oscillator frequencies. Investigation of the minimum energy as a function of the flow parameter for different values of the Λ -SRG scale parameter shows a strong dependence on the flow parameter. In Hartree-Fock calculations the binding energies mimic the structure of the experimental values, but for heavier nuclei they become smaller for increasing scale parameter. The observed effects in the many-body calculations are caused by large induced many-body forces which are neglected in the calculations which are restricted at the two-body level.

The SRG generator contains the square of the momentum operator which leads to a decoupling of long- and short-range correlations. In general any function of the momentum operator should have the same effect. A test using the momentum operator and the momentum operator to the third power, shows that the momentum-space matrix-elements in the 1S_0 channel behave similarly for all different powers of momentum in the generator. It shows, that with increasing power the diagonalization of the matrix becomes a bit slower, but the general structure of the matrix is the same. This is also benchmarked in the deuteron wave-function. The wave-functions have a similar shape and do not deviate much for a fixed flow parameter. For decreasing power of momentum the reduction of the correlation hole and of the D-wave admixture becomes a bit more pronounced. Investigations in the NCSM show that the convergence behaviour is improved a little bit for decreasing power of momentum. The energy as a function of the flow parameter shows, that all three generators lead to similar results, where the minima of the curves is shifted towards larger flow parameters for increasing power of momentum in the generator.

The decoupling of long- and short-range correlations as well as the impact of many-body contributions has to be investigated by applying the unitary SRG or UCOM transformation to other observables than the Hamiltonian for consistency. Both methods

are constructed such, that they allow to consistently transform any observable. A possible choice for an other observable is the radius operator which is long-ranged and one expects only small changes when applying the unitary transformations on it. Hartree-Fock calculations with the SRG-transformed rms-radii show only small deviations of the transformed and untransformed charge radii for flow parameters in the relevant region. Larger values of the flow parameter lead to smaller charge radii when performing the SRG transformation compared to the untransformed radii. The UCOM transformation of the rms-radii leads to very small deviations from the untransformed radii, as well.

NCSM calculations with the SRG-evolved radii show similar results as the Hartree-Fock method. The unitary transformation leads to slightly smaller values for the rms-radii and the deviation of the transformed and untransformed radii increases with increasing flow parameter.

The monopole and quadrupole operators are, like the radius operator, long-ranged operators. Calculations of the monopole transition strengths via the random phase approximation for a set of nuclei in various mass regions show, that the SRG transformation has an effect of 5% for ^{40}Ca to about 30% for ^{90}Zr , for the largest considered flow parameter. For flow parameters in the relevant region the effect of the transformation of the monopole operator is about 5% and generally increases with increasing mass number. In case of the quadrupole the transformation with a flow parameter in the relevant region does not lead to changes larger than 1%. In case of the UCOM transformation of the monopole operator, the effect of the transformation is much smaller than within the SRG transformation. NCSM calculations with SRG-evolved quadrupole operators for the transition from the 3^+ to the 1^+ state of the ^6Li nucleus lead to comparable results and the effect of the unitary transformation is very small in comparison to the absolute value of the transition strength.

For further studies on the UCOM transformed Hamiltonians the inclusion of three-nucleon forces is inevitable. A discussion of phenomenological three-body forces is given in [47] for the Argonne V18 potential, a consistent treatment of two- and three-nucleon interactions from chiral interactions is desirable. In the SRG scheme this step has been applied successfully [73, 74] and SRG transformations with consistent two-plus three-body interactions with the generators used in this thesis will give further insight into short-range correlations and the effect of induced many-body forces in the SRG.

In this work, we have discussed the derivation of effective Hamiltonians and consistent effective operators in the UCOM and SRG approaches. While the transformations can be visualized rather straightforwardly, it is worthwhile to seek further insight by investigating other quantities. The many-body coordinate space densities seem particularly suited for extracting information about the short-range correlations directly. The two-body density can be used to visualize the effect of the correlations directly. To include the density in the existing code, the harmonic oscillator representation is needed, which is given in Appendix C. For consistency also observables like dipole and Gamow-Teller transition operators can be transformed by means of the SRG or UCOM

approaches. The unitary transformation of the Gamow-Teller operator is of special interest to investigate if it has an effect on the quenching, i.e., the fact that only about 60% of the theoretical predicted transition strength has been observed in experiment [75]. In this context the inclusion of three-nucleon forces will also be important, because the radii, for example, show a dependence on the flow parameter and this effect should be corrected for with the inclusion of induced many-body interactions.

Appendix A

The Hartree-Fock Method

The Hartree-Fock method is a many-body method based on the Ritz variational principle. It provides an approximation for the solution of the full many-body problem.

A.1 The Variational Principle

The Ritz variational principle [76, 23] states that the solution of the Schrödinger equation

$$H|\Psi\rangle = E|\Psi\rangle \quad (\text{A.1})$$

is equivalent to the variation

$$\delta E[|\Psi\rangle] = E[|\Psi\rangle + |\delta\Psi\rangle] - E[|\Psi\rangle] = 0, \quad (\text{A.2})$$

provided we work in a complete many-body Hilbert space.

Here the energy is assumed to be a functional of the states $|\Psi\rangle$:

$$E[|\Psi\rangle] = \frac{\langle\Psi|H|\Psi\rangle}{\langle\Psi|\Psi\rangle}. \quad (\text{A.3})$$

Assuming an arbitrary but infinitesimal variation $|\delta\Psi\rangle$ of the state $|\Psi\rangle$, with $\langle\delta\Psi|\delta\Psi\rangle \ll 1$, the variation of the energy functional is given by

$$\delta E[|\Psi\rangle] = \frac{1}{\langle\Psi|\Psi\rangle} \left[\langle\delta\Psi|H|\Psi\rangle + \langle\Psi|H|\delta\Psi\rangle - \frac{\langle\Psi|H|\Psi\rangle}{\langle\Psi|\Psi\rangle} (\langle\delta\Psi|\Psi\rangle + \langle\Psi|\delta\Psi\rangle) \right], \quad (\text{A.4})$$

where higher orders in $|\delta\Psi\rangle$ were discarded, and the stationarity condition leads to

$$\langle \delta\Psi | (H - E) | \Psi \rangle + \langle \Psi | (H - E) | \delta\Psi \rangle = 0. \quad (\text{A.5})$$

Since the variation is arbitrary, we can also consider variations of the type $|\Psi\rangle + i|\delta\Psi\rangle$, and we obtain

$$-i\langle \delta\Psi | (H - E) | \Psi \rangle + i\langle \Psi | (H - E) | \delta\Psi \rangle = 0. \quad (\text{A.6})$$

Combining these two equations leads to the equation

$$\langle \delta\Psi | (H - E) | \Psi \rangle = 0, \quad (\text{A.7})$$

which is equivalent to the stationary Schrödinger equation due to the arbitrariness of the state $|\delta\Psi\rangle$.

The variational principle is used to find approximate solutions of the eigenvalue problem. For that purpose trial states are chosen which cover a subspace instead of the whole Hilbert space. If the exact energy eigenvalue is contained in this subspace, the exact solution of the eigenvalue problem is obtained, otherwise only an approximation.

This method is especially appropriate for the determination of ground-state energies, because it can be shown that the energy expectation value $E[|\Psi\rangle]$ of an arbitrary trial state $|\Psi\rangle$ is greater or equal to the exact value for the ground-state energy E_0 [23]:

$$E[|\Psi\rangle] \geq E_0. \quad (\text{A.8})$$

A.2 The Hartree-Fock Equations

For the description of a system of A fermions the Hartree-Fock trial state is a single Slater determinant

$$|\Phi\rangle = a_1^\dagger a_2^\dagger \dots a_A^\dagger |0\rangle = |\alpha_1 \dots \alpha_A\rangle_a, \quad (\text{A.9})$$

where the subscript indicates antisymmetrization of the state.

The minimal energy expectation value $E[|\Phi\rangle]$ is obtained by the variation of the single-particle states $|\alpha_i\rangle = a_i^\dagger |0\rangle$. A configuration space basis $\{|\chi_k\rangle\}$, where $|\chi_k\rangle = c_k^\dagger |0\rangle$, is chosen in which the states $|\alpha_i\rangle$ are expanded:

$$|\alpha_i\rangle = \sum_k C_{ik} |\chi_k\rangle \quad \text{and} \quad a_i^\dagger = \sum_k C_{ik} c_k^\dagger. \quad (\text{A.10})$$

Here the expansion coefficients C_{ik} have to be determined. Slater determinants are invariant under unitary transformations of the occupied single-particle states. Thus, the Slater determinant is described by a projection on a subspace in the single-particle

space by a projection operator ρ . The matrix-elements of this operator, expressed in terms of the coefficients C_{ik} , define the single-particle density matrix

$$\rho_{kk'}^{(1)} = \langle \Phi | c_{k'}^\dagger c_k | \Phi \rangle = \sum_{j,j'} C_{j'k'}^* C_{jk} \langle \Phi | a_{j'}^\dagger a_j | \Phi \rangle = \sum_j^A C_{jk'}^* C_{jk}. \quad (\text{A.11})$$

The density matrix of a Slater determinant is hermitian

$$\left((\rho^{(1)})_{k'k}^* = \rho_{kk'}^{(1)} \right) \quad (\text{A.12})$$

and idempotent

$$\left(\sum_l \rho_{kl}^{(1)} \rho_{lk'}^{(1)} = \rho_{kk'}^{(1)} \right). \quad (\text{A.13})$$

The Hamiltonian in the basis $|\chi_k\rangle$ is given by

$$H = \sum_{k_1, k_2} T_{k_1, k_2} c_{k_1}^\dagger c_{k_2} + \frac{1}{4} \sum_{k_1, k_2, k_3, k_4} V_{k_1 k_2, k_3 k_4} c_{k_1}^\dagger c_{k_2}^\dagger c_{k_4} c_{k_3}, \quad (\text{A.14})$$

with the single-particle kinetic energy matrix-elements $T_{k_1, k_2} = \langle \chi_{k_1} | T | \chi_{k_2} \rangle$ and the two-body matrix-elements of the interaction between the nucleons $V_{k_1 k_2, k_3 k_4} = {}_a \langle \chi_{k_1} \chi_{k_2} | V | \chi_{k_3} \chi_{k_4} \rangle_a$. Thus, the energy expectation value reads

$$\begin{aligned} E[|\Phi\rangle] &= \langle \Phi | H | \Phi \rangle = \sum_{k_1, k_2} T_{k_1, k_2} \langle \Phi | c_{k_1}^\dagger c_{k_2} | \Phi \rangle \\ &\quad + \frac{1}{4} \sum_{k_1, k_2, k_3, k_4} V_{k_1 k_2, k_3 k_4} \langle \Phi | c_{k_1}^\dagger c_{k_2}^\dagger c_{k_4} c_{k_3} | \Phi \rangle. \end{aligned} \quad (\text{A.15})$$

The expectation values of the annihilation and creation operators are the single-particle density matrix $\rho_{k_2, k_1}^{(1)}$ and the two-body density matrix. One then obtains

$$\rho_{k_3 k_4, k_1 k_2}^{(2)} = \rho_{k_3, k_1}^{(1)} \rho_{k_4, k_2}^{(1)} - \rho_{k_3, k_2}^{(1)} \rho_{k_4, k_1}^{(1)}. \quad (\text{A.16})$$

This can be expressed in terms of single-particle density matrices because the state $|\Phi\rangle$ is a Slater determinant, the energy can be expressed as

$$E[\rho] = \sum_{k_1, k_3} T_{k_1, k_3} \rho_{k_3, k_1}^{(1)} + \frac{1}{2} \sum_{k_1, k_2, k_3, k_4} \rho_{k_3, k_1}^{(1)} V_{k_1 k_2, k_3 k_4} \rho_{k_4, k_2}^{(1)}. \quad (\text{A.17})$$

The variation of the energy functional is given by

$$\delta E[\rho^{(1)}] = \sum_{k_1, k_3} T_{k_1, k_3} \delta \rho_{k_3, k_1}^{(1)} + \sum_{k_1, k_2, k_3, k_4} \delta \rho_{k_3, k_1}^{(1)} V_{k_1 k_2, k_3 k_4} \rho_{k_4, k_2}^{(1)}, \quad (\text{A.18})$$

where only linear terms in $\delta \rho^{(1)}$ are taken into account. Introducing a single-particle Hamiltonian consisting of the kinetic energy and the density matrix-dependent potential,

$$H_{k_1, k_3}[\rho^{(1)}] = T_{k_1, k_3} + \sum_{k_1, k_2, k_3, k_4} V_{k_1 k_2, k_3 k_4} \rho_{k_4, k_2}^{(1)}, \quad (\text{A.19})$$

the variational equation can be written as

$$\delta E[\rho^{(1)}] = \sum_{i_1, i_3} H_{i_1, i_3}[\rho^{(1)}] \delta \rho_{i_1, i_3}^{(1)} = 0. \quad (\text{A.20})$$

The variation of the density matrix is constrained to stay in the space of Slater determinants, i.e., it must preserve idempotency. This implies

$$(\rho + \delta \rho)^2 = \rho + \delta \rho \quad \Rightarrow \quad \rho \delta \rho + \delta \rho \rho = \delta \rho, \quad (\text{A.21})$$

or in terms of matrix-elements:

$$\sum_l \rho_{kl} \delta \rho_{lk'} + \delta \rho_{kl} \rho_{lk'} = \delta \rho_{kk'}. \quad (\text{A.22})$$

This is a strong constraint on the variation $\delta \rho$ which can be seen by evaluating the density matrix in the Hartree-Fock basis, where $\rho_{kk'}$ is diagonal:

$$\rho_{kk'} = n_k \delta_{kk'}, \quad n_k = \begin{cases} 1 & \varepsilon_k \leq \varepsilon_F, \\ 0 & \varepsilon_k > \varepsilon_F. \end{cases} \quad (\text{A.23})$$

Here n_k is the occupation number, where we refers to occupied states (above the fermi energy ε_F) and hole states (below ε_F). Equation (A.2) now reads

$$(n_k + n_{k'}) \delta \rho_{kk'} = \delta \rho_{kk'}. \quad (\text{A.24})$$

It can only be satisfied if k is a particle and k' a hole index, or vice versa, i.e., variations are restricted to the particle-hole matrix-elements of the density matrix, otherwise the space of Slater determinants will be exceeded. To guarantee that the stationarity condition (A.20) is satisfied for such variations, the particle-hole matrix-elements of $H[\rho]$ must vanish, i.e., it has the same block structure as ρ in the Hartree-Fock representation. Due to equation (A.20,) the single-particle Hamiltonian consists of non-vanishing particle-particle and hole-hole matrix-elements in Hartree-Fock basis, i.e. the commu-

tator of the single-particle Hamiltonian and the single-particle density has to vanish:

$$[h[\rho^{(1)}], \rho^{(1)}] = 0. \quad (\text{A.25})$$

This relation can be converted into a single-particle eigenvalue problem

$$h[\rho^{(1)}] |\alpha_i\rangle = \epsilon_i |\alpha_i\rangle, \quad (\text{A.26})$$

where $|\alpha_i\rangle$ are the Hartree-Fock eigenstates and ϵ_i the corresponding Hartree-Fock single-particle energies. Expanding equation (A.26) in the basis $|\chi_k\rangle$ gives

$$\sum_{k_3} h_{k_1, k_3} [\rho^{(1)}] C_{ik_3} = \epsilon_i C_{ik_1}. \quad (\text{A.27})$$

Inserting the explicit form of the Hamiltonian (equation (A.19)) and the single-particle density (equation (A.11)), the Hartree-Fock equations read

$$\sum_{k_3} \left(t_{k_1, k_3} + \sum_{k_2, k_4} \sum_{i'=1}^A v_{k_1 k_2, k_3 k_4} C_{i' k_2} C_{i' k_4} \right) C_{ik_3} = \epsilon_i C_{ik_1}. \quad (\text{A.28})$$

This is a set of non-linear equations for the single-particle energies ϵ_i and the expansion coefficients C_{ik} . It has to be solved in an iterative scheme to obtain self-consistent solutions for the expansion coefficients.

The Hartree-Fock ground-state is a Slater determinant

$$|\text{HF}\rangle = |\Phi\rangle = a_1^\dagger a_2^\dagger \dots a_A^\dagger |0\rangle, \quad (\text{A.29})$$

constructed of the A single-particle states with the lowest energies. Its energy expectation value is

$$E[|\text{HF}\rangle] = \langle \text{HF} | h | \text{HF} \rangle \quad (\text{A.30})$$

$$= \sum_{i=1}^A \langle \alpha_i | t | \alpha_i \rangle + \frac{1}{2} \sum_{i, i'=1}^A a \langle \alpha_i \alpha_{i'} | v | \alpha_i \alpha_{i'} \rangle_a \quad (\text{A.31})$$

$$= \sum_{i=1}^A \epsilon_i - \frac{1}{2} \sum_{i, i'=1}^A a \langle \alpha_i \alpha_{i'} | v | \alpha_i \alpha_{i'} \rangle_a. \quad (\text{A.32})$$

This shows that the ground-state energy is not equal to the sum of the single-particle energies.

A.3 Hartree-Fock for Interactions in Matricelement Representation

The Hamiltonian entering the Hartree-Fock equations consist of the kinetic energy T and the transformed interactions V_{NN} :

$$H_{\text{int}} = T - T_{\text{cm}} + V_{NN} = T_{\text{int}} + V_{NN} . \quad (\text{A.33})$$

The center-of-mass part of the kinetic energy T_{cm} is subtracted from the kinetic energy leading to the intrinsic kinetic energy T_{int} , which can be written as a pure two-body operator

$$T_{\text{int}} = T - T_{\text{cm}} = \frac{2}{A\mu} \sum_{i<j}^A \mathbf{q}_{ij}^2 , \quad (\text{A.34})$$

where \mathbf{q} is the relative two-body momentum.

The eigenstates $|nljmm_t\rangle$ of the spherical harmonic oscillator are chosen as basis states and used to expand the Hartree-Fock single-particle states:

$$|\nu l j m m_t\rangle = \sum_n C_n^{(\nu l j m m_t)} |nljmm_t\rangle . \quad (\text{A.35})$$

Here n is the radial quantum number, l the orbital angular momentum, j the total angular momentum with projection m and m_t the isospin projection. Assuming spherical symmetry, only states with the same l and j quantum numbers can contribute in the Hartree-Fock expansion, and the expansion coefficients are independent of m ($C_n^{(\nu l j m m_t)} = C_n^{(\nu l j m_t)}$). As already mentioned in the former section, these coefficients are used as variational parameters for the minimization of the energy expectation value.

In this basis the Hartree-Fock equation can be written as

$$\sum_{\bar{n}} h_{n\bar{n}}^{ljm_t} C_{\bar{n}}^{(\nu l j m_t)} = \epsilon^{(\nu l j m_t)} C_{\bar{n}}^{(\nu l j m_t)} , \quad (\text{A.36})$$

with the single-particle energies $\epsilon^{(\nu l j m_t)}$. The matrix-elements of the single-particle Hamiltonian are

$$h_{n\bar{n}}^{ljm_t} = \sum_{l',j',m'_t} \sum_{n',\bar{n}'} H_{nn',\bar{n}\bar{n}'}^{(ljm_t,l'j'm'_t)} \rho_{n',\bar{n}'}^{(l'j'm'_t)} , \quad (\text{A.37})$$

with the single-particle density matrix

$$\rho_{n',\bar{n}'}^{(l'j'm'_t)} = \sum_{\nu} (2j+1) C_{\bar{n}}^{(\nu l j m_t)*} C_n^{(\nu l j m_t)}. \quad (\text{A.38})$$

Due to spherical symmetry, we can average over the m quantum numbers, and express the antisymmetrized matrix-elements of the Hamiltonian as [20]

$$H_{nn',\bar{n},\bar{n}'}^{(ljm_t,l'j'm'_t)} = \frac{1}{(2j+1)(2j'+1)} \sum_{m,m'} \langle nljmm_t, n'l'j'm'_t | H_{\text{int}} | \bar{n}ljmm_t, \bar{n}'l'j'm'_t \rangle. \quad (\text{A.39})$$

Coupling the single-particle angular momenta and carrying out the summations over magnetic quantum numbers, we obtain

$$H_{nn',\bar{n},\bar{n}'}^{(ljm_t,l'j'm'_t)} = \sum_{J,M_T} \frac{(2J+1)}{(2j+1)(2j'+1)} c \left(\begin{array}{cc} \frac{1}{2} & \frac{1}{2} \\ m_t & m'_t \end{array} \middle| \begin{array}{c} T \\ M_T \end{array} \right)^2 \quad (\text{A.40})$$

$$\times \langle nlj, n'l'j'; JTM_T | H_{\text{int}} | \bar{n}lj, \bar{n}'l'j'; JTM_T \rangle,$$

where $c \left(\begin{array}{cc} \frac{1}{2} & \frac{1}{2} \\ m_t & m'_t \end{array} \middle| \begin{array}{c} T \\ M_T \end{array} \right)$ is a Clebsch-Gordan coefficient.

In general the matrix-elements of the effective interactions are calculated in a relative LS -basis and have to be transformed to the single-particle jj -coupled basis using Talmi-Moshinsky brackets (see [20] and references therein for details).

Appendix B

The Random Phase Approximation

The Random Phase Approximation (RPA) is the simplest approach for investigations of collective excitations of a mean-field state. RPA can be derived as a harmonic approximation for a time-dependent mean-field theory, i.e., time-dependent Hartree-Fock [23]. Another possibility presented here is the Equation-of-Motion (EoM) method. This method avoids the explicit calculations of the ground-state which is very complicated and gives it in an implicit form [24, 22, 23, 77].

B.1 Equations of Motion

The exact Schrödinger equation

$$H |\Psi_\nu\rangle = E_\nu |\Psi_\nu\rangle \quad (\text{B.1})$$

can be rewritten by introducing excitations operators

$$|\Psi_\nu\rangle = Q_\nu^\dagger |\Psi_0\rangle \quad \text{and} \quad Q_\nu |\Psi_0\rangle = 0, \quad (\text{B.2})$$

where

$$Q_\nu^\dagger = |\Psi_\nu\rangle\langle\Psi_0| \quad \text{and} \quad Q_\nu = |\Psi_0\rangle\langle\Psi_\nu|. \quad (\text{B.3})$$

We obtain the EoM

$$[H, Q_\nu^\dagger] |\Psi_0\rangle = (E_\nu - E_0) Q_\nu^\dagger |\Psi_0\rangle. \quad (\text{B.4})$$

Multiplying this equation with an arbitrary state $\langle\Psi_0|\delta Q$ and inserting additional

terms of the form $\langle \Psi_0 | Q_\nu^\dagger = \langle \Psi_0 | H Q_\nu^\dagger = 0$, to obtain a simplified commutator form, leads to

$$\langle \Psi_0 | [\delta Q, [H, Q_\nu^\dagger]] | \Psi_0 \rangle = (E_\nu - E_0) \langle \Psi_0 | [\delta Q, Q_\nu^\dagger] | \Psi_0 \rangle. \quad (\text{B.5})$$

This equation is exact as long as the variation

$$\delta Q^\dagger | \Psi_0 \rangle = \sum_{\nu \neq 0} \delta c_\nu Q_\nu^\dagger | \Psi_0 \rangle = \sum_{\nu \neq 0} \delta c_\nu | \Psi_\nu \rangle \quad (\text{B.6})$$

is chosen to be orthogonal to the ground-state and to cover the whole Hilbert space.

B.2 Random Phase Approximation

In the following the notation $A_{mn}^{kl} = a_k^\dagger a_l^\dagger a_n a_m$ and $A_l^k = a_k^\dagger a_l$, and normal ordering, where all internal contractions are subtracted, will be used [22]. Contractions of an upper with an lower index are defined as the one-body density matrix

$$\lambda_l^k = \langle \Psi | A_l^k | \Psi \rangle \quad (\text{B.7})$$

with the reference state $|\Psi\rangle$. In normal ordering with respect to the Hartree-Fock solution one obtains:

$$A_l^k = : A_l^k : + \lambda_l^k \quad (\text{B.8})$$

$$A_{mn}^{kl} = : A_{mn}^{kl} : + \lambda_m^k : A_n^l : - \lambda_n^k : A_m^l : + \lambda_n^l : A_m^k : - \lambda_m^l : A_n^k : + \lambda_m^k \lambda_n^l - \lambda_n^k \lambda_m^l. \quad (\text{B.9})$$

Wick's Theorem [22] is used to evaluate pairs of normal-ordered operators, i.e., this product is expanded in a sum of all externally contracted terms. The contraction between a lower and an upper index is given by

$$: A_b^a :: A_l^k := -\xi_b^k : A_l^a : + \dots, \quad (\text{B.10})$$

with

$$\xi_l^k = \lambda_l^k - \delta_l^k = -\langle \Psi | a_l a_k^\dagger | \Psi \rangle. \quad (\text{B.11})$$

In Hartree-Fock basis one obtains

$$\lambda_l^k = n_k \delta_l^k \quad (\text{B.12})$$

with the occupation number n_k defined in (A.23). Contractions between particle and

hole states must vanish and therefore the creation and annihilation operators can be replaced by their normal ordered terms:

$$a_p^\dagger a_h = : a_p^\dagger a_h : , \quad a_h^\dagger a_p = : a_h^\dagger a_p : . \quad (\text{B.13})$$

In the RPA, the excitation operators in the EoM (B.1) are approximated as 1-particle-1-hole operators

$$Q_\nu^\dagger = \sum_{m,a} X_{ma}^{(\nu)} A_a^m - \sum_{m,a} Y_{ma}^{(\nu)} A_m^a . \quad (\text{B.14})$$

In the following the indices a and b indicate states below the Fermi energy ϵ_F (holes), while m and n are used for states above the Fermi energy (particles). Here, the Fermi energy ϵ_F is given by the Hartree-Fock eigenvalue of the highest occupied single-particle state. The ground-state $|\Psi_0\rangle = |\text{RPA}\rangle$ is defined by $Q_\nu |\text{RPA}\rangle = 0$. It contains contributions from particle - hole excitations which are generated by the operator A_a^m and accordingly annihilated by A_m^a .

The forward and backward amplitudes $X_{ma}^{(\nu)}$ and $Y_{ma}^{(\nu)}$ are varied independently of each other:

$$\delta Q^\dagger |\text{RPA}\rangle = \sum_{m,a} \delta X_{ma}^{(\nu)} A_a^m |\text{RPA}\rangle - \sum_{m,a} \delta Y_{ma}^{(\nu)} A_m^a |\text{RPA}\rangle . \quad (\text{B.15})$$

This leads to a set of coupled equations:

$$\begin{aligned} \langle \text{RPA} | [A_m^a, [H, Q_\nu^\dagger]] | \text{RPA} \rangle &= E_\nu^{\text{RPA}} \langle \text{RPA} | [A_m^a, Q_\nu^\dagger] | \text{RPA} \rangle \\ \langle \text{RPA} | [A_a^m, [H, Q_\nu^\dagger]] | \text{RPA} \rangle &= E_\nu^{\text{RPA}} \langle \text{RPA} | [A_a^m, Q_\nu^\dagger] | \text{RPA} \rangle , \end{aligned} \quad (\text{B.16})$$

where $E_\nu^{\text{RPA}} = E_\nu - E_0$. These equations define the excitation operators Q_ν^\dagger through the amplitudes $X_{ma}^{(\nu)}$ and $Y_{ma}^{(\nu)}$. Since the state $|\text{RPA}\rangle$ is unknown a priori, the equations cannot be solved directly. Thus, an additional approximation is introduced: the RPA ground-state is replaced by the Hartree-Fock state in equation (B.16), and we obtain

$$\begin{aligned} \langle \text{RPA} | [A_m^a, A_b^n] | \text{RPA} \rangle &= \delta_{ab} \delta_{mn} + \delta_{mn} \langle \text{RPA} | A_b^a | \text{RPA} \rangle - \delta_{ab} \langle \text{RPA} | A_m^n | \text{RPA} \rangle \\ &\approx \langle \text{HF} | [A_m^a, A_b^n] | \text{HF} \rangle = \delta_{ab} \delta_{mn} . \end{aligned} \quad (\text{B.17})$$

This is known as the quasi-boson approximation. Within this approximation, the coefficients $X_{ma}^{(\nu)}$ and $Y_{ma}^{(\nu)}$ can be identified with the matrix-elements of the one-body transition density $\rho^{(1)}$

$$\begin{aligned}\rho_{ma}^{(1)\nu} &= \langle \text{RPA} | A_m^a | \Psi_\nu \rangle = \langle \text{RPA} | [A_m^a, Q_\nu^\dagger] | \text{RPA} \rangle \approx \langle \text{HF} | [A_m^a, Q_\nu^\dagger] | \text{HF} \rangle = X_{ma}^{(\nu)} \\ \rho_{am}^{(1)\nu} &= \langle \text{RPA} | A_a^m | \Psi_\nu \rangle = \langle \text{RPA} | [A_a^m, Q_\nu^\dagger] | \text{RPA} \rangle \approx \langle \text{HF} | [A_a^m, Q_\nu^\dagger] | \text{HF} \rangle = Y_{am}^{(\nu)}.\end{aligned}\quad (\text{B.18})$$

The absolute square of the transition density matrix gives the probability to find a state $A_m^a | \text{RPA} \rangle$ or $A_a^m | \text{RPA} \rangle$ in the excited state $|\Psi_\nu\rangle$.

In quasi-boson approximation, the RPA equations can be written as a generalized eigenvalue problem:

$$\begin{pmatrix} A & B \\ B^* & A^* \end{pmatrix} \begin{pmatrix} X^{(\nu)} \\ Y^{(\nu)} \end{pmatrix} = E_\nu^{\text{RPA}} \begin{pmatrix} 1 & 0 \\ 0 & -1 \end{pmatrix} \begin{pmatrix} X^{(\nu)} \\ Y^{(\nu)} \end{pmatrix} \quad (\text{B.19})$$

with

$$A_{ma,nb} = \langle \text{HF} | [A_m^a, [H, A_b^n]] | \text{HF} \rangle = (\epsilon_m - \epsilon_a) \delta_{mn} \delta_{ab} + V_{mb,an} \quad (\text{B.20})$$

$$B_{ma,nb} = -\langle \text{HF} | [A_m^a, [H, A_n^b]] | \text{HF} \rangle = V_{mn,ab}, \quad (\text{B.21})$$

where the $V_{mn,ab}$ are interaction matrix-elements for 2-particle 2-hole excitations. The eigenvalue problem (B.19) is non-hermitian, while the sub-matrix A is hermitian and B is symmetric. Its eigenvalues are not necessarily real since the eigenvalue problem contains the metric tensor $\begin{pmatrix} 1 & 0 \\ 0 & -1 \end{pmatrix}$. The coefficients $X_{ma}^{(\nu)}$ and $Y_{ma}^{(\nu)}$ that solve the RPA equations fulfil the orthogonality relation

$$\delta_{\nu\nu'} = \sum_{m,a} (X_{ma}^{(\nu')*} X_{ma}^{(\nu)} - Y_{ma}^{(\nu')*} Y_{ma}^{(\nu)}) \quad (\text{B.22})$$

as well as the closure relation

$$\delta_{mn} \delta_{ab} = \sum_{\nu} (X_{ma}^{(\nu)*} X_{nb}^{(\nu)} - Y_{ma}^{(\nu)*} Y_{nb}^{(\nu)}). \quad (\text{B.23})$$

The RPA ground-state given by $Q_\nu | \text{RPA} \rangle = 0$ can be constructed as

$$| \text{RPA} \rangle = N_0 \exp \left(\frac{1}{2} \sum_{m,n,a,b} Z_{ma,nb} A_a^m A_b^n \right) | \text{HF} \rangle, \quad (\text{B.24})$$

where the coefficients $Z_{ma,nb}$ are defined by

$$\sum_{ma} X_{ma}^{(\nu)} Z_{ma,nb} = Y_{nb}^{(\nu)*} \quad (\text{B.25})$$

and N_0 is a normalization constant. Thus, the RPA ground-state is a coherent state of 2-particle-2-hole states, constructed from the Hartree-Fock state in a self-consistent fashion.

The energy expectation value in the RPA ground-state in quasi-boson approximation is given by [77]

$$\langle \text{RPA} | H | \text{RPA} \rangle = \langle \text{HF} | H | \text{HF} \rangle - \sum_{\nu} E_{\nu}^{\text{RPA}} \sum_{m,a} |Y_{ma}^{(\nu)}|^2. \quad (\text{B.26})$$

Its value is always below the Hartree-Fock energy and can even be lower than the exact ground-state energy, because the approximations made for the derivation of the RPA equations are not consistent with the Ritz variational principle.

B.3 Derivation of the Two-Body Contribution to the Transition Strength

In order to derive equation (5.30) the two-body operator Q has to be inserted in the commutator of the transition amplitude (equation (5.28)) $\langle \text{HF} | [Q, Q_{\nu}^{\dagger}] | \text{HF} \rangle$. Using the tensor notation introduced in the former section one obtains:

$$\begin{aligned} \langle \text{HF} | [Q, Q_{\nu}^{\dagger}] | \text{HF} \rangle &= \frac{1}{4} \sum_{klmn} \sum_{ph} Q_{klmn} \left(X_{ph}^{(\nu)} \langle \text{HF} | [A_{mn}^{kl}, :A_h^p:] | \text{HF} \rangle \right. \\ &\quad \left. - Y_{ph}^{(\nu)} \langle \text{HF} | [A_{mn}^{kl}, :A_p^h:] | \text{HF} \rangle \right). \end{aligned} \quad (\text{B.27})$$

Evaluating the commutator of the first term in the last equation leads to

$$\begin{aligned} \langle \text{HF} | [A_{mn}^{kl}, :A_h^p:] | \text{HF} \rangle &= \langle \text{HF} | \left[:A_{mn}^{kl} : + \lambda_m^k :A_n^l : - \lambda_n^k :A_m^l : + \lambda_n^l :A_m^k : - \lambda_m^l :A_n^k : \right. \\ &\quad \left. + \lambda_m^k \lambda_n^l - \lambda_n^k \lambda_m^l, :A_h^p : \right] | \text{HF} \rangle \\ &= \langle \text{HF} | \left[\lambda_m^k :A_n^l : - \lambda_n^k :A_m^l : + \lambda_n^l :A_m^k : - \lambda_m^l :A_n^k : + \lambda_m^k \lambda_n^l - \lambda_n^k \lambda_m^l, :A_h^p : \right] | \text{HF} \rangle. \end{aligned} \quad (\text{B.28})$$

The commutator $[:A_{mn}^{kl} :, :A_h^p :]$ does not contribute because it cannot be contracted completely.

With the relation

$$\langle \text{HF} | \left[:A_l^k :, :A_b^a : \right] | \text{HF} \rangle = \lambda_b^k \delta_l^a - \lambda_l^a \delta_b^k = (n_b - n_a) \delta_l^a \delta_b^k \quad (\text{B.29})$$

B.3. DERIVATION OF THE TWO-BODY CONTRIBUTION TO THE TRANSITION STRENGTH

equation (B.28) can be simplified to

$$\begin{aligned}
\langle \text{HF} | [A_{mn}^{kl}, : A_h^p :] | \text{HF} \rangle &= \lambda_m^k (\lambda_h^l \delta_n^p - \lambda_n^p \delta_h^l) - \lambda_n^k (\lambda_h^l \delta_m^p - \lambda_m^p \delta_h^l) + \lambda_n^l (\lambda_h^k \delta_m^p - \lambda_m^p \delta_h^k) - \lambda_m^l (\lambda_h^k \delta_n^p - \lambda_n^p \delta_h^k) \\
&= \underbrace{(n_h - n_p)}_{=1} (\lambda_m^k \delta_n^p \delta_h^l - \lambda_n^k \delta_m^p \delta_h^l + \lambda_n^l \delta_m^p \delta_h^k - \lambda_m^l \delta_n^p \delta_h^k) \\
&= n_k \delta_m^k \delta_n^p \delta_h^l - n_k \delta_n^k \delta_m^p \delta_h^l + n_l \delta_n^l \delta_m^p \delta_h^k - n_l \delta_m^l \delta_n^p \delta_h^k,
\end{aligned} \tag{B.30}$$

where equation (B.12) was used in the last step. The commutator $\langle \text{HF} | [A_{mn}^{kl}, : A_p^h :] | \text{HF} \rangle$ can be evaluated analogously leading to

$$\langle \text{HF} | [A_{mn}^{kl}, : A_p^h :] | \text{HF} \rangle = -n_k \delta_m^k \delta_n^h \delta_p^l + n_k \delta_n^k \delta_m^h \delta_p^l - n_l \delta_n^l \delta_m^h \delta_p^k + n_l \delta_m^l \delta_n^h \delta_p^k. \tag{B.31}$$

With these relations the matrix-elements in equation (B.27) evaluate to

$$\begin{aligned}
\langle \text{HF} | [Q, Q_\nu^\dagger] | \text{HF} \rangle &= \frac{1}{4} \sum_{kph} \left(X_{ph}^{(\nu)} (Q_{khkp} n_k - Q_{khp k} n_k + Q_{hkp k} n_k - Q_{hkkp} n_k) \right. \\
&\quad \left. + Y_{ph}^{(\nu)} (Q_{kp kh} n_k - Q_{kph k} n_k + Q_{pk h k} n_k - Q_{pk k h} n_k) \right) \\
&= \sum_{h'ph} n_k \left(X_{ph}^{(\nu)} Q_{h' h h' p} + Y_{ph}^{(\nu)} Q_{h' p h' h} \right),
\end{aligned} \tag{B.32}$$

where h' is an additional hole-state.

The RPA phonon operators can be rewritten as

$$\begin{aligned}
\sum_{pm_p h m_h} X_{pm_p h m_h}^{(\nu)} a_{pm_p}^\dagger a_{h m_h} &= \sum_{pm_p h m_h} (-1)^{j_h + m_h} a_{pm_p}^\dagger \tilde{a}_{h - m_h} X_{pm_p h m_h}^{(\nu)} \\
&= \sum_{pm_p h m_h} \sum_{JM} (-1)^{j_h + m_h} X_{pm_p h m_h}^{(\nu)} \langle j_p m_p j_h m_{-h} | JM \rangle [a_p^\dagger \tilde{a}_{-h}]_M^J \\
&= \sum_{ph} \sum_{JM} X_{ph}^{(\nu J)} [a_p^\dagger \tilde{a}_{-h}]_M^J.
\end{aligned} \tag{B.33}$$

with $[a_p^\dagger \tilde{a}_{-h}]_M^J = \sum_{j_p j_h} (-1)^{j_h + m_h} \langle j_p m_p j_h m_{-h} | JM \rangle a_{pm_p}^\dagger \tilde{a}_{h - m_h}$, following the notation of [22]. Here $\tilde{a}_\alpha \equiv (-1)^{j_\alpha + m_\alpha} a_{\alpha - m_\alpha}$ is an annihilation operator which behaves like a spherical tensor operator of rank j_α . The reduced amplitude $X_{ph}^{(\nu J)}$ is defined via

$$X_{pm_phm_h}^{(\nu)} = \sum_{JM} (-1)^{j_h+m_h} \langle j_p m_p j_h m_{-h} | JM \rangle X_{ph}^{(\nu J)}. \quad (\text{B.34})$$

The reduced amplitude does not depend on M because of spherical symmetry. In case of the backward amplitude one obtains

$$\begin{aligned} \sum_{pm_phm_h} Y_{pm_phm_h}^{(\nu)} a_{hm_h}^\dagger a_{pm_p} &= \sum_{pm_phm_h} (-1)^{j_p+m_p} a_{hm_h}^\dagger \tilde{a}_{p-m_p} Y_{pm_phm_h}^{(\nu)} \\ &= \sum_{pm_phm_h} \sum_{JM} (-1)^{j_p+m_p} Y_{pm_phm_h}^{(\nu)} \langle j_h m_h j_p m_{-p} | JM \rangle [a_h^\dagger \tilde{a}_{-p}]_M^J \\ &= \sum_{ph} \sum_{JM} Y_{ph}^{(\nu J)} [a_h^\dagger \tilde{a}_{-p}]_M^J \end{aligned} \quad (\text{B.35})$$

with

$$Y_{pm_phm_h}^{(\nu)} = \sum_{JM} (-1)^{j_p+m_p} \langle j_h m_h j_p m_{-p} | JM \rangle Y_{ph}^{(\nu J)}. \quad (\text{B.36})$$

The matrix-elements of the forward-going part of equation (B.32), where the summation over M on the left hand side leads to a M -independent right hand side, then read

$$\begin{aligned} &\sum_{h'm_h'pm_phm_h} \sum_M X_{pm_phm_h}^{(\nu)} \langle h'm_h'hm_h | Q_M^{(J)} | h'm_h'pm_p \rangle \\ &= \sum_{h'm_h'pm_phm_h} \sum_{MJ_1M_1J_2M_2} (-1)^{j_h+m_h} \langle j_p m_p j_h m_{-h} | JM \rangle X_{ph}^{(\nu J)} \\ &\quad \langle j_h' m_h' j_h m_h | J_1 M_1 \rangle \langle j_h' m_h' j_p m_p | J_2 M_2 \rangle \langle h'h J_1 M_1 | Q_M^J | h'p J_2 M_2 \rangle \\ &= \sum_{h'm_h'pm_phm_h} \sum_{MJ_1M_1J_2M_2} (-1)^{j_h+m_h} (-1)^{J-j_p-j_h} \langle j_p - m_p j_h m_h | J - M \rangle X_{ph}^{(\nu J)} \\ &\quad \langle j_h' m_h' j_h m_h | J_1 M_1 \rangle (-1)^{j_p+m_p} \frac{\hat{J}_2}{\hat{J}_{h'}} \langle j_p - m_p J_2 M_2 | j_h' m_h' \rangle \langle h'h J_1 M_1 | Q_M^J | h'p J_2 M_2 \rangle \\ &= \sum_{h'ph} \sum_{MJ_1M_1J_2M_2} (-1)^{J-M+1} \frac{\hat{J}_2}{\hat{J}_{h'}} X_{ph}^{(\nu J)} \langle h'h J_1 M_1 | Q_M^J | h'p J_2 M_2 \rangle \\ &\quad \sum_{m_h'm_p m_h} \langle j_p - m_p j_h m_h | J - M \rangle \langle j_h' m_h' j_h m_h | J_1 M_1 \rangle \langle j_p - m_p J_2 M_2 | j_h' m_h' \rangle \\ &\stackrel{[78]}{=} \sum_{h'ph} \sum_{MJ_1M_1J_2M_2} (-1)^{J-M+1} \frac{\hat{J}_2}{\hat{J}_{h'}} X_{ph}^{(\nu J)} \langle h'h J_1 M_1 | Q_M^J | h'p J_2 M_2 \rangle \\ &\quad (-1)^{j_h+J+j_h'+J_2} \hat{J}_{h'} \langle J - M J_2 M_2 | J_1 M_1 \rangle \left\{ \begin{matrix} j_p & j_h & J \\ J_1 & J_2 & j_{h'} \end{matrix} \right\} \end{aligned} \quad (\text{B.37})$$

B.3. DERIVATION OF THE TWO-BODY CONTRIBUTION TO THE TRANSITION STRENGTH

$$\begin{aligned}
&= \sum_{h'ph} \sum_{MJ_1M_1J_2M_2} (-1)^{1-M+j_h+j_{h'}+J_2} \hat{J}_2 \hat{J} X_{ph}^{(\nu J)} \langle h'hJ_1M_1 | Q_M^J | h'pJ_2M_2 \rangle \\
&\quad \langle J - MJ_2M_2 | J_1M_1 \rangle \left\{ \begin{matrix} j_p & j_h & J \\ J_1 & J_2 & j_{h'} \end{matrix} \right\}. \tag{B.38}
\end{aligned}$$

Here the abbreviation $\hat{J} = \sqrt{2J+1}$ is used and in (B.37) the relation $(-1)^{m_p+m_h} = (-1)^{2m_p-m_p+m_h} = (-1)^{1-M}$ which can be written in that form because the m quantum numbers are half-integers.

The backward-going contribution to the matrix-elements can be evaluated analogously and we obtain

$$\begin{aligned}
&\sum_{h'm_{h'}pm_phm_h} \sum_M Y_{pm_phm_h}^{(\nu)} \langle h'm_{h'}pm_p | Q_M^{(J)} | h'm_{h'}hm_h \rangle \\
&= \sum_{h'ph} \sum_{MJ_1M_1J_2M_2} (-1)^{1-M+j_p+j_{h'}+J_2} \hat{J}_2 \hat{J} Y_{ph}^{(\nu J)} \langle h'pJ_1M_1 | Q_M^J | h'pJ_2M_2 \rangle \\
&\quad \langle J - MJ_2M_2 | J_1M_1 \rangle \left\{ \begin{matrix} j_h & j_p & J \\ J_1 & J_2 & j_{h'} \end{matrix} \right\}. \tag{B.39}
\end{aligned}$$

Using the Wigner-Eckart theorem [22] the matrix-elements of the transition operator can be rewritten as

$$\langle h'pJ_1M_1 | Q_M^J | h'pJ_2M_2 \rangle = \hat{J}_1^{-1} \langle J_2M_2JM | J_1M_1 \rangle \langle h'hJ_1 || Q^J || h'pJ_2 \rangle. \tag{B.40}$$

The Clebsch-Gordan coefficients in (B.38) and (B.40) can be rewritten as

$$\begin{aligned}
&\langle J_2M_2JM | J_1M_1 \rangle \langle J - MJ_2M_2 | J_1M_1 \rangle \\
&= (-1)^{J_1+J_2-J} \frac{\hat{J}_1^2}{\hat{J}_2} \langle J_1M_1J_2 - M_2 | JM \rangle \langle J_1M_1J_2 - M_2 | J - M \rangle. \tag{B.41}
\end{aligned}$$

Carrying out the summation over M_1 and M_2 leads to

$$\sum_{M_1M_2} \langle J_1M_1J_2 - M_2 | JM \rangle \langle J_1M_1J_2 - M_2 | J - M \rangle = \delta_{JJ} \delta_{M,-M} = \delta_{M,0}. \tag{B.42}$$

Using all the previous steps one obtains for the forward part of the matrix-elements

$$\begin{aligned}
 & \sum_{h'm_{h'}pm_phm_h} \sum_M X_{pm_phm_h}^{(\nu)} \langle h'm_{h'}hm_h | Q_M^{(J)} | h'm_{h'}pm_p \rangle \\
 &= \sum_{h'ph} \sum_{J_1 J_2} (-1)^{1+j_h+j_{h'}+J_1-J} \frac{\hat{J}_1 \hat{J}_2}{\hat{J}} X_{ph}^{(\nu J)} \left\{ \begin{matrix} j_p & j_h & J \\ J_1 & J_2 & j_{h'} \end{matrix} \right\} \langle h'hJ_1 || Q^J || h'pJ_2 \rangle. \quad (\text{B.43})
 \end{aligned}$$

In case of the backward component of the matrix-elements we have

$$\begin{aligned}
 & \sum_{h'm_{h'}pm_phm_h} \sum_M Y_{pm_phm_h}^{(\nu)} \langle h'm_{h'}pm_p | Q_M^{(J)} | h'm_{h'}hm_h \rangle \\
 &= \sum_{h'ph} \sum_{J_1 J_2} (-1)^{1+j_p+j_{h'}+J_1-J} \frac{\hat{J}_1 \hat{J}_2}{\hat{J}} Y_{ph}^{(\nu J)} \left\{ \begin{matrix} j_h & j_p & J \\ J_1 & J_2 & j_{h'} \end{matrix} \right\} \langle h'pJ_1 || Q^J || h'hJ_2 \rangle. \quad (\text{B.44})
 \end{aligned}$$

Renaming J_1 and J_2 in equation (B.44) and using the symmetry of the $6j$ -symbol which is invariant under arbitrary permutations of the columns, the two-body contribution to the transition operator (5.30) is obtained:

$$\begin{aligned}
 \sum_M \langle \text{HF} | [Q_{JM}^T]^{[2]}, Q_\omega^\dagger | \text{HF} \rangle &= \sum_{phh'J_1J_2} (-1)^{1-J+j_{h'}} \frac{\hat{J}_1 \hat{J}_2}{\hat{J}} \left\{ \begin{matrix} j_p & j_h & J \\ J_1 & J_2 & j_{h'} \end{matrix} \right\} \\
 &\quad \left[(-1)^{j_h+J_1} \langle h'hJ_1 || [Q_J^T]^{[2]} || h'pJ_2 \rangle X_{ph}^{(\nu,J)} \right. \\
 &\quad \left. + (-1)^{j_p+J_2} \langle h'pJ_1 || [Q_J^T]^{[2]} || h'hJ_2 \rangle Y_{ph}^{(\nu,J)} \right]. \quad (\text{B.45})
 \end{aligned}$$

B.3. DERIVATION OF THE TWO-BODY CONTRIBUTION TO THE TRANSITION STRENGTH

Appendix C

Unitary Transformed Densities

C.1 Motivation

The unitary transformation of the density operator should give insight into the effects of the different treatment of short-range correlations by SRG and UCOM transformations. The unitary operators are chosen in an analogous way as for the transition operators discussed in Chapter 5. Again, the unitary operator is represented by the correlation operators $C_r C_\Omega$ in case of the UCOM and U_α for the SRG transformation, respectively:

$$U = \begin{cases} C_r C_\Omega & \text{UCOM} \\ U_\alpha & \text{SRG} \end{cases} \quad (\text{C.1})$$

C.1.1 Two-Body Density in Harmonic Oscillator Basis

The unitary operators used for the transformation are given in harmonic oscillator representation. Therefore it is sensible to calculate the transformed density in that basis and transform to coordinate or momentum representation afterwards.

The two-body density operator in harmonic oscillator representation in second quantized form is defined as

$$R(n_1 n_2, n'_1 n'_2) = c_{n_1}^\dagger c_{n_2}^\dagger c_{n'_2} c_{n'_1}, \quad (\text{C.2})$$

with the operators $c_{n_i}^\dagger$ creating a particle in oscillator state n_i and c_{n_j} annihilating a particle in state n_j . The matrix elements in harmonic oscillator basis $\{|\alpha\rangle\}$ are then given by

$$\langle \bar{\alpha}_1 \bar{\alpha}_2 | R(n_1 n_2, n'_1 n'_2) | \bar{\alpha}_1 \bar{\alpha}_2 \rangle = {}_a \langle \bar{\alpha}_1 \bar{\alpha}_2 | c_{n_1}^\dagger c_{n_2}^\dagger c_{n'_2} c_{n'_1} | \bar{\alpha}_1 \bar{\alpha}_2 \rangle_a \quad (C.3)$$

$$\begin{aligned} &= \delta_{n_1 \bar{\alpha}_1} \delta_{n_2 \bar{\alpha}_2} \delta_{n'_1 \bar{\alpha}_1} \delta_{n'_2 \bar{\alpha}_2} + \delta_{n_1 \bar{\alpha}_2} \delta_{n_2 \bar{\alpha}_1} \delta_{n'_1 \bar{\alpha}_1} \delta_{n'_2 \bar{\alpha}_1} \\ &\quad - \delta_{n_1 \bar{\alpha}_2} \delta_{n_2 \bar{\alpha}_1} \delta_{n'_1 \bar{\alpha}_1} \delta_{n'_2 \bar{\alpha}_2} - \delta_{n_1 \bar{\alpha}_1} \delta_{n_2 \bar{\alpha}_2} \delta_{n'_1 \bar{\alpha}_2} \delta_{n'_2 \bar{\alpha}_1}, \end{aligned} \quad (C.4)$$

where in the last step the creation and annihilation operators, c and c^\dagger , are applied to the harmonic oscillator states.

Taking the unitary operator (C.1) in harmonic oscillator representation to unitarily transform the two-body density in harmonic oscillator representation gives

$$\begin{aligned} &\langle \alpha_1 \alpha_2 | U^\dagger R(n_1 n_2, n'_1 n'_2) U | \alpha'_1 \alpha'_2 \rangle \\ &= \frac{1}{4} \sum_{\bar{\alpha}_1 \bar{\alpha}_2 \bar{\alpha}_1 \bar{\alpha}_2} \langle \alpha_1 \alpha_2 | U^\dagger | \bar{\alpha}_1 \bar{\alpha}_2 \rangle_{aa} \langle \bar{\alpha}_1 \bar{\alpha}_2 | c_{n_1}^\dagger c_{n_2}^\dagger c_{n'_2} c_{n'_1} | \bar{\alpha}_1 \bar{\alpha}_2 \rangle_{aa} \langle \bar{\alpha}_1 \bar{\alpha}_2 | U | \alpha'_1 \alpha'_2 \rangle. \end{aligned} \quad (C.5)$$

Evaluation of this equation using (C.4) leads to a quite simple form for the unitarily transformed two-body densities:

$$\begin{aligned} &= \frac{1}{4} \langle \alpha_1 \alpha_2 | U^\dagger | n_1 n_2 \rangle \langle n'_1 n'_2 | U | \alpha'_1 \alpha'_2 \rangle + \frac{1}{4} \langle \alpha_1 \alpha_2 | U^\dagger | n_2 n_1 \rangle \langle n'_2 n'_1 | U | \alpha'_1 \alpha'_2 \rangle \\ &\quad - \frac{1}{4} \langle \alpha_1 \alpha_2 | U^\dagger | n_2 n_1 \rangle \langle n'_1 n'_2 | U | \alpha'_1 \alpha'_2 \rangle - \frac{1}{4} \langle \alpha_1 \alpha_2 | U^\dagger | n_1 n_2 \rangle \langle n'_2 n'_1 | U | \alpha'_1 \alpha'_2 \rangle \end{aligned} \quad (C.6)$$

$$= \langle \alpha_1 \alpha_2 | U^\dagger | n_1 n_2 \rangle \langle n'_1 n'_2 | U | \alpha'_1 \alpha'_2 \rangle. \quad (C.7)$$

The one-body density matrix can then be calculated by summation over the states n :

$$\sum_n \langle \alpha_1 \alpha_2 | U^\dagger R(n_1 n, n'_1 n) U | \alpha'_1 \alpha'_2 \rangle = \sum_n \langle \alpha_1 \alpha_2 | U^\dagger | n_1 n \rangle \langle n'_1 n | U | \alpha'_1 \alpha'_2 \rangle. \quad (C.8)$$

These results can now be transformed in the representation of interest.

Bibliography

- [1] B. Povh *et al.*, *Teilchen und Kerne*, 8th ed. (Springer-Verlag, 2009).
- [2] <http://scienceblogs.com/startswithabang/2012/07/06/now-that-weve-got-the-higgs-whats-next/> (2012).
- [3] <http://press.web.cern.ch/press/pressreleases/releases2012/pr17.12e.html> (2012).
- [4] D. J. Gross, Twenty five years of asymptotic freedom, *Nucl.Phys.Proc.Suppl.* **74**, 426 (1999).
- [5] M. J. Savage, Nuclear physics from QCD : The anticipated impact of exa-scale computing, *AIP Conf.Proc.* **1343**, 30 (2011).
- [6] E. Epelbaum, Nuclear Forces from Chiral Effective Field Theory: A Primer, (2010), *nucl-th/001.3229*.
- [7] R. Machleidt and D. Entem, Chiral effective field theory and nuclear forces, *Phys.Rept.* **503**, 1 (2011).
- [8] E. Epelbaum, Few-nucleon forces and systems in chiral effective field theory, *Prog.Part.Nucl.Phys.* **57**, 654 (2006).
- [9] R. B. Wiringa, V. G. J. Stoks, and R. Schiavilla, An accurate nucleon-nucleon potential with charge independence breaking, *Phys. Rev.* **C51**, 35 (1995).
- [10] R. Machleidt, The high precision, charge dependent Bonn nucleon-nucleon potential (CD-Bonn), *Phys.Rev.* **C6**, 024001 (2001).
- [11] R. Roth, T. Neff, and H. Feldmeier, Nuclear structure in the framework of the unitary correlation operator method, *Prog. Part. Nucl. Phys.* **65**, 50 (2010).
- [12] H. Feldmeier, T. Neff, R. Roth, and J. Schnack, A unitary correlation operator method, *Nucl. Phys.* **A632**, 61 (1998).
- [13] S. K. Bogner, R. J. Furnstahl, R. J. Perry, and A. Schwenk, Are low-energy nuclear observables sensitive to high-energy phase shifts?, *Phys. Lett.* **B649**, 488 (2007).
- [14] S. K. Bogner, R. J. Furnstahl, and R. J. Perry, Similarity renormalization group for nucleon-nucleon interactions, *Phys. Rev.* **C75**, 061001 (2007).

- [15] S. D. Glazek and K. G. Wilson, Renormalization of hamiltonians, Phys. Rev. **D48**, 5863 (1993).
- [16] S. D. Glazek and K. Wilson, Perturbative renormalization group for hamiltonians, Phys.Rev. **D49**, 4214 (1994).
- [17] R. Roth, S. Reinhardt, and H. Hergert, Unitary correlation operator method and similarity renormalization group: Connections and differences, Phys. Rev. **C77**, 064003 (2008).
- [18] S. Reinhardt, Comparison and connection of the similarity renormalization group and the unitary correlation operator method, Diploma thesis, TU Darmstadt (2008).
- [19] P. Navratil, J. P. Vary, and B. R. Barrett, Large basis ab initio no-core shell model and its application to C-12, Phys. Rev. **C62**, 054311 (2000).
- [20] R. Roth *et al.*, Hartree-fock and many-body perturbation theory with correlated realistic NN-interactions, Phys.Rev. **C73**, 044312 (2006).
- [21] N. Paar, P. Papakonstantinou, H. Hergert, and R. Roth, Collective multipole excitations based on correlated realistic nucleon-nucleon interactions, Phys.Rev. **C74**, 014318 (2006).
- [22] J. Suhonen, *From Nucleons to Nucleus. Concepts of Microscopic Nuclear Theory* (Springer-Verlag, 2007).
- [23] P. Ring and P.Schuck, *The Nuclear Many-Body Problem*, 3rd ed. (Springer-Verlag, 2004).
- [24] D. J. ROWE, Equations-of-motion method and the extended shell model, Rev. Mod. Phys. **40**, 153 (1968).
- [25] E. Anderson, S. Bogner, R. Furnstahl, and R. Perry, Operator evolution via the similarity renormalization group I: The deuteron, Phys.Rev. **C82**, 054001 (2010).
- [26] S. Weinberg, Phenomenological lagrangians, Physica **A96**, 327 (1979).
- [27] R. Machleidt, Nuclear forces from chiral effective field theory, (2007), nucl-th/0704.0807.
- [28] S. Weinberg, *The Quantum Theory of Fields, Volume 2: Modern Applications* (Cambridge University Press, 2005).
- [29] D. Rozpedzik *et al.*, A first estimation of chiral four-nucleon force effects in He-4, Acta Phys.Polon. **B37**, 2889 (2006).
- [30] E. Epelbaum, Four-nucleon force using the method of unitary transformation, Eur.Phys.J. **A34**, 197 (2007).

- [31] K. Hebeler, S. Bogner, R. Furnstahl, A. Nogga, and A. Schwenk, Improved nuclear matter calculations from chiral low-momentum interactions, *Phys.Rev.* **C83**, 031301 (2011).
- [32] R. Roth *et al.*, Ab initio calculations of medium-mass nuclei with normal-ordered chiral NN+3N interactions, *Phys.Rev.Lett.* **109**, 052501 (2012).
- [33] D. R. Entem and R. Machleidt, Accurate charge-dependent nucleon-nucleon potential at fourth order of chiral perturbation theory, *Phys. Rev.* **C68**, 041001 (2003).
- [34] R. Roth, T. Neff, H. Hergert, and H. Feldmeier, Nuclear structure based on correlated realistic nucleon-nucleon potentials, *Nucl. Phys.* **A745**, 3 (2004).
- [35] T. Neff and H. Feldmeier, Tensor correlations in the unitary correlation operator method, *Nucl. Phys.* **A713**, 311 (2003).
- [36] R. Roth, *Effektive Wechselwirkungen für Quantenflüssigkeiten und Quantengase*, PhD thesis, TU Darmstadt (2000).
- [37] T. Neff, *Short-Ranged Central and Tensor Correlations in Nuclear Many-Body Systems*, PhD thesis, TU Darmstadt (2002).
- [38] R. Roth, H. Hergert, P. Papakonstantinou, T. Neff, and H. Feldmeier, Matrix elements and few-body calculations within the unitary correlation operator method, *Phys. Rev.* **C72**, 034002 (2005).
- [39] F. Wegner, Flow-equations for hamiltonians, *Ann. Phys.* (1994).
- [40] F. J. Wegner, Flow equations for hamiltonians, *Nucl. Phys. Proc. Suppl.* **90**, 141 (2000).
- [41] S. Szpigel and R. J. Perry, The Similarity renormalization group, (2000), hep-ph/0009071.
- [42] E. Jurgenson, *Applications of the Similarity Renormalization Group to the Nuclear Interaction*, PhD thesis, Ohio State University (2009).
- [43] E. Jurgenson, P. Navratil, and R. Furnstahl, Evolution of nuclear many-body forces with the similarity renormalization group, *Phys.Rev.Lett.* **103**, 082501 (2009).
- [44] R. Roth, J. Langhammer, A. Calci, S. Binder, and P. Navratil, Similarity-transformed chiral NN+3N interactions for the ab initio description of 12-C and 16-O, *Phys.Rev.Lett.* **107**, 072501 (2011).
- [45] K. Hebeler, Momentum space evolution of chiral three-nucleon forces, *Phys.Rev.* **C85**, 021002 (2012).
- [46] H. Hergert, *An Ab-Initio Approach to Pairing Phenomena Using Modern Effective Interactions*, PhD thesis, TU Darmstadt (2008).

- [47] A. Günther, *Nuclear Structure with Unitarily Transformed Two-Body plus Phenomenological Three-Body Interactions*, PhD thesis, TU Darmstadt (2011).
- [48] H. Feldmeier, W. Horiuchi, T. Neff, and Y. Suzuki, Universality of short-range nucleon-nucleon correlations, *Phys.Rev.* **C84**, 054003 (2011).
- [49] K. Wendt, R. Furnstahl, and S. Ramanan, Local Projections of Low-Momentum Potentials, *Phys.Rev.* **C86**, 014003 (2012).
- [50] P. Navrátil and W. E. Ormand, Ab initio shell model calculations with three-body effective interactions for *p*-shell nuclei, *Phys. Rev. Lett.* **88**, 152502 (2002).
- [51] E. Caurier, G. Martinez-Pinedo, F. Nowacki, A. Poves, and A. P. Zuker, The shell model as unified view of nuclear structure, *Rev. Mod. Phys.* **77**, 427 (2005).
- [52] A. Nogga, H. Kamada, and W. Gloeckle, Modern nuclear force predictions for the alpha particle, *Phys.Rev.Lett.* **85**, 944 (2000).
- [53] M. Viviani, L. Girlanda, A. Kievsky, L. Marcucci, and S. Rosati, Bound and scattering states with non-local potentials, *Nucl. Phys. A* **790** (2007).
- [54] K. Heyde, *Basic ideas and concepts in nuclear physics*, Second ed. (Institute of Physics Publishing, 1999).
- [55] P. Papakonstantinou and R. Roth, Large-scale second RPA calculations with finite-range interactions, *Phys.Rev.* **C81** (2010).
- [56] R. Roth and J. Langhammer, Pade-resummed high-order perturbation theory for nuclear structure calculations, *Phys.Lett.* **B683**, 272 (2010).
- [57] G. Audi, A. Wapstra, and C. Thibault, The AME 2003 atomic mass evaluation: (II). tables, graphs and references, *Nucl. Phys.* **A729** (2003).
- [58] G. Hagen *et al.*, Coupled-cluster theory for three-body hamiltonians, *Phys.Rev.* **C76**, 034302 (2007).
- [59] S. Kehrein, *The Flow Equation Approach to Many-Particle Systems* (Springer-Verlag, 2006).
- [60] W. Li, E. Anderson, and R. Furnstahl, The similarity renormalization group with novel generators, *Phys.Rev.* **C84**, 054002 (2011).
- [61] K. Tsukiyama, S. Bogner, and A. Schwenk, In-medium similarity renormalization group for nuclei, *Phys.Rev.Lett.* **106**, 222502 (2011).
- [62] K. Tsukiyama, S. Bogner, and A. Schwenk, In-Medium Similarity Renormalization Group for Open-Shell Nuclei, *Phys.Rev.* **C85**, 061304 (2012).
- [63] K. Wendt, R. Furnstahl, and R. Perry, Decoupling of spurious deep bound states with the similarity renormalization group, *Phys.Rev.* **C83**, 034005 (2011).

- [64] R. Furnstahl, The renormalization group in nuclear physics, Nucl.Phys.Proc.Suppl. **228**, 139 (2012).
- [65] I. Stetcu and J. Rotureau, Effective interactions and operators in no-core shell model, Prog.Part.Nucl.Phys. **69**, 182 (2013).
- [66] R. Roth, Die Methode der unären Korrelatoren und ihre Anwendung auf kurzreichweitig abstoßende Nukleon-Nukleon-Wechselwirkungen, Diploma thesis, TH Darmstadt (1997).
- [67] S. Eidelman *et al.*, Review of particle physics, Physics Letters B **592** (2004).
- [68] Y.-W. Lui, H. L. Clark, and D. H. Youngblood, Giant resonances in ^{16}O , Phys. Rev. C **64**, 064308 (2001).
- [69] D. H. Youngblood, Y.-W. Lui, and H. L. Clark, Isoscalar $e0$, $e1$, and $e2$ strength in ^{40}Ca , Phys. Rev. C **63**, 067301 (2001).
- [70] F. Bertrand, G. Satchler, D. Horen, and A. van der Woude, Systematics of the isoscalar giant monopole resonance from 60 MeV inelastic proton scattering, Physics Letters B **80**, 198 (1979).
- [71] S. Raman, J. Nestor, C.W.G., and P. Tikkanen, Transition probability from the ground to the first-excited $2+$ state of even-even nuclides, Atom.Data Nucl.Data Tabl. **78**, 1 (2001).
- [72] R. Roth, Importance truncation for large-scale configuration interaction approaches, Phys.Rev. **C79**, 064324 (2009).
- [73] A. Calci, Ab initio nuclear structure with SRG-transformed chiral NN plus NNN interactions, Master's thesis, TU Darmstadt (2010).
- [74] J. Langhammer, Consistent chiral three-nucleon interactions in nuclear structure, Master's thesis, TU Darmstadt (2010).
- [75] F. Osterfeld, Nuclear spin and isospin excitations, Rev. Mod. Phys. **64**, 491 (1992).
- [76] W. Nolting, *Grundkurs Theoretische Physik 7*, 7th ed. (Springer-Verlag, 2009).
- [77] R. Roth, Theoretische Kernphysik (WS 2006/2007), Vorlesungsskript.
- [78] D. A.Varshalovich, A. N.Moskalev, and V. K.Khersonskii, *Quantum Theoy of Angular Momentum* (World Scientific, 1989).

Danksagung

Zum Gelingen dieser Arbeit haben viele Personen beigetragen denen ich im Folgenden danken möchte.

Besonderer Dank gebührt Professor Robert Roth, der mir die Möglichkeit gegeben hat diese Arbeit anzufertigen. Seine motivierende Art und sein Interesse haben zum Gelingen dieser Arbeit erheblich beigetragen.

Professor Jochen Wambach danke ich für die Übernahme des Zweitgutachtens.

Den aktuellen und ehemaligen Mitgliedern der Theorieabteilung des IKP danke ich für ihre freundliche Aufnahme und die angenehme Arbeitsatmosphäre. Ganz besonderer Dank gebührt hierbei Heiko Hergert für das Korrekturlesen dieser Arbeit, sowie das schnelle und sehr kompetente Beantworten meiner Fragen und seine Hilfestellung zum Verständnis der RPA. Meinen zahlreichen Bürokollegen danke ich für die netten Gespräche über physikalische und nicht-physikalische Themen. Hierbei sind besonders Hannes Basler und Anneke Günther hervorzuheben, die mich, zusammen mit Klaus Heckmann, immer wieder sehr unterstützt haben. David Scheffler, Nils Strodthoff und Markus Huber danke ich für den Zusammenhalt der "Hinterbliebenen". Richard Tripel danke ich für die Bereitstellung des Einteilchen-RPA-Codes und die Beantwortung meiner Fragen hierzu.

Meinen Freunden danke ich für ihre Motivation und die vielfältigen Ablenkungen.

Meiner Familie möchte ich für ihre unermüdliche Unterstützung danken. Die Übernahme der Kinderbetreuung hat es mir ermöglicht diese Arbeit anzufertigen. Ganz besonderer Dank gilt Markus und Annika, die mir immer wieder gezeigt haben was im Leben wirklich wichtig ist.

Lebenslauf

Persönliche Daten

Name	Sabine Reinhardt
Geburtstag	23. Juni 1983
Geburtsort	Groß-Gerau
Staatsangehörigkeit	deutsch
Eltern	Werner Reinhardt Irene Reinhardt, geb. Weichel
Familienstand	ledig, 1 Kind

Bildungsweg

08/1989 - 07/1993	Besuch der Schillerschule Groß-Gerau (Grundschule)
09/1993 - 06/2002	Besuch der Prälat-Diehl-Schule Gymnasium Groß-Gerau
06/2002	Abitur
10/2002 - 04/2008	Studium der Physik an der TU Darmstadt
07/2005 - 06/2006	ERASMUS Austauschprogramm an Norges Teknisk- og Naturvitenskapelige Universitet, Trondheim, Norwegen
04/2007 - 03/2008	Anfertigung der Diplomarbeit " <i>Comparison and Connection of the Similarity Renormalization Group and the Unitary Correlation Operator Method</i> "
04/2008	Diplom, Gesamtnote: sehr gut
seit 05/2008	Promotionsstudium an der TU Darmstadt und Anfertigung der Dissertation
seit 05/2008	Wissenschaftliche Mitarbeiterin am Institut für Kernphysik